AEROSPACE ENGINEERING

Master's Degree Thesis

Implementation of a Solver for Static Aeroelasticity and Flutter Prediction on Light Sport Aircrafts based on VLM, DLM and advanced 1D structural models

Academic Supervisors

Prof. Marco Petrolo

Prof. Enrico Zappino

Candidate

Filippo Miotto

Company Supervisor

Ing. Cristian Cosatto

April 2022

Ringraziamenti

Vorrei rendere questa pagina un breve riassunto di tutto ciò che una tesi di laurea nasconde e non può essere raccontato dai risultati degli esami o dalla carriera lavorativa. Questo momento così importante è il frutto di tantissime ore di studio e di impegno, di tanti momenti felici e di periodi difficili che ho affrontato assieme a molte persone che mi hanno sostenuto e permesso di essere qui oggi.

In primo luogo, vorrei ringraziare tutto il personale della *Fly Synthesis s.r.l.*, che mi ha permesso di collaborare con loro in un momento storico complicato e di ampliare gli orizzonti delle mie esperienze professionali. Un ringraziamento particolare lo devo all'Ing. Cristian Cosatto, che mi ha guidato in questa esperienza.

Con la stessa gratitudine ringrazio il Prof. Marco Petrolo ed il Prof. Enrico Zappino, che si sono sempre resi disponibili in modo tempestivo ed efficace nelle diverse fasi dello svolgimento di questo lavoro e mi hanno consigliato con la loro esperienza nel campo dell'aeroelasticità.

Un ringraziamento speciale lo devo ai miei genitori, Rosella e Gino, e a mia sorella Chiara, che mi hanno sempre supportato non solo a livello economico, ma soprattutto perché hanno creduto in me, mi hanno permesso di seguire i miei sogni e mi hanno sostenuto nei momenti difficili (ammetto che nemmeno in un libro potrei elencare tutti i motivi per cui vi sono grato). Lo stesso vale per la nonna Armida, con cui ho condiviso molto e, tra un caffè e l'altro, mi ha dato dei consigli di vita preziosi.

Ringrazio gli zii e zie (Andrea, Costantino, Federica, Paola e Sonia) e le mie cugine (Arianna, Cinzia ed Emma) per tutti i bei momenti passati assieme, i pranzi di famiglia e le esperienze condivise. Un ringraziamento speciale va alla zia Paola, che mi ha sempre dato dei buoni consigli e spronato ad allargare i miei orizzonti.

Oltre alla famiglia, ci sono tanti amici con cui ho condiviso molto nel corso di questi anni tra il Friuli e Torino. Nonostante alcuni di loro siano lontani in questo momento e le nostre strade siano diverse, vorrei comunque ricordare l'importanza delle esperienze condivise e di tutti i bei ricordi che mi hanno lasciato. Una menzione speciale va agli amici di sempre e in particolare a Davide e Mattia, su cui posso sempre contare.

Sommario

Il presente lavoro è incentrato sull'implementazione di un gruppo di codici MatLab® basati su metodi semplificati per lo studio dei principali fenomeni aeroelastici applicati ai velivoli ultraleggeri. Le tre ipotesi fondamentali che caratterizzano l'analisi riguardano la non viscosità del flusso, le oscillazioni aerodinamiche di tipo puramente armonico nel caso di fenomeni non-stazionari e l'analisi strutturale mediante elementi di tipo unidimensionale.

I principali passi seguiti sono:

- L'analisi aerodinamica, che è stata sviluppata in campo inviscido nel caso stazionario (Vortex Lattice Method) e non stazionario (Doublet Lattice Method);

- L'analisi della deformazione strutturale statica e dinamica di strutture unidimensionali di tipo trave tramite metodo agli elementi finiti implementato con elementi isoparametrici e *Carrera Unified Formulation*;

- L'analisi dell'interazione statica tra le sollecitazioni aerodinamiche e la deformazione strutturale (divergenza torsionale) mediante l'analisi degli autovalori delle matrici di rigidezza aeroelastica;

- L'analisi dell'interazione dinamica (*flutter*) tra le sollecitazioni aerodinamiche e la deformazione strutturale con l'utilizzo del *k-method*.

Per ognuno dei punti presentati è stata svolta un'analisi dei modelli utilizzati per il loro studio, seguita da una fase di implementazione dei codici MatLab® e dall'applicazione degli strumenti ottenuti al caso del velivolo ultraleggero biposto (MTOW<600kg) *Syncro*, prodotto dall'azienda Fly Synthesis s.r.l.

Summary

Implementation of a group of MatLab® codes based on simplified methods that permit the study of main aeroelastic phenomena, applied on ultralight Light Sport Aircrafts. The fundamental hypotheses of these analyses concern the inviscid nature of the considered fluid, harmonic oscillations (when unsteady aerodynamic phenomena are considered) and 1D beam structural elements.

The principal steps of this work are:

- The aerodynamic analysis, developed in the steady case through Vortex Lattice Method and in the unsteady one through Doublet Lattice Method.

- The static structural deformation analysis and the free-vibrational analysis, developed through finite elements method using isoparametric elements and *Carrera Unified Formulation* for unidimensional beam structures.

- Analysis of the interaction between static aerodynamic loads and structural deformation (torsional divergence) through the evaluation of eigenvalues of aeroelastic stiffness matrix.

- Analysis of the interaction between harmonic aerodynamic loads and dynamic structural deformation (*flutter analysis*) through *k-method*.

Every point presented in this work has been investigated through the main theories that are related to these phenomena. Afterwards, the MatLab® codes have been developed and applied on the Light Sport Aircraft (*MTOW<600kg*) *Syncro*, produced by the Fly Synthesis s.r.l. company.

Contents

Ringraziamenti ... 3
Sommario ... 5
Summary ... 6
Contents ... 7
List of Figures ... 11
List of Tables ... 13

Chapter 1
Introduction ... 15
1.1 Aeroelastic Phenomena ... 15
1.2 Importance of aeroelasticity prediction ... 16
1.2.1 Handley Page O/400 and first flutter cases ... 16
1.2.2 F-117A Nighthawk elevon flutter ... 17
1.2.3 Solution methods and testing historical overview ... 18
1.4 Aim of this work ... 18
1.5 Case study: Fly Synthesis Syncro ... 19

Chapter 2
Aerodynamic models ... 21
2.1 Laplace Equation and inviscid aerodynamic model ... 21
2.2 Singularities for Laplace Equation Solution ... 22
2.2.1 Uniform Current Singularity ... 22
2.2.2 Vortex Singularity ... 22
2.2.3 Doublet Singularity ... 23
2.3 Vortex Lattice Method (VLM) ... 23
2.4 Doublet Lattice Method (DLM) ... 27
2.5 Aerodynamic Code Development and Verification ... 33
2.5.1 Steady Aerodynamics Contribute (VLM) ... 33
2.5.1.1 Main steady code development steps ... 33
2.5.1.2 Syncro wing geometrical properties ... 36
2.5.1.3 Verification on target analysis aircraft and convergence considerations ... 37
2.5.1.4 Wing symmetry code simplifications ... 39
2.5.2 Unsteady Aerodynamic Contribute (DLM) ... 39
2.5.2.1 Main Unsteady Code Development Steps ... 40
2.5.2.2 DLM code verification ... 41
2.5.2.3 Unsteady Aerodynamic Properties of Syncro Wing ... 42

Chapter 3
Structural models 45
3.1 Stresses and Displacements, Geometrical Relations, and Constitutive Equations 45
3.1.1 Geometrical relations..46
3.1.2 Constitutive equations 46
3.2 Beam modeling through Carrera unified formulation 49
3.2.1 McLaurin polynomials...49
3.2.2 Isoparametric Finite Elements 50
3.3 1D Finite Elements model 52
3.4 Principle of Virtual displacements and solution of the problem 53
3.5 Static Deformation Problem 55
3.6 Free Vibration Problem 56
3.7 Structural stiffness and mass matrices 57
3.8 Global coordinate system 59
3.9 Structural Code Development and Verification 61
3.9.1 Main code development steps...61
3.9.2 Code verification and convergence considerations 63
3.9.3 Syncro wing geometry simplification 64
3.9.3.1 Composite materials properties...64
3.9.3.2 Main structural components and equivalent section properties 65
3.9.3.3 Static analysis results 67
3.9.3.4 Pure bending section calibration 68
3.9.3.5 Pure twist section calibration 70
3.9.3.6 Modal analysis results..72
3.9.4 Modal analysis results on composite materials beams 73

Chapter 4
Splining Process 75
4.1 Infinite Plate Spline method 75
4.2 Load and control points notation 77
4.2.1 Displacements at Load and Control points 78
4.2.2 Slopes at Control points...78
4.3 Unsteady boundary condition for DLM...79
4.4 IPS Code Development and Results 79
4.4.1 Main code development steps..80
4.4.2 Code verification and convergence considerations 81
4.4.3 Syncro wing geometry simplification 82

Chapter 5
Aeroelastic model..83
5.1 Static aeroelastic model 83

5.1.1 Steady aerodynamic loads vector....83
5.1.2 Aerodynamic stiffness matrix....85
5.1.3 Aeroelastic stiffness matrix and problem solution....86
5.2 Dynamic aeroelastic model: flutter....88
5.2.1 General problem description....88
5.2.2 p-k method....90
5.2.3 k method....92

Chapter 6
Static Aeroelasticity and Flutter Results....93
6.1 Static Aeroelasticity code development....93
6.2 Flutter code development....94
6.3 Static Aeroelasticity results....95
6.3.1 Constant cross-section test beam....95
6.3.2 Syncro torsional divergence evaluation....97
6.3.3 Effect of lamination on divergence speed....99
6.3.4 Sweep effect on static divergence velocity....103
6.4 Flutter results....105
6.4.1 Constant cross-section test beam....105
6.4.2 Simple case experimental references and g-method analysis....107
6.4.3 HALE aircraft equivalent wing model....108
6.4.4 Syncro model flutter evaluation....109

Chapter 7
Conclusions....111

Chapter 8
Appendix....115
Appendix I – ISA Atmosphere....115
Appendix II – Material stiffness coefficients matrix....116
Appendix III – Static test loading conditions....117
Appendix IV - Code Interfaces....118
IV.1 VLM interface....118
IV.2 DLM interface....119
IV.3 Structural static deformation interface....120
IV.4 Other codes....120

Bibliography....121

List of Figures

Figure 1: Schematization of the aeroelastic problem. 15
Figure 2: Handley Page O/400 Bomber. 16
Figure 3: F117A Nighthawk. 17
Figure 4: Syncro ultralight aircraft in flight. 19
Figure 5: Uniform current velocity due to equation 2.5 singularity. 22
Figure 6: Irrotational vortex singularity. 22
Figure 7: Doublet vortex singularity. 23
Figure 8: Example of cosine law use for grid refinement at wing tips. 23
Figure 9: Vortex Ring element represented on the generic j-th trapezoidal panel of the wing. 24
Figure 10: Horseshoe vortex element represented on the generic j-th trapezoidal panel of the wing. 24
Figure 11: Generic constant vortex line segment in 3D space. 25
Figure 12: Simple example of wing discretization with horseshoe and ring vortex elements (panels numbering order is also shown). 27
Figure 13: Representation of global and local coordinate systems for DLM. 28
Figure 14: Aspect ratio definition for rectangular panels. 33
Figure 15: Syncro profile representation in its coordinate system. 34
Figure 16: Code structure for the aerodynamic influence coefficients evaluation. 35
Figure 17: Wing and tail geometric properties for Syncro aircraft. 36
Figure 18: Lift and drag coefficients versus angle of attack. 38
Figure 19: Polar curves from present code and Athena Vortex Lattice. 38
Figure 20: VLM lift coefficient distribution along span coordinate (angle of attack 2°). 39
Figure 21: Code structure for unsteady aerodynamic influence coefficients evaluation. 40
Figure 22: Test semi-wing and aileron geometry. 41
Figure 23: Test semi-wing pressure coefficient results. 42
Figure 24: Semi-wing geometry and mesh representation for Syncro aircraft. 43
Figure 25: Reference system for a beam element with circular cross section. 45
Figure 26: Representation of stress and strain components in 3D space. 45
Figure 27: Material and physical coordinates for an orthotropic material. 48
Figure 28: McLaurin polynomials for N=4. From left to right and from to bottom the polynomials are: 1, x, z, x^2, xz, z^2, x^3, x^2z, xz^2, z^3, x^4, x^3z, x^2z^2, xz^3, z^4. 50
Figure 29: Natural coordinate system for a 4-node finite element. 51
Figure 30: Third order Lagrange polynomials in the natural coordinate system. 52
Figure 31: Stiffness and mass matrices building procedure for 4-th order cross section approximation and 4-node elements. 58

Figure 32: Stiffness and mass matrices building procedure for a 4-node beam structure (4 elements are considered)..........59
Figure 33: Representation of the local and global coordinate systems relation..........60
Figure 34: Representation of the beam used for verification process..........63
Figure 35: Discrete semi-wing cross section geometry for Syncro aircraft (right semi-wing)..........67
Figure 36: Static analysis z deformation for Syncro semi-wing, 4-th order McLaurin polynomials and n=1 loading at shear centre..........69
Figure 37: Static analysis results for Syncro semi-wing with 5-th order McLaurin polynomials and n=1 loading at shear centre. Comparison with experimental results..........69
Figure 38: Static analysis results for Syncro semi-wing with 2-nd order McLaurin polynomials and twist test loading. Comparison with experimental results..........71
Figure 39: Modal analysis results for Syncro semi-wing with 4-nd order McLaurin polynomials..........72
Figure 40: Lamination angles for an orthotropic beam (from top to bottom: 0°, 45°, 90°)..........74
Figure 41: Coordinate system and load application points representation..........76
Figure 42: Pseudo Structural Points for a generic simple semi-wing..........81
Figure 43: Syncro wing geometry configuration. Relation between structural elements position and aerodynamic surface collocation..........82
Figure 44: Damped, harmonic, and amplified oscillations for a single degree of freedom system..........89
Figure 45: p-k method algorithm for a flutter problem with Nmodes modal shapes..........91
Figure 46: Main static aeroelasticity code sections..........93
Figure 47: Tip angular deflection behaviour for a generic test semi-wing, 3-rd order McLaurin polynomials. 96
Figure 48: Orthotropic material lamination angle reference system for a generic beam structure..........99
Figure 49: Tip section rotation angles for different lamination angles and airspeeds..........101
Figure 50: Aeroelastic tayloring effect on divergence velocities..........102
Figure 51: Sweep angle reference system on a generic tapered right semi-wing..........103
Figure 52: Sweep angle influence on spanwise lift coefficient distribution (present code results)..........103
Figure 53: Sweep angle influence on static divergence velocity (present code results)..........104
Figure 54: First 10 modes frequencies for the considered test beam..........106
Figure 55: Unstable mode damping-velocity plot for HALE aircraft..........109
Figure 56: ISA Atmosphere temperature and density variation..........115
Figure 57: Vortex Lattice Method code user interface..........118
Figure 58: Doublet Lattice Method code user interface..........119
Figure 59: Structural code user interface..........120

List of Tables

Table 1: Examples of flutter events and incidents recorded in the first period of aviation development. 17
Table 2: Fly Synthesis Syncro main technical data. 20
Table 3: Coefficients for Desmarais approximation of I0 integral. 32
Table 4: Limits for aspect ratio of DLM panels. 33
Table 5: Main xFoil commands used in the described code. 34
Table 6: Aerodynamic geometry of Syncro wing. 36
Table 7: Grid parameters convergence evaluations. 37
Table 8: Angular lift coefficient error evaluation 37
Table 9: Computational times comparison between semi-wing and complete wing VLM model. 39
Table 10: DLM test semi-wing properties. 41
Table 11: Definition of material stiffness matrix coefficients for orthotropic and isotropic materials. 47
Table 12: Number of DOFs for a 10 elements beam. 52
Table 13: Modal Analysis - Results for different orders of cross-section approximation and number beam of elements. 63
Table 14: Static deformation - Results for different orders of cross-section approximation and number beam of elements. 64
Table 15: Composite materials specifications. 65
Table 16: Laminated composite materials - Fibre sheets global properties. 65
Table 17: Discrete semi-wing cross section properties for Syncro aircraft. 66
Table 18: Discrete semi-wing cross section properties for Syncro aircraft. 68
Table 19: Discrete semi-wing nodal z displacements for element node 2...70
Table 20: Discrete semi-wing cross section properties for Syncro aircraft, torsional properties calibration...71
Table 21: Modal analysis results for square cross-section. 73
Table 22: Orthotropic beam geometrical and material properties. 74
Table 23: Orthotropic beam modal frequencies (4-th order McLaurin polynomials cross-section discretization). 74
Table 24: Aerodynamic matrix terms definition through DLM and IPS splining results. 91
Table 25: Test beam structure properties. 95
Table 26: Test semi-wing aerodynamic properties. 95
Table 27: Static aeroelasticity results comparison. 96
Table 28: Test semi-wing divergence velocity. 97
Table 29: Syncro semi-wing divergence velocity evaluation, aerodynamic grid definition and convergence considerations for Δ=1.54 (real wing shear centre approximate position). 97
Table 30: Syncro semi-wing divergence velocity evaluation, 1.225 kg/m^3 air density. 98

Table 31: Syncro semi-wing divergence velocity evaluation, altitude variation effect. 99
Table 32: Orthotropic material beam structure properties. 100
Table 33: Aeroelastic tayloring effect on divergence velocities, percentual variation. 102
Table 34: Test case beam properties and considered discretization. 104
Table 35: Lift coefficient results verification for three different sweep angles on the considered semi-wing (incidence: 1°). 104
Table 36: Test beam geometrical and material properties for flutter analysis. 105
Table 37: Test beam structural and aerodynamic grid properties for flutter analysis. 105
Table 38: Test beam flutter results comparison. 106
Table 39: Reference rectangular beam aerodynamic and structural grids. 107
Table 40: Reference rectangular beam geometrical and material properties. 107
Table 41: Flutter results comparison for the rectangular beam test case considered. 108
Table 42: First six free vibrational modes for the considered rectangular beam. 108
Table 43: Geometrical and structural properties of HALE aircraft. 108
Table 44: HALE aircraft discretization properties. 109
Table 45: Syncro aircraft flutter results. 110
Table 46: Semi-wing loadings for experimental tests. 117

Chapter 1

Introduction

1.1 Aeroelastic Phenomena

The project of an aircraft has always been focused on the analysis of the structural and fluid-dynamic parameters of its main components, including wing, stabilizer, rudder, and fuselage. The interaction between these two sides of the aeronautical project has been investigated for decades, since the structural deformation of an aerodynamic element influences the fluid-dynamic forces generated in that configuration.

A general definition for aeroelasticity was developed by *Arthur Roderick Collar [2]* in 1947:

"the study of the mutual interaction that takes place within the triangle of the inertial, elastic, and aerodynamic forces acting on structural members exposed to an airstream, and the influence of this study on design".

This sentence can be explained by a simple scheme, as reported by *Hodges and Pierce [1]*, which identifies the main aspects of this field of engineering. It is important to notice that it refers not only to aeronautics, but to all the problems where an elastic element with his own mass interacts with aerodynamic forces.

In *Figure 1,* three types of actions can be identified at the vertices of the triangle:

1. Aerodynamic forces (surface forces), pressure loads acting on a surface generated by the interaction of a fluid flow with a body at a certain relative speed.
2. Elastic forces, that represent the forces related to the deformation of the body under determined loading conditions.
3. Dynamics, which is the study of the movement of a body due to certain actions.

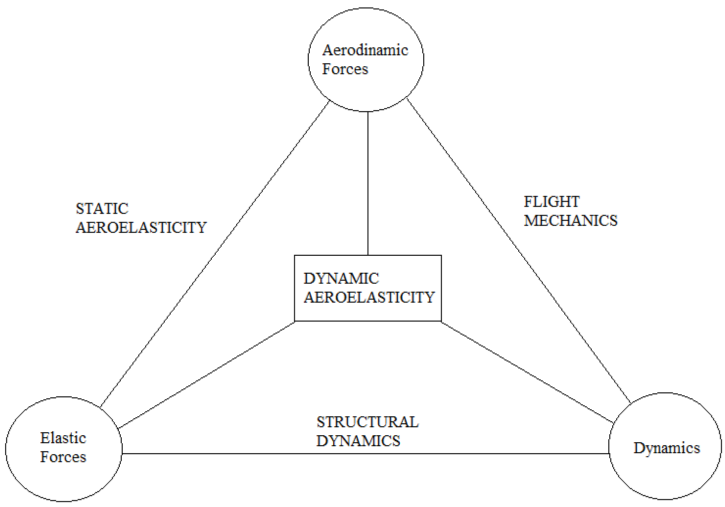

Figure 1: Schematization of the aeroelastic problem.

The mutual interaction of these elements is at the origin of the disciplines listed on the triangle sides and at its centre. The relation between aerodynamic and elastic forces and the one between all actions defines the two main fields of study of aeroelasticity:

- *Static Aeroelasticity*, which is the study of the interaction of aerodynamic loadings induced by a steady flow and the consequent deformation of the structure. According to *A. R. Collar [2],* it influences controllability, performance, stability, and structural stiffness of an aerodynamic element (a wing element will be considered from this section on for the sake of simplicity). All phenomena are intended as static ones since this analysis is focused on equilibrium configuration and deformation of the considered wing element.

- *Dynamic Aeroelasticity*, in the following pages flutter phenomenon will be considered. It is defined as the interaction between aerodynamic forces and dynamic vibrational modes of a wing, that can generate undamped oscillations under specific conditions. As stated by *Hodges and Pierce [1], p. 3*, flutter can be perceived as mild vibrations by the pilot and passengers, when it is near to the benign end of the spectrum. On the other hand, it leads to the rapid destruction and loss of the aircraft when oscillations are huge.

This work concentrates on static and dynamic aeroelasticity of Light Sport Aircrafts (with *MTOW < 600kg*) and will try to provide a simple instrument able to evaluate potentially critical conditions on airplanes produced by *Fly Synthesis s.r.l.*

1.2 Importance of aeroelasticity prediction

The occurrence of aeroelastic instability, and in particular of flutter, has been the cause of different concerns in aviation history; this underlines the importance of its avoidance in all flight conditions. In the following chapter, some of these events will be presented to focus on the conditions that generated the insurgence of instabilities. Some examples and an historical overview are provided by *Michael W. Kehoe [3]*; both old and modern (referring to aircraft history) planes experience aeroelastic instability, as shown in the next images.

1.2.1 Handley Page O/400 and first flutter cases

The first recorded incident caused by flutter was on a twin-engine biplane bomber (*Handley Page O/400*) in 1916, during World War I. The oscillating phenomenon was traced to a coupling between the fuselage torsion mode and an antisymmetric elevator rotation mode, that were independently actuated. The solution to this problem was to interconnect the elevators with a torque tube (*Michael W. Kehoe [3], p.5*).

Other flutter situations triggered by control surfaces were experienced during the years of WWI and were resolved with an empirical approach: as stated in the work of *Michael W. Kehoe [3]* the balance mass of control surface was increased and in nearly all situations this brought to the resolution of the issue.

Figure 2: Handley Page O/400 Bomber.

During the 1920's and 1930's, flutter was spotted on primary surfaces and many incidents were reported in the attempt to break speed records. This was also due to the transition from external wire-braced biplanes to cantilevered wings. Later, from 1947 to 1956, many incidents were experienced involving control surface at transonic regimes of flight and the carriage of external stores on wings (such as bombs or external fuel tanks). *Table 1* resumes this type of incidents, according to *Michael W. Kehoe [3]* and *Garrick and Reed [5]*:

Period	***Field***	***Number of events***	***Aerodynamic elements involved***
WW1	Military	Widely Encountered	Ailerons
1925-1935	Civil (Records Challenging)	Widely Encountered	Primary Surfaces
1947-1956	Military	11	Servo Tab
1947-1956	Military	26	Control Surfaces
1947-1956	Military	7	Carriage of external stores/Pylon mounted engines
1947-1956	Military	7	Tails

Table 1: Examples of flutter events and incidents recorded in the first period of aviation development.

1.2.2 F-117A Nighthawk elevon flutter

In 1997, *F-117A Nighthawk* experienced large elevon oscillations and incipient flutter while performing a fly-by demonstration at Martin State Airport air show. The oscillations brought to the loss of the aircraft and its crash on the ground, while the aircraft was completing its third pass over the demonstration zone.

The pilot was starting his climb out for departure when the left wing broke. The aircraft crashed into the residential area of Bowley's Quarters and caused extensive fire damage to several homes and vehicles. There were no fatalities or serious injuries; the pilot, Maj. Bryan K. Knight, ejected himself and received only minor injuries (*NY Times [4]*).

Figure 3: F117A Nighthawk.

The accident investigation report concluded that the cause of the accident was structural failure of a support assembly in the left wing. This was due to 4 missing fasteners of the 39 in the assembly, that were improperly reinstalled during a scheduled periodic inspection in 1996.

The entire fleet of *F-117 Nighthawk* was inspected during a precautionary stand down and none were found to have the same defect. Apparently, the four missing fasteners caused the coupling of aerodynamic forces with free vibration frequencies of the wing, generating a catastrophic condition.

1.2.3 Solution methods and testing historical overview

The first methodical approach trying to describe flutter was developed after World War I. After some practical solution techniques, in 1924-1925 the problem appeared on the British Aeronautical Research Committee yearbook: *"Of increasing importance is the problem of flutter which has been discussed with representatives of a number of firms; a preliminary theoretical attack has been made on the problem. It would appear that the subject may need a large amount of experimental inquiry before a complete solution is obtained".*

This stated the start in flutter research, followed by the establishment of a sub-committee addressed to this specific topic. A solution based on simplified modes of structural deformation, while aerodynamics relied on empirical constants that did not consider the interaction effect of wake vortices (*Garrick and Reed [5], p. 901*). As reported in *AGARD Manual on Aeroelasticity*, *"All the early purely theoretical work on flutter marred inadequacy representation the aerodynamic action."*, thus the first reliable results were obtained through wind tunnel scaled testing, which showed good correlation with the full-scale model. In the same years, some research work was carried out at a *Massachusetts Institute of Technology*, with some theses based on the study of flutter from the practical point of view and wind tunnel testing.

An adequate solution for unsteady aerodynamics was proposed by Theodore Theodorsen in 1934 in *NACA Rept. No. 496*, which contributed to flutter problem solution progression. It refers to the two-dimensional oscillating flat plate with translation, torsion, and aileron motions by means of a separation of the velocity potential in a circulatory part and a non-circulatory one. As will be explained later, this method is at the basis of the strip theory, where flutter is investigated by wing simplification to a representative section.

Other methods were developed in the same years, the 1930's, around the world (in Italy, Japan, Russia…) as well as some empirical criteria based on the torsional frequency, valid for the type of aircrafts developed at that time.

As reported before, testing has been a valid method for flutter prediction, even thought that it is a dangerous technique for the risks concerning test pilots: the procedure consisted into diving the airplane to its maximum speed. An alternative was proposed by von Schlippe in 1935 in Germany, as reported by *Garrick and Reed [5], p. 905*. The phenomenon is studied through the induction of forced mechanical oscillations. Tests permit to predict the velocity for which the oscillations reach a divergent behaviour through an interpolation of data obtained in non-flutter flight conditions. By the late 1940's flight flutter testing achieved improvements through modern flight instrumentation and a better theoretical understanding of the flutter problem. More recently, these methods have evolved into advanced procedures using flight and ground based digital computers, real time tests and analyses.

1.4 Aim of this work

As it has been specified in the previous section, static divergence and flutter could be disruptive phenomena and cause the loss of the aircraft in particular conditions. For this reason, even a simple model for its prediction is essential for the complete project of a modern aircraft.

The advance in aeronautical field and the development of specific models for this type of analysis, as well as the development of adequate calculus capabilities, brought to different solutions for flutter problems, as described in the historical overview before.

These models provide a good approximation of flutter speed, but they refer to a 2D approximation of a three-dimensional problem. Moving from a 2D to a 3D solution permits to include parameters such as sweep angle, ailerons, and taper ratio in the analysis. Moreover, the use of finite elements (FE) for static and free vibrational analysis can improve the evaluation of bending and torsional oscillation frequencies of the structure and evaluate even coupling between different modes.

The aim of this work can, thus, be identified in the development of an efficient aeroelasticity prediction tool. A compromise between a good approximation of this phenomenon and short calculation times is the combination of the following methods for structural and aerodynamic analysis:

1. Vortex Lattice Method (VLM) and Doublet Lattice Method (DLM), based on the solution of Laplace equation in steady (VLM) and unsteady (DLM) case. They use a distribution of vortices and doublets on the wing representative surface, which is approximated by a certain number of trapezoidal elements. A good approximation of lift is provided, while the evaluation of drag is limited to the induced drag contribute.
2. One-dimensional (1D) structural beam models. The use of 1D Finite Elements (FE) can be a good compromise for the representation of wing structures. Nevertheless, there are many orders of approximation for beam elements, with different levels of complexity. Next chapters will focus on their description and on the presentation of *Carrera Unified Formulation* (CUF), used in this approach.

More accurate solutions could be provided using complex models such as:

- Computational Fluid Dynamics (CFD) codes for aerodynamic analysis. These codes imply longer solution times, even though that they permit the study of viscous flows using Reynolds Averaged Navier-Stokes (N-S) equations or more precise representations of N-S equations.
- Two- or three-dimensional models for structural elements, that are more precise in the discretization of wing structures, but also more expensive from the computational point of view.

This last approach will not be presented in the next chapters and is mentioned only for completeness reasons.

1.5 Case study: Fly Synthesis Syncro

As said before, the final aim is to generate a tool that is able (with specific adaptations made for every case) to evaluate static divergence and flutter conditions on aircrafts produced by *Fly Synthesis s.r.l.* In particular, Syncro Light Sport Aircraft case is described in the following lines.

All data and information provided in this chapter were obtained directly from the technical manual of the aircraft or the project database of analysis carried out by the company.

Figure 4: Syncro ultralight aircraft in flight.

This airplane project, born in 2006, is the most advanced of the company and combines the advantages of a light weight 2 seat aircraft with comfort and good performance. The chosen configuration is high wing, since it provides good aerodynamic properties and an easier accessibility.

Many characteristics could be described in this chapter, including all its flight properties and innovative instruments, but they do not concern the aim of this work. The main properties related to aerodynamic surfaces and their structure are listed:

1. The structure of the semi-wing is fully realized in composite materials. Carbon fibre, glass fibre, honeycomb, and resins are used in the realization processes.

2. The wing has a trapezoidal shape: root chord is 1.268m and tip chord is 0.805m.

3. Sweep angle is zero, which means that the quarter chord line is parallel to the y axis (perpendicular to the symmetry plane of the aircraft).

4. Flaps and ailerons are the semi-wing control surfaces (the aircraft does not need slats).

5. As can be observed in *Figure 4*, it is equipped with winglets, that provide a reduction of induced drag.

6. The wing is characterized by four different profiles along the span, that vary aerodynamic properties.

7. Dihedral angle is 2.7°.

8. The tail has a traditional configuration, with horizontal stabilizer and vertical fin.

9. Command line is of mechanical type, while flaps are actuated by an electrical engine.

Wingspan	10,4 m	***Wing area***	10,54 m^2
Height	2,26 m	***Take Off Run***	150 m
Length	6,75 m	***Landing Run***	150 m
MTOW	600 kg	***Stall Speed (V_{s0})***	73 km/h
Max/Min Load Factors	+4g/-2g	***Cruise speed (V_c)***	220 km/h
Engine	Rotax 912	***Cruise speed at 75%***	250 km/h
Power	100 hp	***Never Exceed speed (V_{ne})***	272 km/h
Fuel Capacity	65x2 l	***Endurance with 30' Reserve***	1200 km
Fuel Consumption 75%	18 l/h	***Number of wing profiles used***	4

Table 2: Fly Synthesis Syncro main technical data.

Between all the aircrafts made by this company, *Syncro* aircraft has been selected for the following reasons:

- Its performances are challenging in the Light Sport Aircrafts category and relatively high speeds are reached; thus, flutter evaluations should be properly considered.

- With a view to a restyling of the project in the future, this could be an optimum tool for the evaluation of thinner structures and wing design, bringing to a more flexible solution.

Chapter 2

Aerodynamic models

2.1 Laplace Equation and inviscid aerodynamic model

As was anticipated in the introduction, this work focuses on the use of simplified aerodynamics to study loads on wings in the situation of a steady or an unsteady flow. The main hypothesis introduced (according to *Corrado C. [6]*) are the following:

- Ideal flux, thus viscosity (μ) and thermal conductivity (k) are null.
- Irrotational flow field, which means that $\nabla \times \vec{V} = 0$.

These considerations will be later applied to the balance equations of mass, momentum, and energy, that can be written in the differential non-conservative case as:

$$\begin{cases} \dfrac{D\rho}{Dt} = -\rho\nabla \cdot \vec{V} \\ \rho\left(\dfrac{\partial \vec{V}}{\partial t} + \vec{V} \cdot \nabla\vec{V}\right) = \nabla \cdot \bar{\bar{\tau}} \\ \rho\dfrac{De}{Dt} = -p\nabla \cdot \vec{V} + \rho D + k\nabla^2 T \end{cases} \tag{2.1}$$

Where the main variables and constants that appear in the equation are:

- ρ density of the fluid that is considered.
- $\vec{V}$ velocity vector in 1D, 2D or 3D space.
- $\bar{\bar{\tau}}$ stress tensor representing normal and shear stresses.
- e internal energy.
- p local pressure of the fluid.
- k thermal conductivity.
- D dissipation function.

The hypotheses made before allow to define the kinetic potential function (Θ), which is related to speed *2.2*:

$$\vec{V} = \nabla\Theta \tag{2.2}$$

Thus, the potential equation for a non-steady, compressible, irrotational ideal flux can be written as:

$$\nabla^2\Theta - \frac{1}{c^2}\left[\frac{\partial^2\Theta}{\partial t^2} + \frac{1}{2}\nabla\Theta \cdot \nabla\left(\left||\nabla\Theta|\right|^2 + \frac{\partial}{\partial t}\left(\left||\nabla\Theta|\right|^2\right)\right)\right] = 0 \tag{2.3}$$

Where c is the local speed of sound.

Considering that perturbations affecting the local velocity are small when compared to the module of the undisturbed speed ($\overrightarrow{V_\infty}$) can bring to the linearization of the previous equation, which becomes:

$$\nabla^2\Theta = \frac{1}{{c_\infty}^2}\frac{D^2\Theta}{Dt^2} \tag{2.4}$$

Eventually, the linearized potential equation for a non-steady, compressible, irrotational ideal flux can be used for high Reynolds numbers, thin wake, limited speeds, and small perturbations (profile's camber is limited). Moreover, this means also that the linearized potential equation is valid only for small angles of attack and it is not able to evaluate lift around stall angles.

Now, all the elements necessary for the description of how Vortex Lattice Method works are known, in particular the hypotheses that need to be satisfied.

2.2 Singularities for Laplace Equation Solution

Singularities are used in the solution of Laplace equation in the steady and unsteady case. They are a mean to represent the characteristics of the flow field generated by a wing through the velocity potential. Usually, this is achieved by the superimposition of different distributions of singularities. The next chapter will focus on the distributions across three-dimensional space, while in the following lines the two-dimensional equivalent singularities will be presented to properly describe the phenomena involved (*Arina R. [7] (pp.96-101)*).

2.2.1 Uniform Current Singularity

Uniform current singularity function in 2D space corresponds to the potential function of a uniform fluid flow with two components of velocity in cartesian coordinates (u_∞, v_∞), respectively in red and blue (*Figure 5*):

$$\Theta(x, y) = u_\infty x + v_\infty y \qquad (2.5)$$

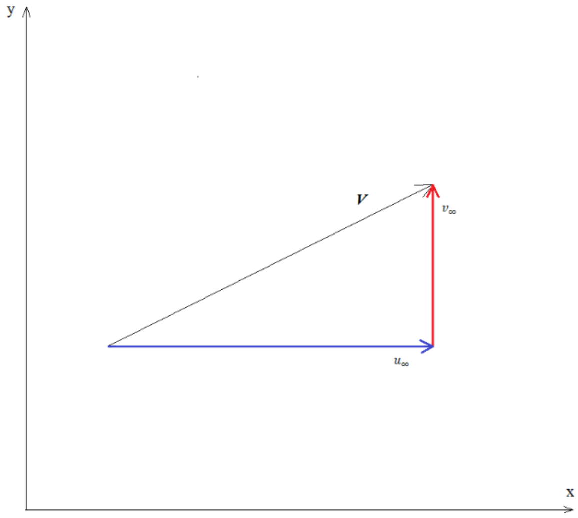

Figure 5: Uniform current velocity due to equation 2.5 singularity.

2.2.2 Vortex Singularity

Vortex Singularity represents the fluid field where an irrotational vortex in 2D space is considered. In the case presented in equation *2.6*, the singularity is located at the origin of cartesian coordinates.

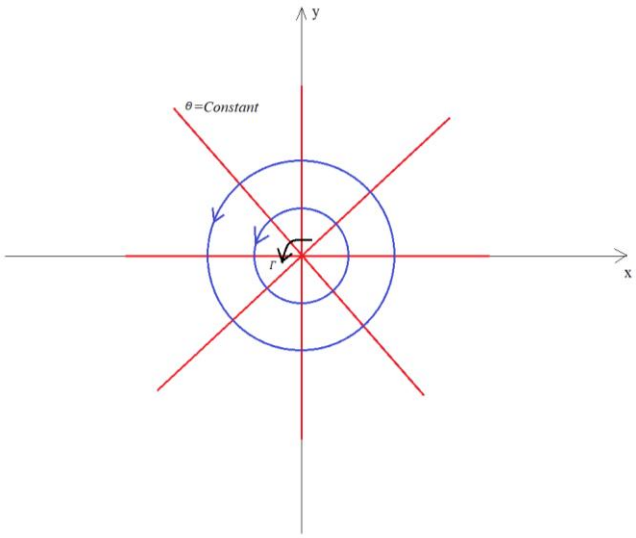

$$\Theta(r, \theta) = \frac{\Gamma}{2\pi}\theta \qquad (2.6)$$

In *Figure 6* equipotential lines are represented in red, while streamlines generated by Γ vortex are circular concentric lines (in blue). Clockwise or anticlockwise rotation depends on the sign of the vortex.

Figure 6: Irrotational vortex singularity.

2.2.3 Doublet Singularity

Doublet Singularity is composed by the superimposition of source sink singularities (*2.7*) of equal intensity. Their distance (*d*) is asymptotically tending to zero, while the intensity of the two sources is q and -q. The doublet is thus represented by the parameter $\mu = dq$ and is located at the origin of the reference system. As for vortex singularity case, streamlines are represented in blue, while equipotential lines are colored in red (*Figure 7*).

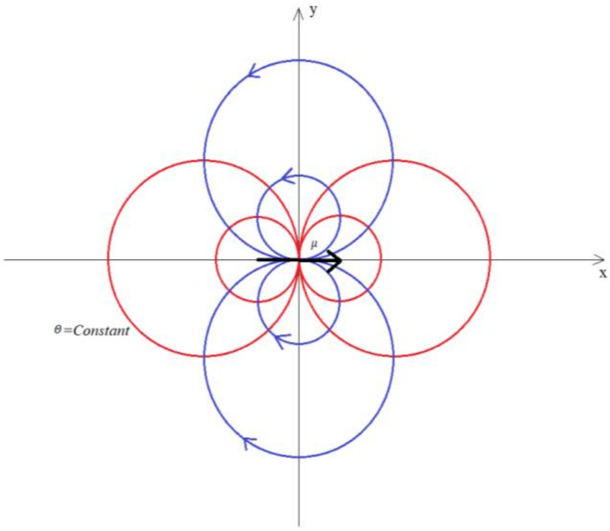

Figure 7: Doublet vortex singularity.

$$\Theta(r,\theta) = \frac{\pm q}{2\pi}\log(r) \tag{2.7}$$

$$\Theta(r,\theta) = -\frac{\mu}{2\pi}\frac{\cos(\theta)}{r} \tag{2.8}$$

2.3 Vortex Lattice Method (VLM)

VLM is based on the solution of the linearized potential equation in the steady case, which means that the previous equation is furtherly simplified (Laplace's equation):

$$\nabla^2\Theta = 0 \tag{2.9}$$

The solution (as described by *Katz and Plotkin [8] (pp. 380-397)*) is provided after the discretization of the wing surface in a sufficient number of trapezoidal panels, which is evaluated through some convergence considerations that will be shown later. It is important to increase the number of panels in the areas of the wing where highest velocity and pressure gradients are expected, for example next to the tip of the wing. An appropriate method is to use the cosine law for the spanwise discretization (shown in *Figure 8*) and equal length elements for the chordwise splitting.

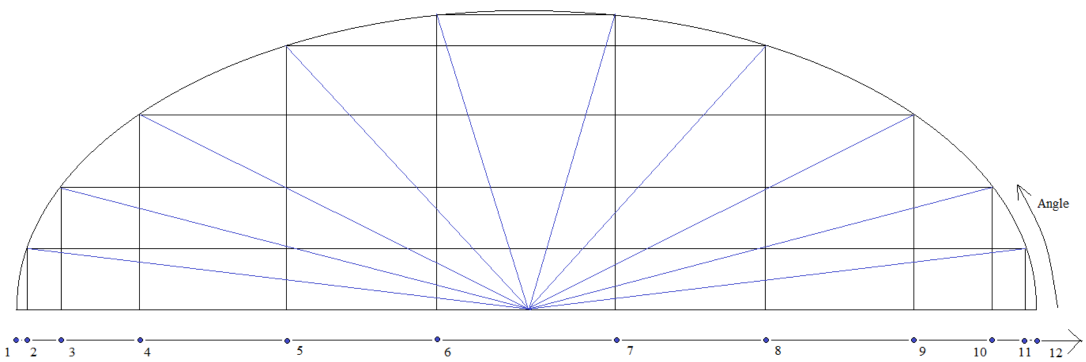

Figure 8: Example of cosine law use for grid refinement at wing tips.

At this point, each panel is represented by a singularity element which models its lifting properties. Horseshoe elements and vortex rings will be used for this steady case: both are built on the vortex singularity element, that is an irrotational source of vorticity.

According to *Katz and Plotkin [8] (pp. 380-397)*, the vortex ring is represented by four elements:

1. A straight bound vortex segment, modeling the lifting properties (BC).
2. A left vortex line (AB) parallel to the chord of the panel.
3. A right vortex line (CD) parallel to the chord of the panel.
4. A rear vortex (DA) closing the vortex ring.

In order to complete the definition of a panel, two remarkable points need to be defined, that are *Load Point* and *Collocation* or *Control Point*. The first one is positioned at the center of the quarter chord line, while *Collocation Point* is at the center of three-quarter chord line. Right hand rule and the segments defined before can be used for the evaluation of the normal vector for each panel, as shown in *Figure 9* and *Figure 10*.

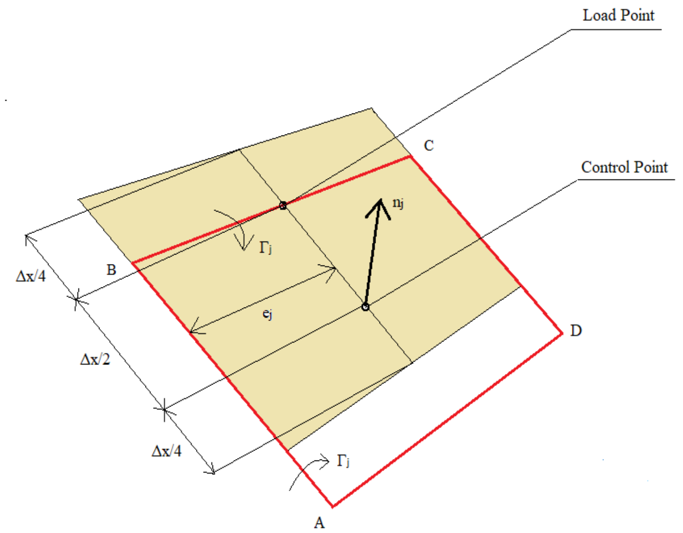

Figure 9: Vortex Ring element represented on the generic j-th trapezoidal panel of the wing.

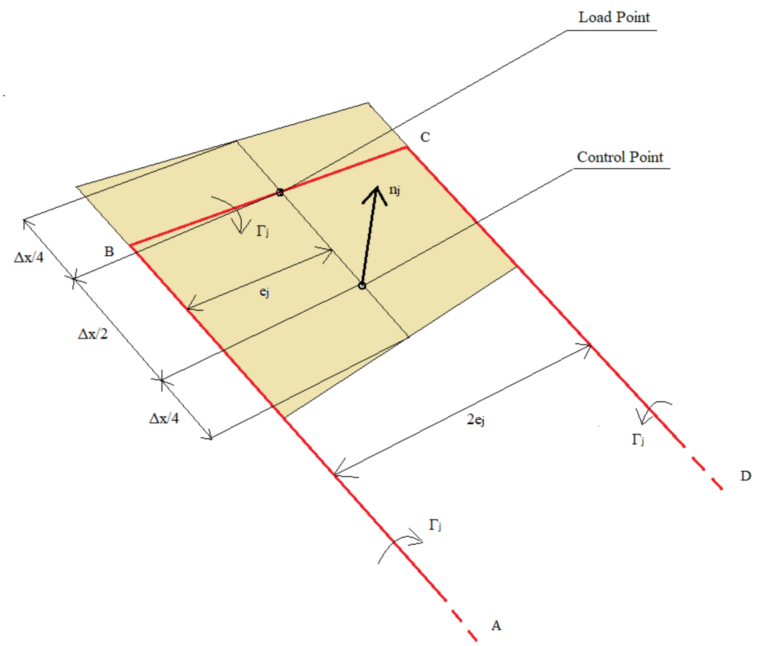

Figure 10: Horseshoe vortex element represented on the generic j-th trapezoidal panel of the wing.

The vortex strength Γ has a constant value for each segment of the vortex ring (or horseshoe in the other case) and it satisfies the two-dimensional Kutta condition on every panel. This means that the flow respects the condition of zero normal flow across the wing's solid surface (related to the normal vector to the panel) at the *Control Point*.

Vortex ring elements are used for all the panels of the wing except for the ones located on the trailing edge. In this case it is necessary to model the wake, thus horseshoe elements will be used: they are analogue to the vortex rings, but rear vortex is located at a distance from the straight bound one that is much greater than the length of segment BC. In this way, the rear vortex is still represented (this permits to satisfy the Helmholtz condition), but it is located so far that its influence on lift is negligible.

Another important condition for trailing panels is that the semi-infinite lines of AB and CD vortices are parallel to the streamlines (in this way no force will act on trailing vortices). It is now possible to explain the routines for wing lift evaluation from the singularities presented before.

One of the advantages of vortex ring elements is that they permit to evaluate lift on various wing planform shapes and with camber specification for panels. For this reason, a solution of the constant vortex line problem in three-dimensional space is presented. The velocity induced by a constant vortex Γ is evaluated through Biot-Savart's law:

$$\Delta\vec{V} = \frac{\Gamma}{4\pi}\frac{d\vec{l} \times \vec{r}}{r^3} \tag{2.10}$$

$d\vec{l}$ is the vortex segment and $\vec{r}$ is the distance from the point of the segment that is considered to P, where $\Delta\vec{V}$ is evaluated. Considering a finite length element in 3D space as shown in *Figure 11*, the velocity at an arbitrary point P is:

$$\vec{V}_{12} = \frac{\Gamma}{4\pi}\frac{\vec{r_1} \times \vec{r_2}}{|\vec{r_1} \times \vec{r_2}|^2}\vec{r_0} \cdot \left(\frac{\vec{r_1}}{r_1} - \frac{\vec{r_2}}{r_2}\right) \tag{2.11}$$

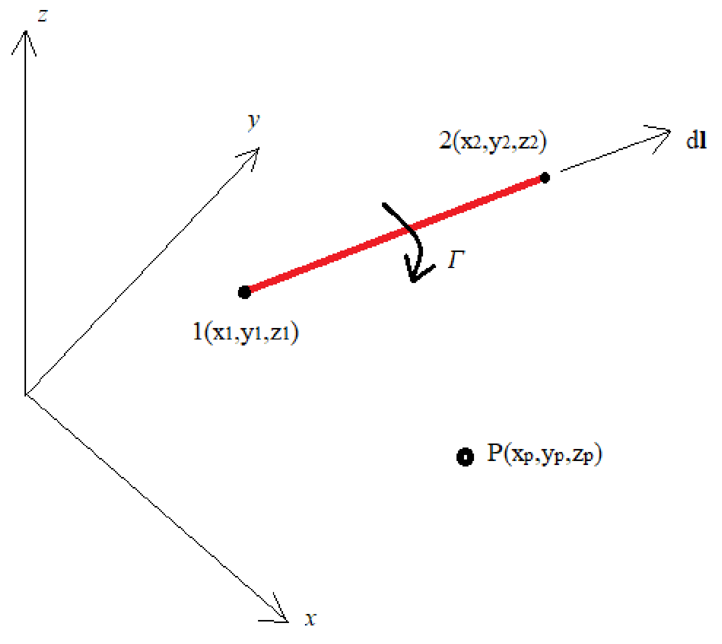

Figure 11: Generic constant vortex line segment in 3D space.

It is obvious that a vortex ring or a horseshoe element can be built as a combination of line elements. All the elements necessary for the evaluation of velocity in a generic P point are now available and can be implemented in a code solution routine.

The last step needed is the evaluation of the induced velocity at every *Collocation Point* by means of all the ring and horseshoe elements. An influence coefficient is calculated between the *Collocation Point* of the selected panel and the vortex elements of every other one, defining a matrix of coefficients with *NxN* dimensions, where *N* is the number of horseshoe and vortex ring total elements. Every element of the matrix represents the normal component of velocity (relative to the considered panel) induced on the *i-th Collocation Point* by the *j-th* unitary singularity element.

Once these evaluations have been fulfilled, the boundary condition of no normal flow across the panel at *Collocation Point* is imposed for every element of the discretized surface. The obtained equations are then:

$$\begin{cases} a_{11}\Gamma_1 + a_{12}\Gamma_2 + a_{13}\Gamma_3 + \cdots + a_{1N}\Gamma_N = -\overrightarrow{V_\infty} \cdot \overrightarrow{n_1} \\ a_{21}\Gamma_1 + a_{22}\Gamma_2 + a_{23}\Gamma_3 + \cdots + a_{2N}\Gamma_N = -\overrightarrow{V_\infty} \cdot \overrightarrow{n_2} \\ \cdots \\ a_{N1}\Gamma_1 + a_{N2}\Gamma_2 + a_{N3}\Gamma_3 + \cdots + a_{NN}\Gamma_N = -\overrightarrow{V_\infty} \cdot \overrightarrow{n_N} \end{cases} \tag{2.12}$$

In matrixial shape (*2.14*) this is equal to the system that must be solved to find the values of vortex singularities. It is important to see that the influence coefficients matrix depends only on geometrical parameters, while the right-hand side depends on the velocity of the undisturbed flow and on the geometry of panels (since the normal vector appears). The result is written in the following equation:

$$A_{ij}\Gamma = RHS \tag{2.13}$$

$$\begin{bmatrix} a_{11} & a_{12} & \cdots & a_{1N} \\ a_{21} & a_{22} & \cdots & a_{2N} \\ \cdots & \cdots & \cdots & \cdots \\ a_{N1} & a_{N2} & \cdots & a_{NN} \end{bmatrix} \begin{Bmatrix} \Gamma_1 \\ \Gamma_2 \\ \cdots \\ \Gamma_N \end{Bmatrix} = \begin{Bmatrix} -\overrightarrow{V_\infty} \cdot \overrightarrow{n_1} \\ -\overrightarrow{V_\infty} \cdot \overrightarrow{n_2} \\ \cdots \\ -\overrightarrow{V_\infty} \cdot \overrightarrow{n_N} \end{Bmatrix} \tag{2.14}$$

Once the values of vortex singularities have been obtained, lift and drag can be simply computed:

$$\Delta L_j = \rho V_\infty \Gamma_j e_j \tag{2.15}$$

$$\Delta D_j = -\rho w_{ind,j} \Gamma_j e_j \tag{2.16}$$

If the panels are located on the leading edge of the wing (first line of panels). Otherwise:

$$\Delta L_j = \rho V_\infty \left(\Gamma_j - \Gamma_{j-s}\right) e_j \tag{2.17}$$

$$\Delta D_j = -\rho w_{ind,j} \left(\Gamma_j - \Gamma_{j-s}\right) e_j \tag{2.18}$$

Where s is the number of panels for each line of the wing, while e_j is the spanwise dimension of the considered panel. This is due to the rear vortex segment of each vortex ring, that has a subtractive contribute to the lift of the following line of panels. *2.17* and *2.18* are used only for vortex rings, while *2.15* and *2.16* are valid for all panels when horseshoe vortices are used.

The evaluation of $w_{ind,j}$ is done by B_{ij} matrix: its terms are obtained using the influence velocity routine with the influence of bound vortex segments turned off. If the value of singularities has already been found:

$$\begin{Bmatrix} w_{ind,1} \\ w_{ind,2} \\ \cdots \\ w_{ind,N} \end{Bmatrix} = \begin{bmatrix} b_{11} & b_{12} & \cdots & b_{1N} \\ b_{21} & b_{22} & \cdots & b_{2N} \\ \cdots & \cdots & \cdots & \cdots \\ b_{N1} & b_{N2} & \cdots & b_{NN} \end{bmatrix} \begin{Bmatrix} \Gamma_1 \\ \Gamma_2 \\ \cdots \\ \Gamma_N \end{Bmatrix} \tag{2.19}$$

An example of wing discretization is reported in *Figure 12*, where all considerations made in the previous chapter are visually easier to understand and the panel numbering modes is shown.

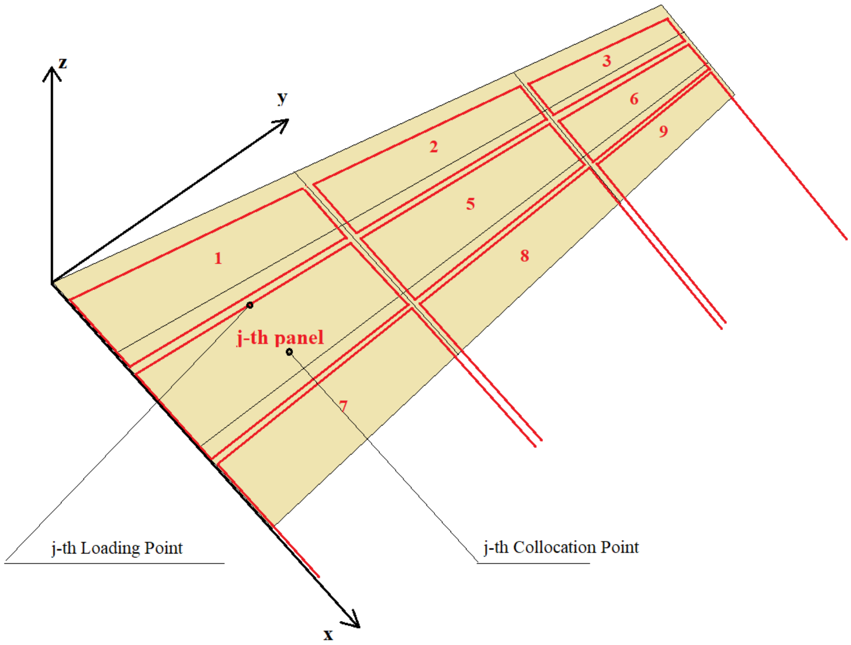

Figure 12: Simple example of wing discretization with horseshoe and ring vortex elements (panels numbering order is also shown).

2.4 Doublet Lattice Method (DLM)

If the unsteady contribution of aerodynamic forces must be evaluated, DLM is one of the most used finite elements methods for modeling oscillating lifting surfaces forces in subsonic flows. It reduces to VLM if the oscillating frequency is zero and it is based on the same panel's discretization and considerations. Some additional conditions would be added in high frequency problems, concerning the number of panels necessary to reduce errors.

The solution presented (*Rodden, Taylor and McIntosh [9]*) is an evolution of classic DLM method (developed by *Rodden, Giesing and Kalman*), where the original parabolic approximation of doublet distribution is replaced by a quartic polynomial one. The doublet element is represented by a single segment placed at the same place of the *BC* line used in VLM, as can be observed in *Figure 13*. As for the previous VLM theory, also DLM permits a three-dimensional distribution of panels and the introduction of a camber line (thus panels are not all parallel to the *x* axis of the wing), but this will not be considered in the code development phase.

If *w* is the normal wash for the considered surface in the case of harmonic motion, then its expression is:

$$\begin{aligned} w &= \overline{w}e^{i\omega t} \\ \Delta p &= \overline{\Delta p}e^{i\omega t} \end{aligned} \tag{2.20}$$

Where the amplitude of normal wash on the *i-th* panel due to the interaction with all the panel's singularities is evaluated through:

$$\overline{w_i} = \frac{1}{8\pi}\sum_{j=1}^{N} \overline{\Delta p_j}\,\Delta x_j$$
$$\overline{w_i} = \sum_{j=1}^{N} D_{ij}\overline{\Delta p_j} \tag{2.21}$$

The normal wash factor (D_{ij}) is thus given by equation *2.22*:

$$D_{ij} = \frac{\Delta x_j}{8\pi}\int_{-e_j}^{+e_j} K_{ij}\, d\hat{\eta}_j \tag{2.22}$$

Where K_{ij} is the kernel function, that will be evaluated in this chapter through some approximations. Before proceeding with this calculations, it is necessary to describe the reference systems used.

The local coordinate system $(\hat{x}, \hat{y})$ is located on the panel where the sending doublet distribution is located (panel *j*) and the origin is coincident with the middle point of the doublet segment (*BC*). The global coordinate system (x, y) is located on the wing root chord, as can be seen in *Figure 12* (reported in VLM chapter).

In the local coordinate system (*Figure 13*), $\hat{\eta}_j$ is the distance in *y* direction of the considered point from the *Load Point*. Considering that the general panel is trapezoidal, the angle between *y* axis and the doublet distribution is Λ_j. *x* position along the doublet segment can be defined as:

$$\hat{\xi}_j = \hat{\eta}_j \tan(\Lambda_j) \tag{2.23}$$

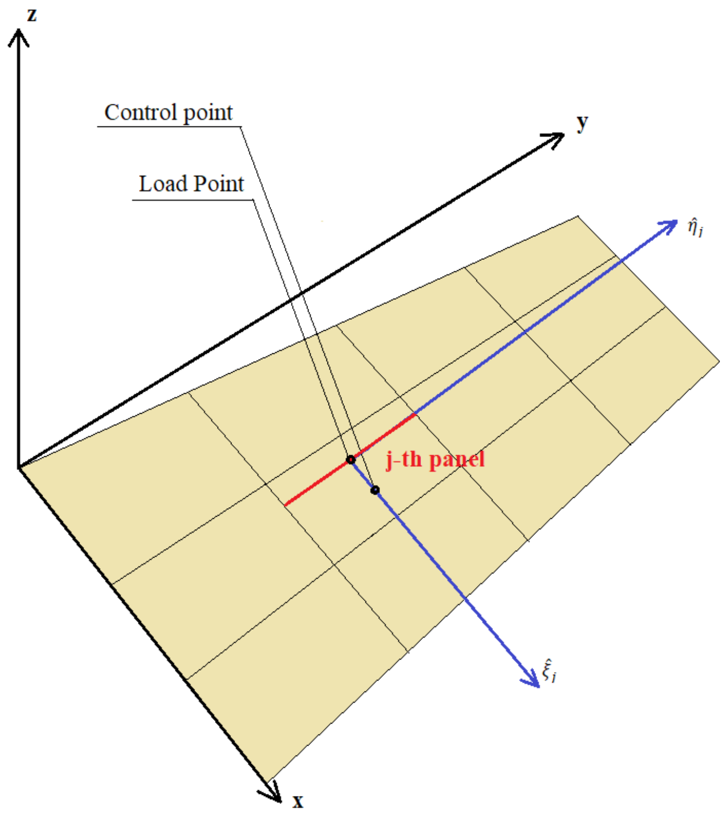

Figure 13: Representation of global and local coordinate systems for DLM.

The subscript i refers to the receiving panel, which is the one where the influence of all the other doublets is evaluated. The coordinates (x_i, y_i) and $(\hat{x}_i, \hat{y}_i)$ refer to the *Control Point* of the considered panel in the two reference systems defined before.

Now, all quantities involved in kernel function calculation are known. Thus:

$$D_{ij} = D_{0,ij} + D_{1,ij} + D_{2,ij} \tag{2.24}$$

Where the first term is the steady contribute, that could be expressed by its integral form, but is more conveniently obtained from Vortex Lattice Method evaluations; the second and the third one are defined by DLM, respectively by the planar and non-planar part of the Kernel (as will be seen in equation *2.26*). The term a_{ij} in equation *2.25*, is the one presented in equation *2.14*:

$$D_{0,ij} = \frac{1}{2}\Delta x_j a_{ij} \tag{2.25}$$

$$D_{1,ij} + D_{2,ij} = \frac{\Delta x_j}{8\pi}\int_{-e_j}^{+e_j}\left[\frac{\left(e^{-\frac{i\omega x_0}{V_\infty}}K_1 - K_{10}\right)T_1}{r^2} + \frac{\left(e^{-\frac{i\omega x_0}{V_\infty}}K_2 - K_{20}\right){T_2}^*}{r^4}\right]d\hat{\eta}_j \tag{2.26}$$

Where:

$$x_0 = \hat{x}_i - \hat{\xi}_j = \hat{x}_i - \hat{\eta}_j \tan(\Lambda_j) \tag{2.27}$$

$$R = \sqrt{{x_0}^2 + \beta^2 r^2} \tag{2.28}$$

$$y_0 = \hat{y}_i - \hat{\eta}_j \tag{2.29}$$

$$u_1 = \frac{MR - x_0}{\beta^2 r} \tag{2.30}$$

$$\beta = \sqrt{1 - M^2} \tag{2.31}$$

$$k_1 = \frac{\omega r}{V_\infty} \tag{2.32}$$

$$\begin{gathered} T_1 = \cos(\gamma_i - \gamma_j) \\ {T_2}^* = (z_0 \cos\gamma_i - y_0 \cos\gamma_i)(z_0 \cos\gamma_j \\ - y_0 \cos\gamma_j) \end{gathered} \tag{2.33}$$

$$r = \sqrt{{y_0}^2 + {z_0}^2} \tag{2.34}$$

M: Mach number, V_∞: unperturbed velocity, γ_i, γ_j: angles of incidence of receiving and sending panel respectively

According to *Blair M. [10] (pp. 79-90)* the expressions of K_1 and K_2, and those of I_1 and I_2 are the following:

$$I_1 = \int_{u_1}^{\infty}\frac{e^{-ik_1 u}}{(1+u^2)^{\frac{3}{2}}}du \tag{2.35a}$$

$$I_2 = \int_{u_1}^{\infty}\frac{e^{-ik_1 u}}{(1+u^2)^{\frac{5}{2}}}du \tag{2.35b}$$

$$K_1 = I_1 + \frac{Mr}{R}\frac{e^{-ik_1 u_1}}{(1+{u_1}^2)^{\frac{1}{2}}} \tag{2.36a}$$

$$K_2 = 3I_2 + \left[\frac{ik_1M^2r^2}{R^2}\right]\frac{e^{-ik_1u_1}}{(1+{u_1}^2)^{\frac{1}{2}}} + \frac{Mr}{R}\left[(1+{u_1}^2)\frac{\beta^2r^2}{R^2}+2 + \frac{Mru_1}{R}\right]\frac{e^{-ik_1u_1}}{(1+{u_1}^2)^{\frac{3}{2}}} \qquad (2.36b)$$

For the sake of brevity, the mathematical methods used for the evaluation of the expressions in equations *2.35* and *2.36* are not reported here, but they can be easily found in the work of *Blair [10]* cited before.

The integral that appears in the expression of $D_{1,ij}$ is evaluated through the following approximation:

$$D_{1,ij} = \frac{\Delta x_j}{8\pi}\Bigg\{\left[({\hat{y}_i}^2 - {\hat{z}_i}^2)A_1 + \hat{y}_iB_1 + C_1 + \hat{y}_i({\hat{y}_i}^2 - 3{\hat{z}_i}^2)D_1 + ({\hat{y}_i}^4 - 6{\hat{y}_i}^2{\hat{z}_i}^2 + {\hat{z}_i}^4)E_1\right]F + \left[\hat{y}_iA_1 + \frac{1}{2}B_1 + \frac{1}{2}(3{\hat{y}_i}^2 - {\hat{z}_i}^2)D_1 + 2\hat{y}_i({\hat{y}_i}^2 - {\hat{z}_i}^2)E_1\right]\ln\left(\frac{(\hat{y}_i - e_j)^2 + {\hat{z}_i}^2}{(\hat{y}_i + e_j)^2 + {\hat{z}_i}^2}\right) + 2e_j\left[A_1 + 2\hat{y}_iD_1 + \left(3{\hat{y}_i}^2 - {\hat{z}_i}^2 + \frac{1}{3}{e_j}^2\right)E_1\right]\Bigg\} \qquad (2.37a)$$

While $D_{2,ij}$ is obtained from:

$$\begin{aligned} D_{2,ij} = \frac{\Delta x_j}{16\pi{\hat{z}_i}^2}\Bigg\{ & \left[({\hat{y}_i}^2 + {\hat{z}_i}^2)A_2 + \hat{y}_iB_2 + C_2 + \hat{y}_i({\hat{y}_i}^2 + 3{\hat{z}_i}^2)D_2 + ({\hat{y}_i}^4 + 6{\hat{y}_i}^2{\hat{z}_i}^2 - 3{\hat{z}_i}^4)E_2\right]F \\ & + \frac{1}{(\hat{y}_i + e_j)^2 + {\hat{z}_i}^2}\{[({\hat{y}_i}^2 + {\hat{z}_i}^2)\hat{y}_i + ({\hat{y}_i}^2 - {\hat{z}_i}^2)e_j]A_2 + ({\hat{y}_i}^2 + {\hat{z}_i}^2 + \hat{y}_ie_j)B_2 \\ & + (\hat{y}_i + e_j)C_2 + [{\hat{y}_i}^4 - {\hat{z}_i}^4 - ({\hat{y}_i}^2 - 3{\hat{z}_i}^2)\hat{y}_ie_j]D_2 \\ & + [({\hat{y}_i}^4 - 2{\hat{y}_i}^2{\hat{z}_i}^2 - 3{\hat{z}_i}^4)\hat{y}_i + ({\hat{y}_i}^4 - 6{\hat{y}_i}^2{\hat{z}_i}^2 + {\hat{z}_i}^4)e_j]E_2\} \\ & - \frac{1}{(\hat{y}_i - e_j)^2 + {\hat{z}_i}^2}\{[({\hat{y}_i}^2 + {\hat{z}_i}^2)\hat{y}_i - ({\hat{y}_i}^2 - {\hat{z}_i}^2)e_j]A_2 + ({\hat{y}_i}^2 + {\hat{z}_i}^2 - \hat{y}_ie_j)B_2 \\ & + (\hat{y}_i - e_j)C_2 + [{\hat{y}_i}^4 - {\hat{z}_i}^4 - ({\hat{y}_i}^2 - 3{\hat{z}_i}^2)\hat{y}_ie_j]D_2 \\ & + [({\hat{y}_i}^4 - 2{\hat{y}_i}^2{\hat{z}_i}^2 - 3{\hat{z}_i}^4)\hat{y}_i - ({\hat{y}_i}^4 - 6{\hat{y}_i}^2{\hat{z}_i}^2 + {\hat{z}_i}^4)e_j]E_2\} \\ & + {\hat{z}_i}^2\ln\left(\frac{(\hat{y}_i - e_j)^2 + {\hat{z}_i}^2}{(\hat{y}_i + e_j)^2 + {\hat{z}_i}^2}\right)D_2 + 4{\hat{z}_i}^2\left[e_j + \hat{y}_i\ln\left(\frac{(\hat{y}_i - e_j)^2 + {\hat{z}_i}^2}{(\hat{y}_i + e_j)^2 + {\hat{z}_i}^2}\right)\right]E_2\Bigg\} \end{aligned} \qquad (2.37b)$$

A_1, B_1, C_1, D_1, E_1 are the polynomial coefficients for the fourth order approximation of $\left(e^{-\frac{i\omega x_0}{V_\infty}}K_1 - K_{10}\right)T_1$:

$$\left(e^{-\frac{i\omega x_0}{V_\infty}}K_1 - K_{10}\right)T_1 \cong {\hat{\eta}_j}^2A_1 + \hat{\eta}_jB_1 + C_1 + {\hat{\eta}_j}^3D_1 + {\hat{\eta}_j}^4E_1 = Q_1(\hat{\eta}_j) \qquad (2.38a)$$

A_2, B_2, C_2, D_2, E_2 are the polynomial coefficients for the fourth order approximation of $\left(e^{-\frac{i\omega x_0}{V\infty}} K_2 - K_{20}\right) {T_2}^*$:

$$\left(e^{-\frac{i\omega x_0}{V\infty}} K_2 - K_{20}\right) {T_2}^* \cong {\hat{\eta}_j}^2 A_2 + \hat{\eta}_j B_2 + C_2 + {\hat{\eta}_j}^3 D_2 + {\hat{\eta}_j}^4 E_2 = Q_2(\hat{\eta}_j) \qquad (2.38b)$$

The coefficients can be calculated through the values of $Q_{1,2}$ in five different points along BC segment, that are equally spaced. The expressions of polynomial coefficients are the same in the first and second case:

$$A_{1,2} = -\frac{\left[Q_{1,2}(-e_j) - 16Q_{1,2}\left(-\frac{e_j}{2}\right) + 30Q_{1,2}(0) - 16Q_{1,2}\left(\frac{e_j}{2}\right) + Q_{1,2}(e_j)\right]}{6{e_j}^2}$$

$$B_{1,2} = \frac{\left[Q_{1,2}(-e_j) - 8Q_{1,2}\left(-\frac{e_j}{2}\right) + 8Q_{1,2}\left(\frac{e_j}{2}\right) - Q_{1,2}(e_j)\right]}{6e_j}$$

$$C_1 = Q_{1,2}(0) \qquad (2.39)$$

$$D_{1,2} = -2\frac{\left[Q_{1,2}(-e_j) - 2Q_{1,2}\left(-\frac{e_j}{2}\right) + 2Q_{1,2}\left(\frac{e_j}{2}\right) - Q_{1,2}(e_j)\right]}{3{e_j}^3}$$

$$E_{1,2} = 2\frac{\left[Q_{1,2}(-e_j) - 4Q_{1,2}\left(-\frac{e_j}{2}\right) + 6Q_{1,2}(0) - 4Q_{1,2}\left(\frac{e_j}{2}\right) + Q_{1,2}(e_j)\right]}{3{e_j}^4}$$

The integral F is:

$$F = \int_{-e_j}^{+e_j} \frac{d\hat{\eta}_j}{\left(\hat{y}_i - \hat{\eta}_j\right)^2} = \frac{2e_j}{{\hat{y}_i}^2 - {e_j}^2} \qquad (2.40)$$

The missing elements for the problem resolution are the values of $Q_{1,2}$ at the five interpolation points:

$$Q_{1,2}(-e_j);\ Q_{1,2}\left(-\frac{e_j}{2}\right);\ Q_{1,2}(0);\ Q_{1,2}\left(\frac{e_j}{2}\right);\ Q_{1,2}(e_j)$$

From this point, only K_1 and $D_{1,ij}$ terms will be evaluated. That approximation of the term I_1, is obtained as described in *2.41* and *2.42*:

- $u_1 \geq 0$

$$I_1(u_1, k_1) = \left[1 - \frac{u_1}{(1 + {u_1}^2)^{\frac{1}{2}}} - ik_1 I_0(u_1, k_1)\right] e^{-ik_1 u_1} \qquad (2.41)$$

- $u_1 < 0$

$$I_1(u_1, k_1) = 2Re[I_1(0, k_1)] - Re[I_1(-u_1, k_1)] + iIm[I_1(-u_1, k_1)] \qquad (2.42)$$

The value of $I_0(u_1, k_1)$ is computed through:

$$I_0(u_1, k_1) = \int_{u_1}^{\infty} \left(1 - \frac{u}{(1 + u^2)^{\frac{1}{2}}}\right) e^{-ik_1 u} du \tag{2.43}$$

Where:

$$1 - \frac{u}{(1 + u^2)^{\frac{1}{2}}} = \sum_{s=1}^{n} a_s e^{-c_s u} \tag{2.44}$$

The integration of the previous term leads to the formulation:

$$I_0(u_1, k_1) = \sum_{s=1}^{n} \frac{a_s(c_s - ik_1)e^{-c_s u_1}}{{c_s}^2 + {k_1}^2} \tag{2.45}$$

The coefficients of the integral approximation, obtained by *Desmarais*, are written in *Table 3:*

a_1	0,000319759140
a_2	−0,000055461471
a_3	0,002726074362
a_4	0,005749551566
a_5	0,031455895072
a_6	0,106031126212
a_7	0,406838011567
a_8	0,798112357155
a_9	−0,417749229098
a_{10}	0,077480713894
a_{11}	−0,012677284771
a_{12}	0,001787032960
b	0,009054814793
$n = 12$	$c_s = \left(2^{\frac{s}{m}}\right) b$
$m = 1$	

Table 3: Coefficients for Desmarais approximation of I0 integral.

In the end, some considerations about panel discretization need to be done for DLM, since the chordwise length of each panel must satisfy the following condition:

$$\Delta x < \frac{0.08 V_\infty}{f} = \frac{0.08 V_\infty}{\omega} 2\pi \tag{2.46}$$

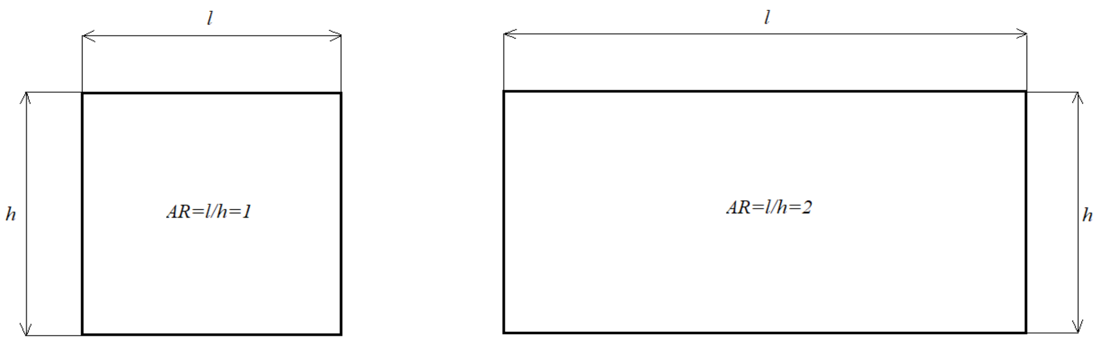

Figure 14: Aspect ratio definition for rectangular panels.

That can be obtained from the work done by *Rodden, Taylor and McIntosh [9]*. The limits imposed to dimensions of the panels are set through the Aspect Ratio (AR), which is defined as the ratio between the two dimensions of the panel (the numerator is usually the greatest length, while the denominator is the smallest one). The quadratic approximation of doublet distribution allows a smaller aspect ratio than the one allowed by the quartic one. The limits imposed by *Rodden, Taylor and McIntosh [9]* are reported in *Table 4*.

Quadratic polynomial approximation	Quartic polynomial approximation
$AR<3$	$AR<5$

Table 4: Limits for aspect ratio of DLM panels.

2.5 Aerodynamic Code Development and Verification

The previous chapters include all details that are necessary for the implementation of a solver able to evaluate lifting properties of a wing. The code developed specifically for the purposes of this work, is described in section *2.5.1.1*. A fundamental part is the verification of the obtained results, achieved through the comparison with experimental results or other computational aerodynamics codes.

2.5.1 Steady Aerodynamics Contribute (VLM)

The steady contribute is evaluated through Vortex Lattice Method. A code able to do this potential flux computations for a wide range of aerodynamic surfaces has been developed and its structure will be described in section *2.5.1.1*.

2.5.1.1 Main steady code development steps

The code developed for this analysis is divided into the following main sections:

Data input section (from command prompt), where the following parameters can be set:

1. The first three parameters are names that refer to the *.txt* file which contains profile coordinates. In each file the upper and the lower surface of the profile are discretized through a certain number of points.
2. The 4th, 5th, 6th parameters are the angle of attack, the freestream velocity and altitude for which the induced velocity, lift, and drag are evaluated in the *Post processing* section of the code.

3. The geometry of trapezoidal wings, defined by root chord, tip chord, span and sweep angle is set through the input lines going from the 6^{th} to the 10^{th}.
4. The 11^{th} and 12^{th} parameters define the number of panels for chordwise and spanwise discretization.
5. The last two parameters set some characteristics related to the spanwise position at which the wing profile changes as described by the first three ones.

This section also provides the generation of all the parameters related to the fluid flow (temperature, density…) with the hypothesis of ISA Atmosphere (*Appendix I*).

Profile Camber line generation section permits to obtain the camber line of each profile from upper and lower surfaces data. The use of *xFoil* for this calculations permits to increment the number of discretization points along the chord and to evaluate the pressure coefficient generated by the single profile and its polar curve, if necessary. *Table 5* reports the functions used in *xFoil* and their action: the code developed can autonomously open *xFoil* and execute all the operations needed.

Function	***Operations***
LOAD	Loads profile coordinates contained in the file which name is reported after the command.
PPAR	Permits to set a new parametrization for the upper surface, lower surface, and camber line of the profile.
ALFA	Sets the angle of attack of the profile for C_p evaluation.
CPWR	Writes pressure coefficient along the chord in the addressed file.
WRTC	Writes the coordinates of camber line in the addressed file.

Table 5: Main xFoil commands used in the described code.

The results provided by this section are a vector (*Centerline_X*) and a structure (*Centerline_Y*), that contain respectively the values of *x* and *y* coordinates of camber line points. The reference system adopted is the one represented in *Figure 15* and the number of discretization points for the camber line is equal to the number of chordwise panels plus one. It is important to notice that the structure *Centerline_Y* contains three vectors, corresponding to each profile loaded in the first section.

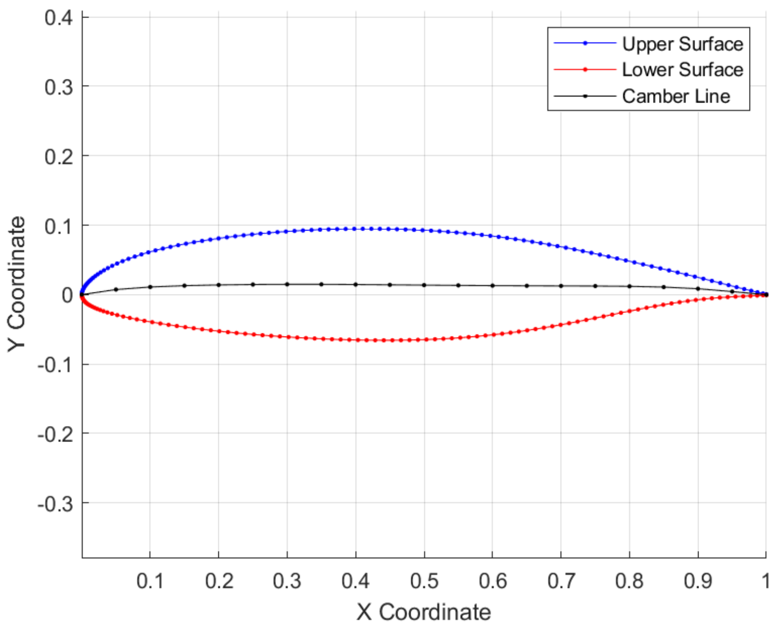

Figure 15: Syncro profile representation in its coordinate system.

Wing geometry construction section, that establishes and plots the main characteristics of the semi-wing. It can be observed that the trapezoidal semi-wing will be reflected only after the grid definition, due to the hypothesis of symmetric aircraft.

Grid generation section, where all the geometric properties of the grid are defined:

1. Each trapezoidal panel's vertices have three-dimensional coordinates that are named following the convention for the vortex singularity segments: the one corresponding to AB vortex, for example, has (*Xa, Ya, Za*) and (*Xb, Yb, Zb*) coordinates.
2. *Control point* and *Load point*, that are fundamental for the collocation of vortices and boundary conditions. They also have three dimensional coordinates, that are addressed to as: (*Control_point_x, Control_point_y, Control_point_z*).
3. The surface of each panel, that will be used later for lift and pressure evaluations.
4. *Normal vector*, which is fundamental to set boundary conditions and evaluate normal velocity.

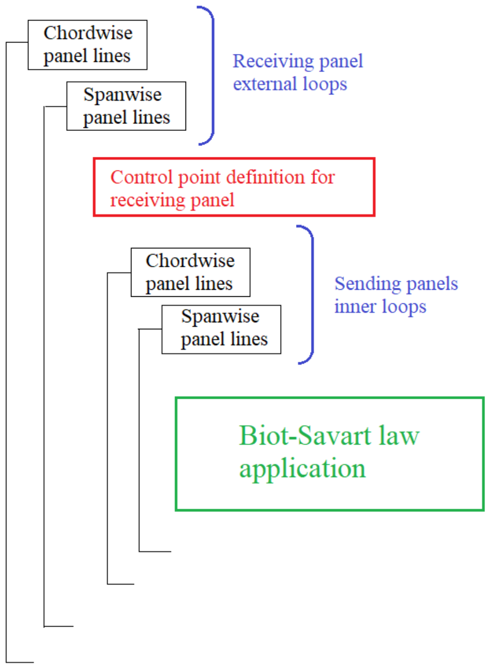

Figure 16: Code structure for the aerodynamic influence coefficients evaluation.

Aerodynamic influence coefficients evaluation section, where a_{ij} coefficients are computed. Four loops (*for* cycles) are used to evaluate the influence of each horseshoe and ring vortex on each other panel of the wing. This permits to define A_{ij} matrix, remembering that:

1. The first two loops define the receiving panel (*i-th*), on which the influence coefficient is evaluated.

2. The inner loops permit to scan all the panels (*j-th*) that in turn influence the receiving one.

The core of this calculations is the application of Biot-Savart's law for each vortex segment. The workflow used for the definition of each sending and receiving panel is schematized in *Figure 16*. Moreover, b_{ij} coefficients are evaluated considering only the influence of left and right vortices, that correspond to the segments AB and CD of each panel.

The number of panels set in the input section determines the computational time for influence coefficients evaluation. These values are directly proportional; thus, it is important to choose a number of singularities that is a trade-off between a good approximation and short calculation time. Some convergence considerations will be presented in the verification section (*2.5.1.3*).

Post processing section, in which lift, and induced drag are computed through *2.15, 2.16, 2.17, 2.18* equations. Moreover, it evaluates the polar curve for the wing and induced velocity. It is important to notice that the influence coefficients matrix is computed only once, while the angle of attack varies. Thus, the right-hand side term changes for each considered angle and then the singularities are evaluated through the matrix system presented in equation *2.13*:

$$\Gamma = [A_{ij}]^{-1}\, RHS \tag{2.47}$$

Grid points exportation section, that saves *Load* and *Control Points* (where boundary conditions are applied) in a *.mat* file, that will be essential for aeroelastic problems resolution, as explained in the following chapters.

2.5.1.2 Syncro wing geometrical properties

The wing of Syncro aircraft is trapezoidal, as stated in the introduction chapter of this work. Its main properties are listed in *Table 6*, including mean aerodynamic chord, root chord, tip chord and ailerons characteristics. Four profiles have been used along wingspan, that were developed properly for this aircraft.

The coordinates of upper and lower profile surfaces are stored in the *.txt* files reported in *Table 6*, while the zero sweep condition states that the quarter line of each profile along span is parallel to *y* axis.

<table>
<tr><th colspan="6">Wing main Surface</th></tr>
<tr><th colspan="2">Profile</th><th colspan="2">Y Coordinate</th><th colspan="2">Local chord</th></tr>
<tr><td colspan="2">Profilo_radice.txt</td><td colspan="2">0,000 m (Root)</td><td colspan="2">1,286 m</td></tr>
<tr><td colspan="2">Profilo_500.txt</td><td colspan="2">0,500 m</td><td colspan="2">1,214 m</td></tr>
<tr><td colspan="2">Profilo_2720.txt</td><td colspan="2">2,720 m</td><td colspan="2">0,974 m</td></tr>
<tr><td colspan="2">Profilo_tip.txt</td><td colspan="2">4,280 m (Tip)</td><td colspan="2">0,805 m</td></tr>
<tr><th colspan="2">Ailerons</th><th colspan="4">Flaps</th></tr>
<tr><td>Rotation angle</td><td>-27°/+15°</td><td colspan="2">Rotation angle</td><td colspan="2">0°/40°</td></tr>
<tr><td>Chord</td><td>24% of local chord</td><td colspan="2">Chord</td><td colspan="2">27% of local chord</td></tr>
<tr><td>Spanwise extension</td><td>from 2,720m to 4,280m</td><td colspan="2">Spanwise extension</td><td colspan="2">from 0,000m to 2,720m</td></tr>
</table>

Table 6: Aerodynamic geometry of Syncro wing.

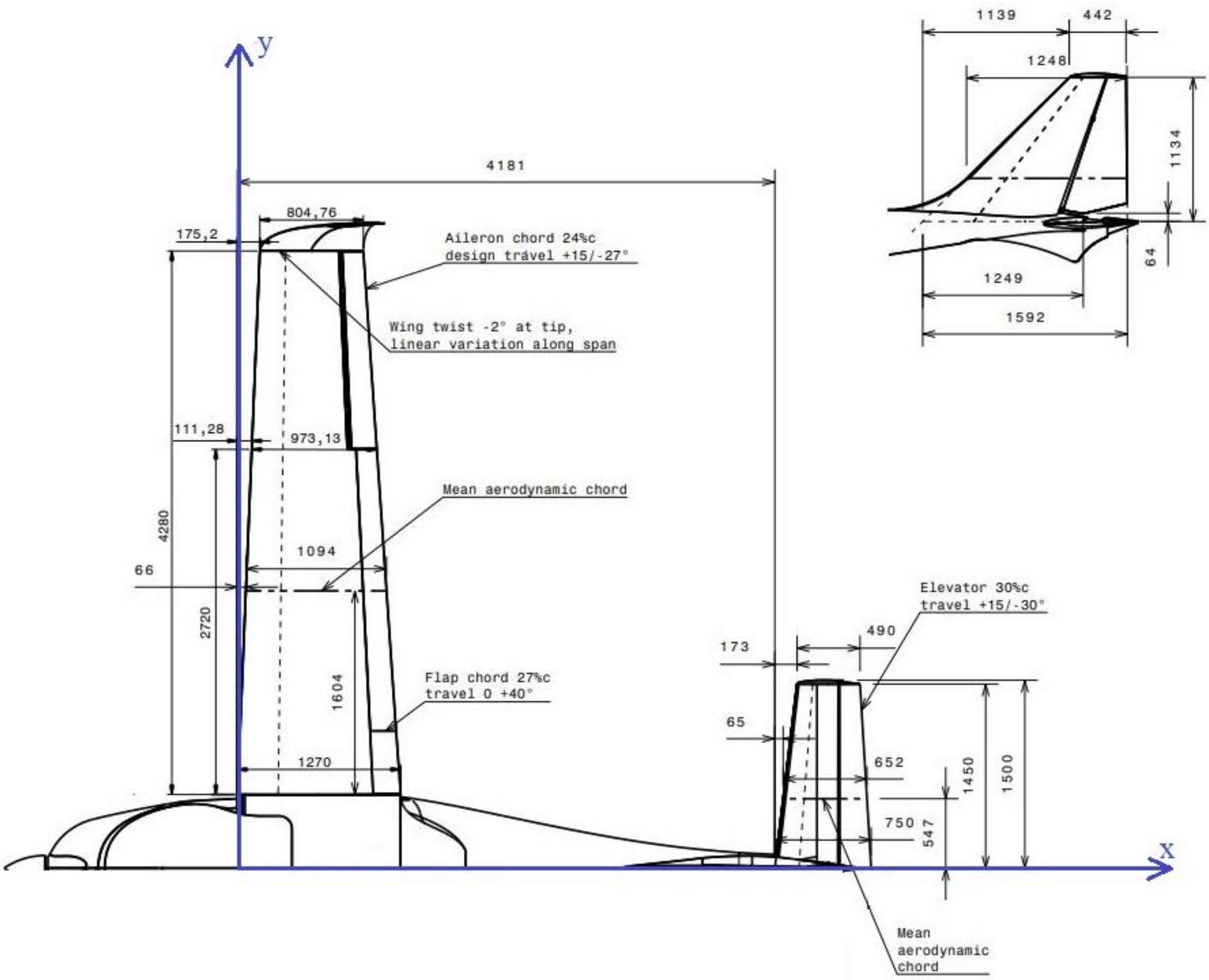

Figure 17: Wing and tail geometric properties for Syncro aircraft.

2.5.1.3 Verification on target analysis aircraft and convergence considerations

The instrument used for code verification is another Vortex Lattice Method code, named AVL (*Athena Vortex Lattice*), developed by *Mark Drela [11]*. The main differences between the two codes are related to the input methods and the output variables: the code developed in this work provides as an output the aerodynamic influence coefficients matrix, that is essential for Doublet Lattice Method evaluations. Moreover, the input method used in this case permits a quicker selection of parameters, although the number of variables is more limited and is adapt for simple geometry wings (for example the ones that are usually equipped on ultralight aircrafts category).

The first analysis that has been carried out regards the convergence of the results as far as the number of panels is changed. As the grid is thickened, the computational time increases exponentially because of the increased size of A_{ij} matrix and thus the number of variables of the problem is greater. A trade-off between the optimum computational time and a good approximation of the results is carried out. The results obtained show how the coefficients have an asymptotic behaviour as the number of panels grows: *Table 7* reports the percentual variability of C_L and C_D referred to the previous discretization step.

The compromise condition chosen is the following:

- 20 chordwise panels, equally spaced.
- 60 spanwise panels, with a cosine distribution.

Chordwise panels	***ΔCL***	***ΔCD***	***Spanwise panels***	***ΔCL***	***ΔCD***
3	14,682%	21,382%	***15***	0,758%	1,823%
5	9,144%	13,781%	***30***	0,434%	0,667%
8	5,066%	7,659%	***45***	0,166%	0,266%
12	3,108%	4,779%	***60***	0,131%	0,206%
17	1,962%	3,040%	***75***	0,080%	0,090%
23	1,199%	1,821%	***90***	0,059%	0,101%
30	1,142%	1,814%	***105***	0,037%	0,063%
40	---	---	***120***	---	---
Fixed spanwise panels number: ***60***			*Fixed chordwise panels number:* ***20***		

Table 7: Grid parameters convergence evaluations.

The data obtained has been used for the comparison with the equivalent wing configuration on AVL. In both cases, only three profiles have been used for simplicity, since *Profilo_radice.txt* and *Profilo_500.txt* have almost the same geometric properties.

Figure 18, and *Figure 19* describe the main steady aerodynamic properties of the wing, that have been compared with results obtained from *Athena Vortex Lattice [11]*. Considering a range of angles of attack that correspond to linear aerodynamics (stall is not represented by these codes), angular lift coefficients are:

$C_{L\alpha} = \dfrac{\partial C_L}{\partial \alpha} = 4{,}6903$	***Relative error: 0,6140%***
$C_{L\alpha,AVL} = \left(\dfrac{\partial C_L}{\partial \alpha}\right)_{AVL} = 4{,}6615$	

Table 8: Angular lift coefficient error evaluation

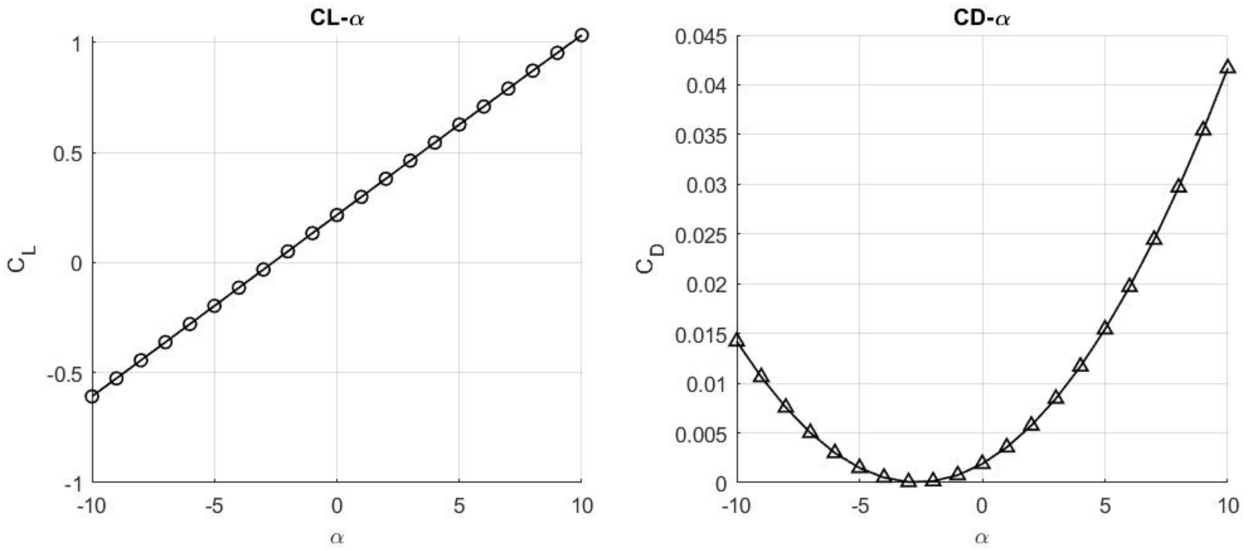

Figure 18: Lift and drag coefficients versus angle of attack.

The wing polar obtained with AVL is also plotted in *Figure 19*. As can be observed, the results obtained are coherent between the two codes; thus, from this chapter, the code can be considered valid for the calculations made for static divergence and flutter studies.

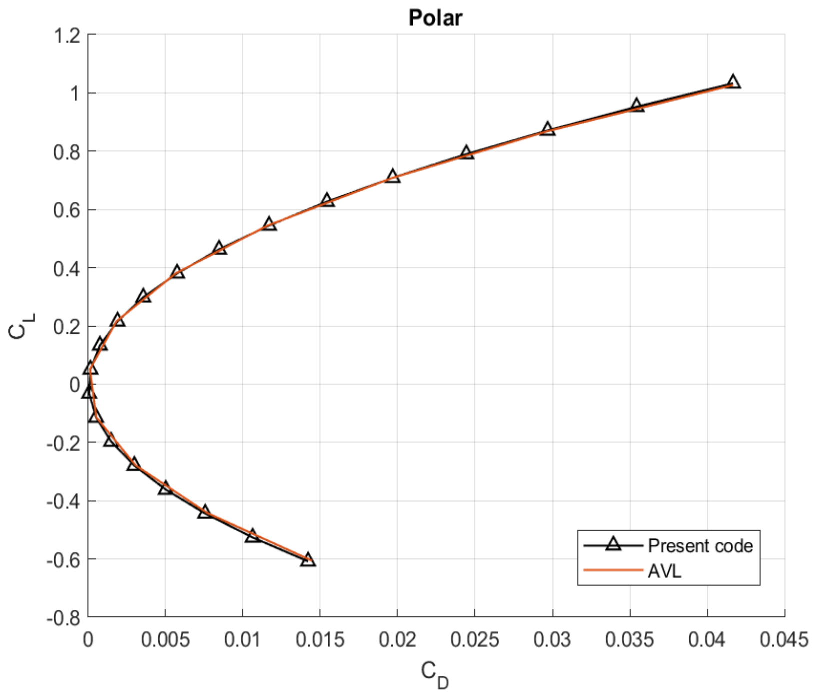

Figure 19: Polar curves from present code and Athena Vortex Lattice.

In the end, *Figure 20* shows the distribution of local lift coefficient along spanwise coordinate of the complete aircraft wing. The integration of lift along the span (y coordinate) permits to evaluate the lift coefficient for the considered angle of attack.

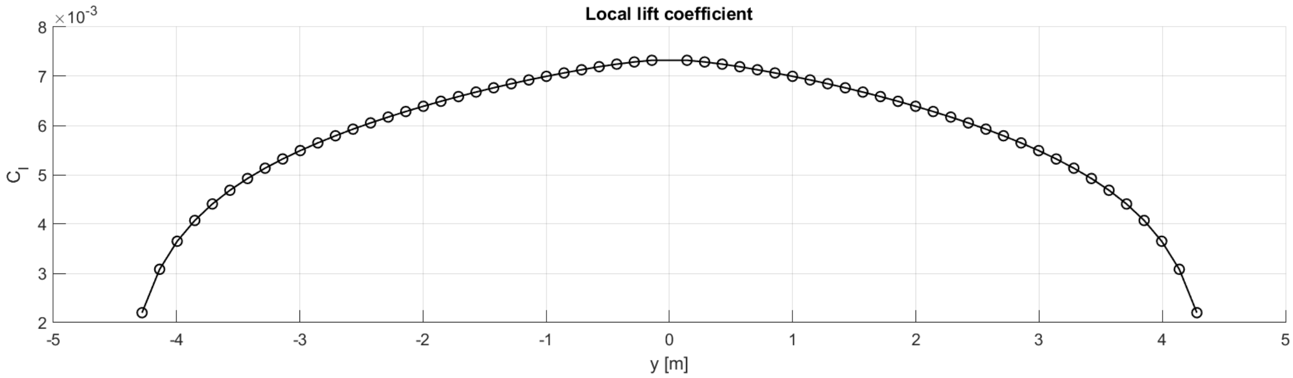

Figure 20: VLM lift coefficient distribution along span coordinate (angle of attack 2°).

2.5.1.4 Wing symmetry code simplifications

VLM code presented in chapter *2.5.1.1* can be improved by considering only one semi-wing in lift and induced drag computations. This is possible because the influence coefficients of the not-represented semi-wing are obtained through the reflection of the other one: only the sign inversion of y coordinates is necessary. In the end, the coefficients of the two semi-wings are summed and the result is a smaller influence coefficients matrix; The influence coefficients matrix building process has been executed in different conditions and the conclusions reached are:

- Computational time differences are neglectable for poor mesh grids, where the solution time is so short that the advantages of the half-wing model are inconsistent.
- The semi-wing model is necessary for some analysis carried out in the next chapters, where the aerodynamic model must be coupled with the semi-wing beam structure.

Mesh grid		*Complete Wing computational time [s]*	*Semi-wing computational time [s]****
Chordwise	*Spanwise*		
5	20	0,606	0,299
10	40	1,676	1,284
20	80	17,967	10,842
25	100	38,698	23,842

Table 9: Computational times comparison between semi-wing and complete wing VLM model.

****Spanwise panels number is half the one reported for the complete wing, thus the results of the two models for lift and induced drag are exactly coincident.*

2.5.2 Unsteady Aerodynamic Contribute (DLM)

The value of z coordinate for each panel has not been considered in Doublet Lattice Method evaluations, since its value is usually much smaller than the other coordinates for wing profiles with limited camber. As underlined by *Blair [10]* in his work, non-planar contributes complicate the calculations, since $D_{2,ij}$ term is introduced. Nevertheless, the previous hypothesis brings to the simplification of equation *2.48*:

$$\lim_{z_0 \to 0} T_2{}^* = \lim_{z_0 \to 0} (z_0 \cos\gamma_i - y_0 \sin\gamma_i)(z_0 \cos\gamma_j - y_0 \sin\gamma_j) = 0 \quad (2.48)$$

The doublet contribute will reduce to the following expression, that is a simplification of equation *2.26*:

$$D_{1,ij} = \frac{\Delta x_j}{8\pi} \int_{-e_j}^{+e_j} \frac{\left(e^{-\frac{i\omega x_0}{V_\infty}} K_1 - K_{10}\right) T_1}{r^2} d\hat{\eta}_j \tag{2.49}$$

Where $T_1 = 1$.

2.5.2.1 Main Unsteady Code Development Steps

Doublets contribute to lift is evaluated through an additional section added to the VLM code. This is possible because the grid used for each panel is the same and the collocation of the doublet line is at the quarter line. The modified code sections are the following:

Aerodynamic influence coefficients evaluation section, where a new subroutine is introduced, as it is necessary to evaluate the coefficients of D matrix. This subroutine is constituted by the equations presented in the first part of the present chapter, that permit to sum D_1 values to D_0 ones (*2.50*): as stated before, the steady contribute is calculated through VLM, while the unsteady one becomes null if the oscillation frequency is zero. The structure of this section is reported in *Figure 21*, that shows how an additional inner loop can be added to evaluate the effect of different reduced oscillation frequencies on the wing in a single code execution, but with a fast increase in computational time.

$$D_{ij} = D_{0,ij} + D_{1,ij} = \frac{1}{2}\Delta x_j a_{ij} + \frac{\Delta x_j}{8\pi} \int_{-e_j}^{+e_j} \left[\frac{\left(e^{-\frac{i\omega x_0}{V_\infty}} K_1 - K_{10}\right) T_1}{r^2} \right] d\hat{\eta}_j \tag{2.50}$$

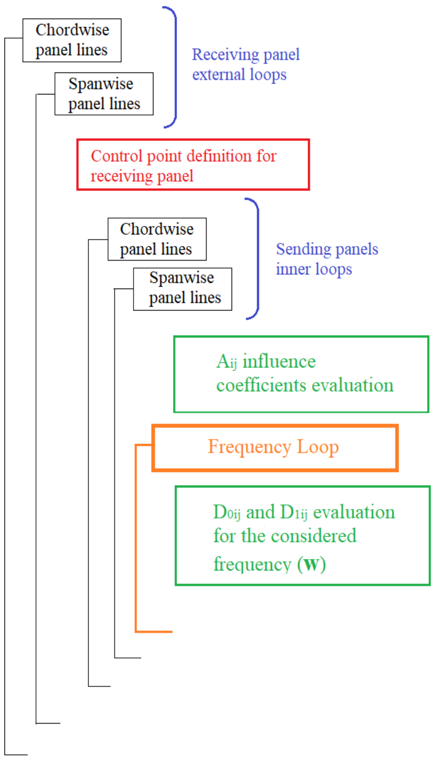

The values of doublet influence coefficients matrices for every frequency are thus saved in a proper variable, that is recalled in the post processing section. The central section of DLM code can be integrated in the previously described VLM code.

The values of reduced frequency are an input of the problem and will be set through some specific evaluations: the range of variation and the step between two contiguous frequencies will be defined in flutter chapter.

Post processing section: for each value of input frequency the pressure coefficient on panels can be properly evaluated through the resolution of the system of equations presented in equation *2.51*:

$$\{C_P\} = [D]^{-1}\{w\} \tag{2.51}$$

Where $\{w\}$ is the vector of dimensionless normal wash for each panel of the wing. In the steady case it differs from the unsteady one because it has only the real part (the imaginary contribute is due to the wing motion/deformation). This term will be defined more precisely in the next chapters since the deformation of the wing is obtained through the free vibrational problem resolution.

Figure 21: Code structure for unsteady aerodynamic influence coefficients evaluation.

2.5.2.2 DLM code verification

Since it is difficult to find data for unsteady aerodynamic analysis, the present code results have been compared with the ones obtained by *Forschling, H., Triebstein, H., Wagener J. [19],* and *Rowe, W.S., Sebastian, J.D., Petrarca, J.R. [20]*. The test case analysis concerns a simple rectangular wing with an oscillating flap, whose characteristics are known and are reported in *Table 10*:

Test semi-wing properties			
Span	$s = 0{,}88\ m$	Sweep angle	$\Lambda = 25°$
Chord	$c = 0{,}60\ m$	Dihedral angle	$\Gamma = 0°$
Aileron Chord	$ac = 0{,}17\ m$	Aileron deflection	$\alpha = 0{,}66°$
Aileron Span	$as = 0{,}47\ m$	Reduced oscillation frequency	$k = 0{,}372$

Table 10: DLM test semi-wing properties.

Figure 22 represents the configuration of the semi-wing, where the angle of attack is equal to zero, while the aileron oscillates with the established frequency. The profile selected for the static aerodynamic contribute is a symmetrical profile, thus all panels are located on the *z=0* plane. The selected discretization considers 20 chordwise panels and 30 spanwise panels, to obtain a sufficiently accurate representation. Results will be presented as distributions of pressure coefficient along the chord of the semi-wing.

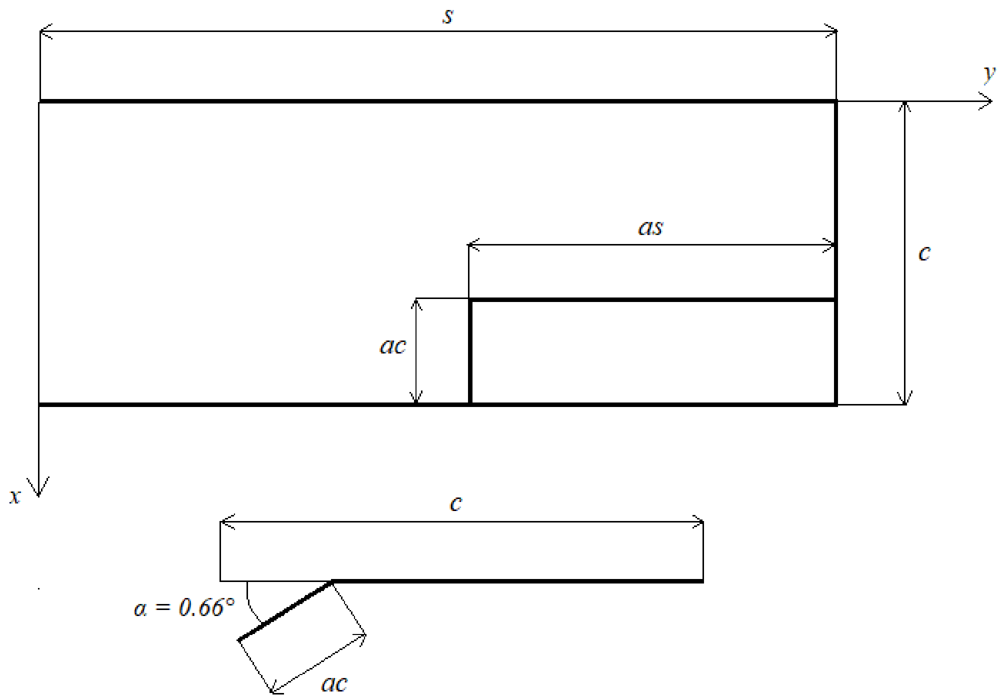

Figure 22: Test semi-wing and aileron geometry.

The results obtained for the considered reduced frequency are reported in *Figure 23*, where the real and imaginary part of pressure coefficient can be observed. Moreover, the unsteady real part of C_P is compared to the steady result, underlining the reduction of pressure due to the oscillating aileron surface. The real part of C_P shows a peak that is located at the connection between the aileron and the remaining part of the wing. A secondary peak can be observed at the leading edge of the wing.

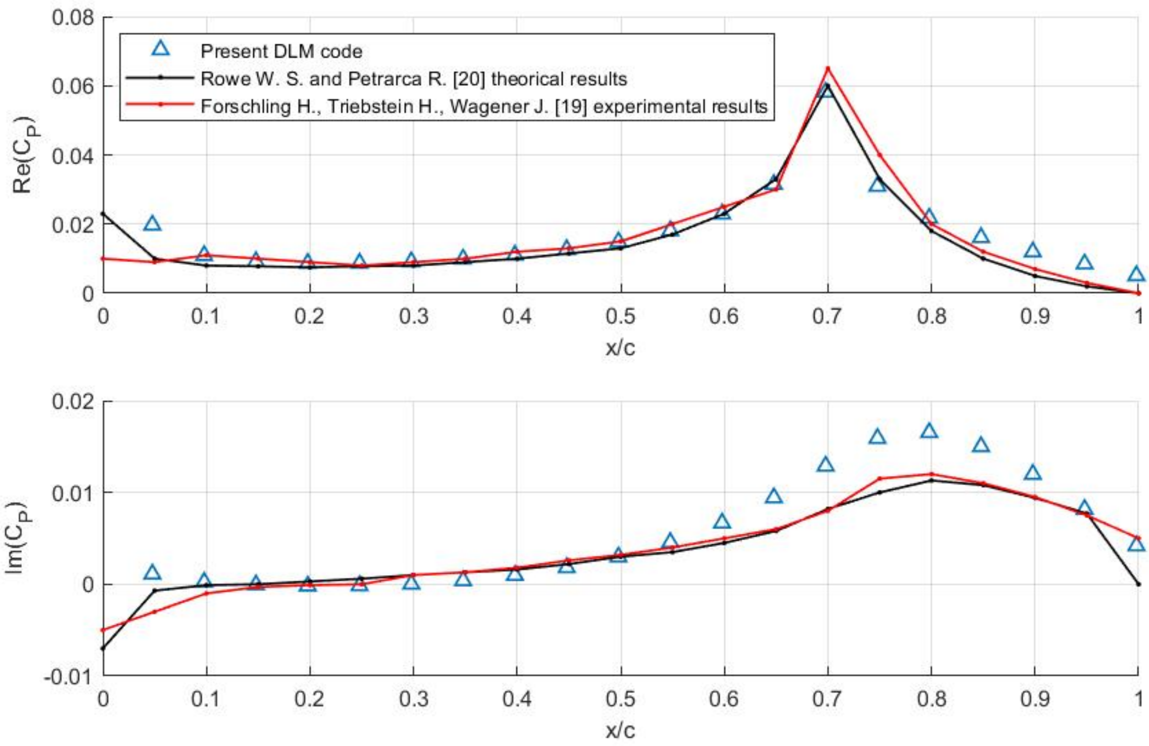

Figure 23: Test semi-wing pressure coefficient results.

2.5.2.3 Unsteady Aerodynamic Properties of Syncro Wing

Following the rules presented in the previous chapters regarding aspect ratio and the number of panels necessary for computations at a defined airspeed, the hereafter presented grid could be selected for DLM application on the semi-wing of Syncro aircraft:

1. 20 chordwise panels, that are enough to satisfy the condition in equation *2.52* for a reasonable range of reduced oscillation frequencies ($b = \frac{c_{mean}}{2} = \frac{1{,}094}{2} = 0{,}547$, half of the mean aerodynamic chord). The estimation of maximum reduced frequency is made on the worst conditions, that is at the root chord of the wing.

$$\begin{gathered} \Delta x < \frac{0{,}08V_\infty}{f} = \frac{0{,}08V_\infty}{\omega}2\pi = \frac{0{,}08V_\infty}{\frac{kV_\infty}{b}}2\pi = \frac{0{,}08b}{k}2\pi \\ k < \frac{0{,}08b}{\Delta x}2\pi = \frac{0{,}08b}{0{,}0634}2\pi = 4{,}3368 \end{gathered} \tag{2.52}$$

2. 30 spanwise panels, that are equally spaced to respect the aspect ratio conditions with a relatively small number of panels. In this case, the worst condition if found at the tip of the wing, where the panels are more stretched. Nevertheless, the results obtained are compatible with the imposed conditions for quartic polynomial Doublet Lattice Method, as shown in *2.53*.

$$AR = \frac{l}{h_{min}} = \frac{0{,}1430}{0{,}0402} = 3{,}557 < 5{,}0 \tag{2.53}$$

The reason why a cosine law is not used for spanwise discretization is that DLM evaluations need to respect the conditions described in *2.52* and *2.53*. The use of a variable spanwise length of the panels brings to a great number of chordwise ones to satisfy *AR* condition and to a much greater computational time. The equally spaced discretization is thus the more suitable for simple wing geometries.

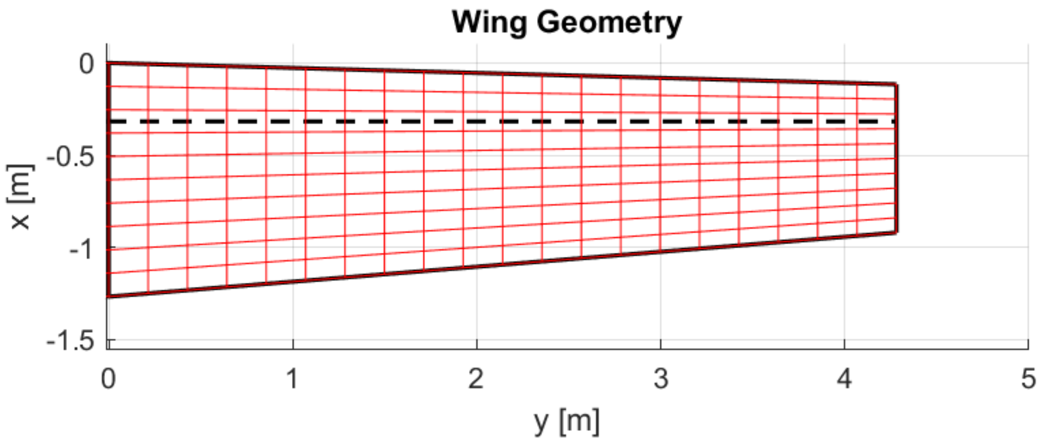

Figure 24: Semi-wing geometry and mesh representation for Syncro aircraft.

Even thought that this would be a suitable discretization, solution times must be considered in flutter analysis resolution, thus a less accurate grid will be built in the following chapters (at least in the first steps of the study, when a wide range of cases is the main target).

Chapter 3

Structural models

Aeroelasticity studies go through the analysis of static deformation and free vibrational modes of wing structure, that are then coupled with aerodynamics. The elements used to represent the wing structure in this work are beams (characterized by a 1D geometry), because the geometry has a predominant dimension. This is usually the y axis, while the cross section of the beam lies in a plane parallel to the x-z one and has an arbitrary shape. The following pages will resume the main points of the theories used in this work: the focus is set on Finite Elements methods.

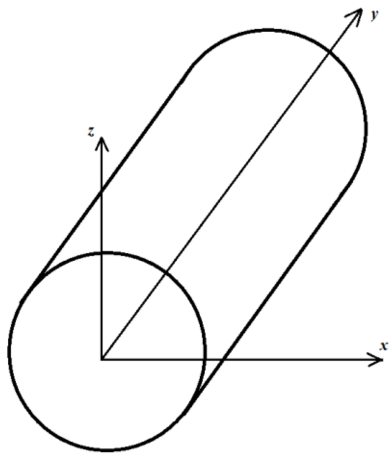

Figure 25: Reference system for a beam element with circular cross section.

3.1 Stresses and Displacements, Geometrical Relations, and Constitutive Equations

First, it is important to define the displacement field for each structural variable in 3D space, which is time dependent in the most general case. Its expression is reported in equation *3.1*:

$$\vec{u}(x,y,z,t) = \begin{Bmatrix} u_x(x,y,z,t) \\ u_y(x,y,z,t) \\ u_z(x,y,z,t) \end{Bmatrix} \tag{3.1}$$

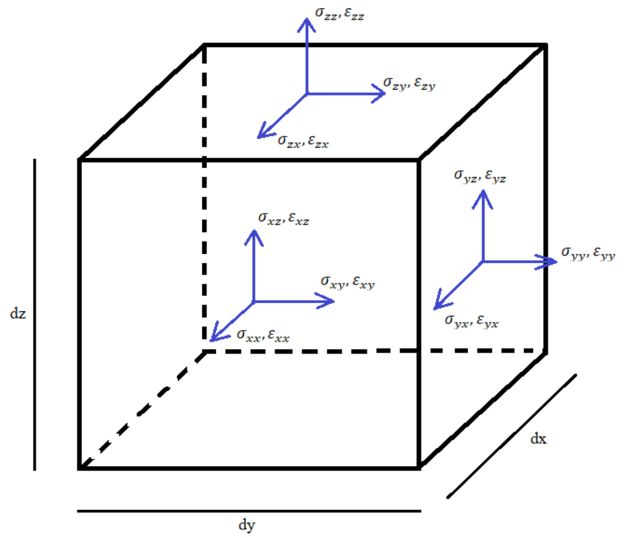

At the same time, stresses and deformations vectors are defined through equation *3.2*. Their components are only six because of the hypothesis of angular momentum equilibrium, which implies a symmetry condition for the cross components addressed to in equation *3.3*. The results presented in this pages are obtained following *Carrera E., Cinefra M. [12] (chapters 3 and 4).*

Figure 26: Representation of stress and strain components in 3D space.

$$\begin{gathered} \vec{\sigma} = \{\sigma_{yy}, \sigma_{xx}, \sigma_{zz}, \sigma_{xz}, \sigma_{yz}, \sigma_{xy}\}^T \\ \vec{\varepsilon} = \{\varepsilon_{yy}, \varepsilon_{xx}, \varepsilon_{zz}, 2\varepsilon_{xz}, 2\varepsilon_{yz}, 2\varepsilon_{xy}\}^T \end{gathered} \tag{3.2}$$

$$\begin{gathered} \sigma_{ij} = \sigma_{ji}, i \neq j \\ \varepsilon_{ij} = \varepsilon_{ji}, i \neq j \end{gathered} \tag{3.3}$$

Figure 26 displays the stress and strain components in 3D space, addressing to the surfaces on which they act (the first subscript refers to the surface through its orthogonal vector) and the direction (the second subscript refers to the direction of the stress/strain). The various components can be divided into two sub-vectors, that refer to the beam cross section and to the *y* direction respectively:

$$\begin{gathered}\vec{\sigma}_p = \{\sigma_{zz}, \sigma_{xx}, \sigma_{xz}\}^T \\ \vec{\varepsilon}_p = \{\varepsilon_{zz}, \varepsilon_{xx}, 2\varepsilon_{xz}\}^T = \{\varepsilon_{zz}, \varepsilon_{xx}, \gamma_{xz}\}^T\end{gathered} \tag{3.4}$$

$$\begin{gathered}\vec{\sigma}_n = \{\sigma_{yz}, \sigma_{xy}, \sigma_{yy}\}^T \\ \vec{\varepsilon}_n = \{2\varepsilon_{yz}, 2\varepsilon_{xy}, \varepsilon_{yy}\}^T = \{\gamma_{yz}, \gamma_{xy}, \varepsilon_{yy}\}^T\end{gathered} \tag{3.5}$$

Where the following notation has been introduced:

$$\gamma_{ij} = 2\varepsilon_{ij}, i \neq j$$

3.1.1 Geometrical relations

The displacements and deformation vectors are related through equation *3.6*, considering small displacements and thus linear relations:

$$\begin{gathered}\varepsilon_{zz} = u_{z,z} \\ \varepsilon_{xx} = u_{x,x} \\ \gamma_{xz} = 2\varepsilon_{xz} = u_{x,z} + u_{z,x} \\ \gamma_{yz} = 2\varepsilon_{yz} = u_{y,z} + u_{z,y} \\ \gamma_{xy} = 2\varepsilon_{xy} = u_{x,y} + u_{y,x} \\ \varepsilon_{yy} = u_{y,y}\end{gathered} \tag{3.6}$$

The same expressions can be formulated in an alternative way through the following differential operators in matrixial form:

$$\boldsymbol{D}_p = \begin{bmatrix} 0 & 0 & \frac{\partial}{\partial z} \\ \frac{\partial}{\partial x} & 0 & 0 \\ \frac{\partial}{\partial z} & 0 & \frac{\partial}{\partial x} \end{bmatrix}; \boldsymbol{D}_{np} = \begin{bmatrix} 0 & \frac{\partial}{\partial z} & 0 \\ 0 & \frac{\partial}{\partial x} & 0 \\ 0 & 0 & 0 \end{bmatrix}; \boldsymbol{D}_{ny} = \begin{bmatrix} 0 & 0 & \frac{\partial}{\partial y} \\ \frac{\partial}{\partial y} & 0 & 0 \\ 0 & \frac{\partial}{\partial y} & 0 \end{bmatrix} \tag{3.7}$$

That permit to obtain the result presented in equation *3.8*:

$$\begin{cases} \vec{\varepsilon}_p = \boldsymbol{D}_p \vec{u} \\ \vec{\varepsilon}_n = \boldsymbol{D}_n \vec{u} = \boldsymbol{D}_{np} \vec{u} + \boldsymbol{D}_{ny} \vec{u} \end{cases} \tag{3.8}$$

3.1.2 Constitutive equations

On the other hand, constitutive equations relate stresses and deformations through the material stiffness matrix of elastic coefficients, that can be defined in different reference systems (*Carrera E., Cinefra M. [12], chapter 6*). At first, the material reference system will be used, in which the coordinates are identified as (1, 2, 3):

$$\begin{gathered}\vec{\sigma}_m = \{\sigma_{33}, \sigma_{22}, \sigma_{11}, \sigma_{21}, \sigma_{31}, \sigma_{23}\}^T \\ \vec{\varepsilon}_m = \{\varepsilon_{33}, \varepsilon_{22}, \varepsilon_{11}, 2\varepsilon_{21}, 2\varepsilon_{31}, 2\varepsilon_{23}\}^T\end{gathered} \tag{3.9}$$

The compact form of constitutive equation can be found in equation *3.10*, that introduces the *6x6* material stiffness matrix of elastic coefficients:

$$\vec{\sigma}_m = \boldsymbol{C}_m \vec{\varepsilon}_m \tag{3.10}$$

Many hypothesis can be applied to $\boldsymbol{C}_m$ matrix, that has different levels of complexity depending on the beam material. The general form has 21 independent coefficients, because the matrix is symmetric. The following equations present the most common simplifications made on material properties:

Anisotropic material

$$\boldsymbol{C}_m = \begin{bmatrix} C_{33} & C_{23} & C_{13} & C_{43} & C_{53} & C_{63} \\ C_{23} & C_{22} & C_{12} & C_{42} & C_{52} & C_{62} \\ C_{13} & C_{12} & C_{11} & C_{41} & C_{51} & C_{61} \\ C_{43} & C_{42} & C_{41} & C_{44} & C_{45} & C_{46} \\ C_{53} & C_{52} & C_{51} & C_{45} & C_{55} & C_{56} \\ C_{63} & C_{62} & C_{61} & C_{46} & C_{56} & C_{66} \end{bmatrix} \tag{3.11}$$

Orthotropic material

$$\boldsymbol{C}_m = \begin{bmatrix} C_{33} & C_{23} & C_{13} & 0 & 0 & 0 \\ C_{23} & C_{22} & C_{12} & 0 & 0 & 0 \\ C_{13} & C_{12} & C_{11} & 0 & 0 & 0 \\ 0 & 0 & 0 & C_{44} & 0 & 0 \\ 0 & 0 & 0 & 0 & C_{55} & 0 \\ 0 & 0 & 0 & 0 & 0 & C_{66} \end{bmatrix} \tag{3.12}$$

Isotropic material

$$\boldsymbol{C}_m = \begin{bmatrix} C_{11} & C_{13} & C_{13} & 0 & 0 & 0 \\ C_{13} & C_{11} & C_{13} & 0 & 0 & 0 \\ C_{13} & C_{13} & C_{11} & 0 & 0 & 0 \\ 0 & 0 & 0 & C_{66} & 0 & 0 \\ 0 & 0 & 0 & 0 & C_{66} & 0 \\ 0 & 0 & 0 & 0 & 0 & C_{66} \end{bmatrix} \tag{3.13}$$

If the coefficients are constant along the structure, the material is considered *homogeneous*, while if the properties change from point to point it is *heterogeneous*. In the orthotropic and isotropic case, the coefficients are defined in relation to Young's modulus, Shear modulus and Poisson's ratio in each direction of the material's reference system (*Table 11* summarizes the definitions of all the coefficients):

Orthotropic material	$C_{11} = \dfrac{E_1(1-\nu_{23}\nu_{32})}{\Delta}$ $C_{22} = \dfrac{E_2(1-\nu_{13}\nu_{31})}{\Delta}$ $C_{33} = \dfrac{E_3(1-\nu_{12}\nu_{21})}{\Delta}$	$C_{12} = C_{21} = \dfrac{E_1(\nu_{21}+\nu_{23}\nu_{31})}{\Delta}$ $C_{13} = C_{31} = \dfrac{E_1(\nu_{31}+\nu_{21}\nu_{32})}{\Delta}$ $C_{23} = C_{32} = \dfrac{E_2(\nu_{32}+\nu_{12}\nu_{31})}{\Delta}$	$C_{44} = G_{21}$ $C_{55} = G_{31}$ $C_{66} = G_{23}$
	$\Delta = 1-\nu_{12}\nu_{21}-\nu_{13}\nu_{31}-\nu_{23}\nu_{32}-\nu_{12}\nu_{23}\nu_{31}-\nu_{13}\nu_{21}\nu_{32}$		
Isotropic material	$C_{11} = \dfrac{(1-\nu)E}{(1+\nu)(1-2\nu)}$	$C_{13} = \dfrac{\nu E}{(1+\nu)(1-2\nu)}$	$C_{66} = \dfrac{E}{2(1+\nu)}$

Table 11: Definition of material stiffness matrix coefficients for orthotropic and isotropic materials.

Where E_1, E_2, E_3 are the Young's moduli along the three directions of the reference system and G_{21}, G_{31}, G_{23} are the shear moduli for the orthotropic material (there are three mutually perpendicular planes of elastic symmetry). On the other side, the isotropic case shows that the material properties are constant across every direction in the space, thus E is the Young's modulus and G is the shear one. In the end, Poisson's ratios are defined through the following relation:

$$\nu_{ij} = -\frac{\varepsilon_{jj}}{\varepsilon_{ii}}, i, j = 1,2,3 \; and \; i \neq j \tag{3.14}$$

Similar considerations lead to the definition of a unique Poisson's ratio for isotropic materials.

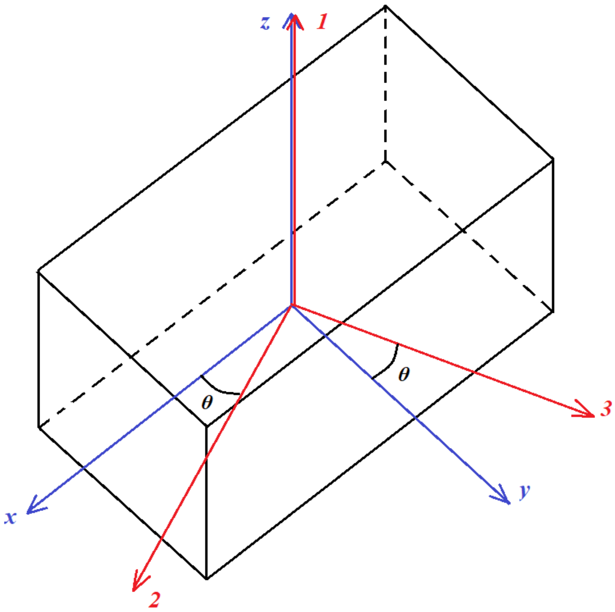

Figure 27: Material and physical coordinates for an orthotropic material.

Figure 27 shows the material reference system for an orthotropic material, where (1, 2, 3) axes are aligned with the planes of elastic symmetry. In general, these directions could be oriented in a different way from structural reference system (x, y, z). Therefore, a transformation from material to physical coordinates is defined, where stresses and strains in physical coordinates are:

$$\begin{aligned} \vec{\sigma} &= \boldsymbol{T}\vec{\sigma}_m \\ \vec{\varepsilon}_m &= \boldsymbol{T^T}\vec{\varepsilon} \end{aligned} \tag{3.15}$$

Where T is the transformation matrix, that has *6x6* dimensions and is function of the rotation angle θ (matrix multiplications necessary to obtain the coefficients in the structural reference system in *Appendix II*):

$$T = \begin{bmatrix} \cos^2(\theta) & sin^2(\theta) & 0 & 0 & 0 & \sin(2\theta) \\ sin^2(\theta) & \cos^2(\theta) & 0 & 0 & 0 & -\sin(2\theta) \\ 0 & 0 & 1 & 0 & 0 & 0 \\ 0 & 0 & 0 & cos\,(\theta) & -\sin(\theta) & 0 \\ 0 & 0 & 0 & \sin(\theta) & cos\,(\theta) & 0 \\ -\sin(\theta)\cos(\theta) & \sin(\theta)\cos(\theta) & 0 & 0 & 0 & \cos^2(\theta) - sin^2(\theta) \end{bmatrix} \tag{3.16}$$

$\widetilde{\boldsymbol{C}}$ is the transformed material stiffness matrix in the physical coordinate system:

$$\vec{\sigma} = \boldsymbol{T}\vec{\sigma}_m = \boldsymbol{T}\boldsymbol{C_m}\vec{\varepsilon}_m = \boldsymbol{T}\boldsymbol{C_m}\boldsymbol{T^T}\vec{\varepsilon} = \widetilde{\boldsymbol{C}}\vec{\varepsilon} \tag{3.17}$$

Moreover, if the stress and strain vectors are split according to equations *3.4* and *3.5*:

$$\begin{cases}\vec{\sigma}_p = \widetilde{\boldsymbol{C}}_{pp}\vec{\varepsilon}_p + \widetilde{\boldsymbol{C}}_{pn}\vec{\varepsilon}_n \\ \vec{\sigma}_n = \widetilde{\boldsymbol{C}}_{np}\vec{\varepsilon}_p + \widetilde{\boldsymbol{C}}_{nn}\vec{\varepsilon}_n\end{cases} \tag{3.18}$$

The sub-matrices composing $\widetilde{\boldsymbol{C}}$ are defined as follows:

$$\widetilde{\boldsymbol{C}}_{pp} = \begin{bmatrix}\tilde{C}_{11} & \tilde{C}_{12} & 0 \\ \tilde{C}_{12} & \tilde{C}_{22} & 0 \\ 0 & 0 & \tilde{C}_{44}\end{bmatrix};\widetilde{\boldsymbol{C}}_{pn} = \widetilde{\boldsymbol{C}}_{np}{}^{T} = \begin{bmatrix}0 & \tilde{C}_{16} & \tilde{C}_{13} \\ 0 & \tilde{C}_{26} & \tilde{C}_{23} \\ \tilde{C}_{45} & 0 & 0\end{bmatrix};\widetilde{\boldsymbol{C}}_{nn} = \begin{bmatrix}\tilde{C}_{55} & 0 & 0 \\ 0 & \tilde{C}_{66} & \tilde{C}_{36} \\ 0 & \tilde{C}_{36} & \tilde{C}_{33}\end{bmatrix} \tag{3.19}$$

The same conditions of equation *3.19* are applied to isotropic materials, with some further simplifications since there are only three independent coefficients.

All the basic material and geometrical properties have been defined, as well as constitutive equations. The next step necessary to obtain a modal analysis of wing structure is to define the simplified model that will be used to represent its stiffness and deformation.

3.2 Beam modeling through Carrera unified formulation

Displacements of beam structure points can be expressed with the following compact expression (*3.20*), which is composed by two terms:

1. $F_\tau(x,z)$, describes the cross-section deformation.
2. $\overrightarrow{u_\tau}(y,t)$, describes the displacement of each section depending on time and *y* coordinate.

$$\begin{gathered}\vec{u}(x,y,z,t) = F_\tau(x,z)\overrightarrow{u_\tau}(y,t) \\ \tau = 1,\dots,N_u\end{gathered} \tag{3.20}$$

This compact expression uses Einstein's notation, with summation respect to subscript τ, that is the arbitrary expansion order of the 1D displacement *Carrera Unified Formulation* (*CUF*) model. The class of the model is determined by the order of approximation adopted for the cross-section deformation. In sub-chapters *3.2.1* and *3.2.2* the orders of approximation adopted in this work will be described. The necessities determined by a good representation of bending and torsion of a beam structure, according to *Petrolo M. [13] (p. 94)*, are related to the discretization that is chosen: in this work, as a compromise between the solution time and the accuracy of the result, *3-rd* and *4-th* order McLaurin polynomials will be used for the cross-section deformation and *4-th* order Lagrange polynomials will be used for the element wise nodes discretization.

3.2.1 McLaurin polynomials

As stated by *Carrera E. [12] (pp. 300-304)*, the cross-section behaviour can be approximated with a method inspired by the classical models, but with a higher order approximation. As an example, the first order complete beam model (*Carrera E. [12], p. 295*) is presented in equation *3.21*:

$$\begin{cases}u = u_1 + xu_2 + zu_3 \\ v = v_1 + xv_2 + zv_3 \\ w = w_1 + xw_2 + zw_3\end{cases} \tag{3.21}$$

With 3 constant variables (u_1, v_1, w_1) and 6 linear ones $(u_2, u_3, v_2, v_3, w_2, w_3)$.

The use of fourth order polynomials brings to a quartic approximation across the section of the beam, which is explained in equation *3.22* with the compact representation (CUF and Einstein's notation) and the explicit one (*3.23*):

$$\vec{u}(x,y,z,t) = F_\tau(x,z)\overrightarrow{u_\tau}(y,t), \qquad \tau = 1, \dots, \frac{(N+1)(N+2)}{2} = N_u, \qquad N = 4$$
$$F_\tau(x,z) = x^i z^j, \qquad i,j = 0, \dots, N \tag{3.22}$$

$$\begin{cases} u_x = u_{x1} + xu_{x2} + zu_{x3} + x^2u_{x4} + xzu_{x5} + z^2u_{x6} + x^3u_{x7} + x^2zu_{x8} + xz^2u_{x9} \\ \qquad +z^3u_{x10} + x^4u_{x11} + x^3zu_{x12} + x^2z^2u_{x13} + xz^3u_{x14} + z^4u_{x15} \\ u_y = u_{y1} + xu_{y2} + zu_{y3} + x^2u_{y4} + xzu_{y5} + z^2u_{y6} + x^3u_{y7} + x^2zu_{y8} + xz^2u_{y9} \\ \qquad +z^3u_{y10} + x^4u_{y11} + x^3zu_{y12} + x^2z^2u_{y13} + xz^3u_{y14} + z^4u_{y15} \\ u_z = u_{z1} + xu_{z2} + zu_{z3} + x^2u_{z4} + xzu_{z5} + z^2u_{z6} + x^3u_{z7} + x^2zu_{z8} + xz^2u_{z9} \\ \qquad +z^3u_{z10} + x^4u_{z11} + x^3zu_{z12} + x^2z^2u_{z13} + xz^3u_{z14} + z^4u_{z15} \end{cases} \tag{3.23}$$

The deformation is thus dependent on 15 coefficients for each direction: *Figure 28* represents the shape of the McLaurin (or Taylor) polynomials used in this work.

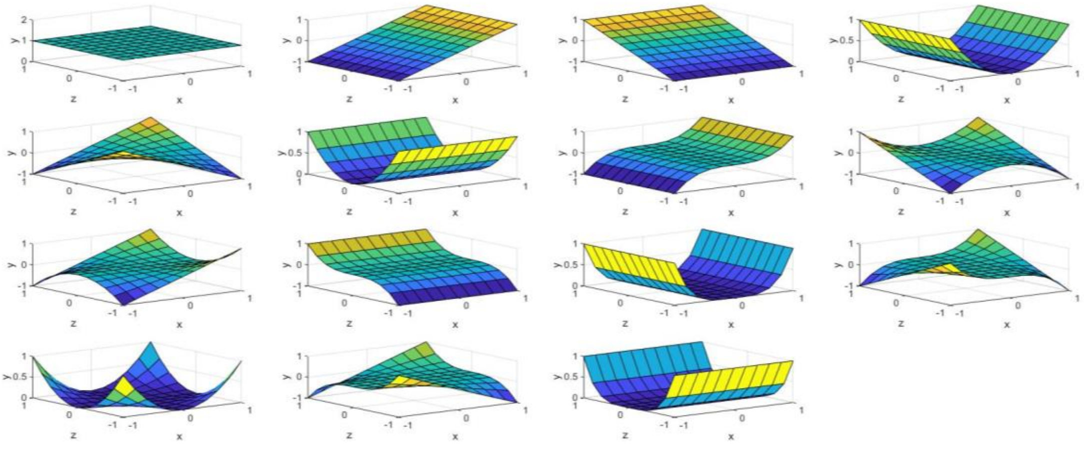

Figure 28: McLaurin polynomials for N=4. From left to right and from to bottom the polynomials are: 1, x, z, x^2, xz, z^2, x^3, x^2z, xz^2, z^3, x^4, x^3z, x^2z^2, xz^3, z^4.

3.2.2 Isoparametric Finite Elements

Following the finite elements method (FEM), the beam is divided into a certain number of elements along *y* coordinate of the reference system presented before. Each element has a certain length, does not overlap with the previous and the following ones, and the mathematical governing equations for the structural problem are solved through a numerical approximated approach (that will be explained briefly in the next section). Isoparametric 1D finite elements are here considered to approximate the displacement field along the *y* direction (*Varello A. [14], p. 31-36*): displacements of any point along the beam longitudinal coordinate are obtained through an interpolation of the displacements of nodal points through shape functions or interpolation functions. Moreover:

1. Each element is defined through equally spaced nodes.
2. The length of the element is L_{el} and is equal to the distance from node 1 to node 2.
3. The internal nodes are ordered from left to right (*Figure 29*).
4. Lagrange polynomials are the ones that satisfy the conditions imposed for shape functions.

This approach can be generalized to an arbitrary number of nodes greater than two for each element. *Figure 29* shows the natural coordinate system for a generic third order element, where y_1 and y_2 are its extremities:

$$r = \frac{(y - y_1) + (y - y_2)}{(y_2 - y_1)} \tag{3.24}$$

The equations that define the general shape functions and the reference system used for each element are presented in the following lines:

$$N_i(r) = \prod_{\gamma=1,\gamma\neq 1}^{N_N} \frac{(r - r_\gamma)}{(r_i - r_\gamma)} \tag{3.25}$$

Where N_N is the number of nodes (in this case $N_N=4$) and Ni represents Lagrange polynomials of the $(N_N\text{-}1)$ order in the natural coordinate system (the value of Ni is always zero for the *i-th* node).

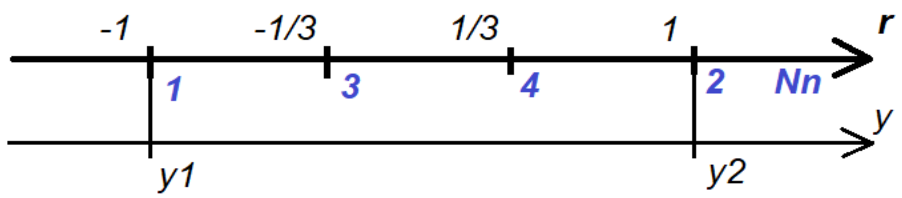

Figure 29: Natural coordinate system for a 4-node finite element.

The explicit formulation of shape functions for the 4-node element can be found in equation *3.26*, they are also graphically represented in *Figure 30*, in the natural coordinate system:

$$\begin{aligned}
N_1 &= -\frac{9}{16}\left(r+\frac{1}{3}\right)\left(r-\frac{1}{3}\right)(r-1) = -\frac{9}{16}r^3 + \frac{9}{16}r^2 + \frac{1}{16}r - \frac{1}{16} \\
N_2 &= +\frac{9}{16}(r+1)\left(r+\frac{1}{3}\right)\left(r-\frac{1}{3}\right) = +\frac{9}{16}r^3 + \frac{9}{16}r^2 - \frac{1}{16}r - \frac{1}{16} \\
N_3 &= +\frac{27}{16}(r+1)\left(r-\frac{1}{3}\right)(r-1) = +\frac{27}{16}r^3 - \frac{9}{16}r^2 - \frac{27}{16}r + \frac{9}{16} \\
N_4 &= -\frac{27}{16}(r+1)\left(r+\frac{1}{3}\right)(r-1) = -\frac{27}{16}r^3 - \frac{9}{16}r^2 + \frac{27}{16}r + \frac{9}{16}
\end{aligned} \tag{3.26}$$

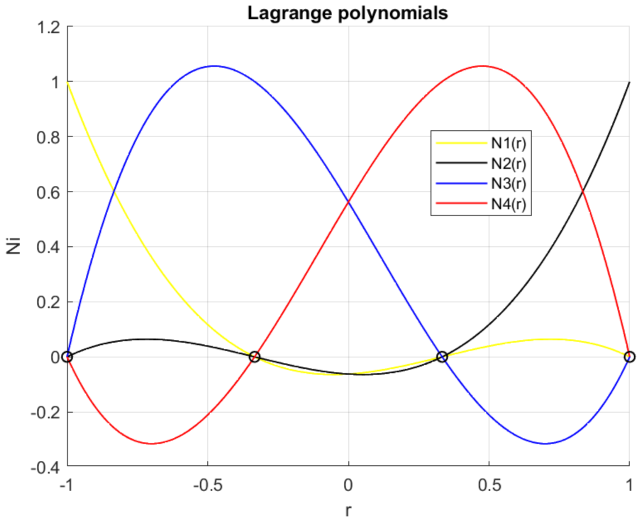

Figure 30: Third order Lagrange polynomials in the natural coordinate system.

3.3 1D Finite Elements model

From the previous section (*3.2*) considerations, it is possible to define the displacement of each point in three-dimensional space that belongs to the beam element. This procedure is carried out considering shape functions in the beam reference system (and not the natural coordinate one), thus a variable change is introduced from equation *3.24*:

$$r = \frac{(y - y_1) + (y - y_2)}{(y_2 - y_1)} = \frac{2(y - y_1) - L_{el}}{L_{el}} \tag{3.27}$$

The displacement field can be finally presented in the following formulation:

$$\vec{u}(x, y, z, t) = F_\tau(x, z) N_i(y) \overrightarrow{q_{\tau i}}(t),$$
$$\tau = 1, \dots, \frac{(N+1)(N+2)}{2}, \qquad i = 1, \dots, N_N \tag{3.28}$$

Where $\overrightarrow{q_{\tau i}}(t)$ is the vector containing all nodal displacements in the 3D space and its dimensions are:

- $3N_N \times N_u$, for a single element. It is obvious that the vector length depends directly on the order of approximation chosen.
- $3[(N_N - 1)N_{EL} + 1] \times N_u$, for the whole beam structure. Square brackets identify the global number of nodes of the beam, considering that in the case of a cantilever structure each element has in common one node with the previous and with the following finite element.

Table 12 resumes the number of degrees of freedom (DOFs) for a beam structure composed of 10 elements of different orders:

10 Beam elements, no boundary conditions applied		***Cross section approximation order***			
		First, $N_u = 3$	*Second, $N_u = 6$*	*Third, $N_u = 10$*	*Fourth, $N_u = 15$*
Element Nodes	*2*	33	198	330	495
	3	63	378	630	945
	4	93	558	930	1395

Table 12: Number of DOFs for a 10 elements beam.

As can be observed in the previous lines, the cantilever beam considered is free to move in space, thus it is fleeting in 3D space and no deformations are experienced due to the applied forces. In the following chapters, the applied boundary condition will be specified with reference to the nodal degrees of freedom.

3.4 Principle of Virtual displacements and solution of the problem

The solution of the elastic problem is obtained through the Principle of Virtual Work (PVW), that according to *Carrera E. [12] (p.119)* can be considered as the universal instrument to solve structural problems. The general statement is that the virtual variation of total work done by an equilibrate system of forces and tensions on a system "a" acting on a system "b" of congruent displacements and deformations is equal to zero.

$$\delta L^{ab} = 0 \tag{3.29}$$

The system "a" is the configuration in which internal and external forces acting on the body are in equilibrium, while displacements and deformations are due to the forces considered. The system "b" is the one where all displacements and deformations are congruent, and the forces and tensions are dependent on the deformations.

It can be rewritten in the simple shape presented in equation *3.30*, because of the equilibrium between internal and external forces acting on the structure. This formulation is also called Principle of Virtual Displacements (PVD): forces are real, while displacements are virtual variations.

$$\delta L_{int} = \delta L_{ext} \tag{3.30}$$

The definitions of the two terms of the equation are:

$$\begin{gathered} \delta L_{ext} = \delta L_P + \delta L_l + \delta L_S + \delta L_V - \delta L_{ine} \\ \delta L_{int} = \int_V \left(\sigma_{xx}\delta\varepsilon_{xx} + \sigma_{yy}\delta\varepsilon_{yy} + \sigma_{zz}\delta\varepsilon_{zz} + \sigma_{xy}\delta\gamma_{xy} + \sigma_{xz}\delta\gamma_{xz} + \sigma_{yz}\delta\gamma_{yz}\right) dV \end{gathered} \tag{3.31}$$

Where σ, ε are stresses and displacements, while L_P is the external work done by point loads, L_l the one due to line loads, L_S the one carried out by surface forces and L_V the one by volume loads. Also, the work done by inertial loads (L_{ine}) is considered in the external contribute.

The present equations are referred to a single element with the y axis aligned with the global one. The effect of the rotation of elements in the global coordinate system and the assembly procedure will be discussed later. Thanks to the previous relations introduced in equation *3.8*, the internal work expression becomes:

$$\delta L_{int} = \int_V \left(\delta\overrightarrow{\varepsilon_n}^T \overrightarrow{\sigma_n} + \delta\overrightarrow{\varepsilon_p}^T \overrightarrow{\sigma_p}\right) dV = \int_l \int_\Omega \left(\delta\overrightarrow{\varepsilon_n}^T \overrightarrow{\sigma_n} + \delta\overrightarrow{\varepsilon_p}^T \overrightarrow{\sigma_p}\right) d\Omega dy \tag{3.32}$$

$$\begin{gathered} \delta\overrightarrow{\varepsilon_n} = \left(\boldsymbol{D}_{np} F_\tau \boldsymbol{I}\right) N_i \delta\overrightarrow{q_{\tau i}} + F_\tau\left(\boldsymbol{D}_{ny} N_i \boldsymbol{I}\right) \delta\overrightarrow{q_{\tau i}} \\ \delta\overrightarrow{\varepsilon_p} = \left(\boldsymbol{D}_p F_\tau \boldsymbol{I}\right) N_i \delta\overrightarrow{q_{\tau i}} \end{gathered} \tag{3.33}$$

Where the volume integral can be split in the cross section contribute and in the y coordinate one. Moreover, the beam elements considered in this Finite Element approach have a constant cross section.

Before proceeding to the substitution in equation *3.32*, the transposed components of the three terms in *3.33* are evaluated:

$$
\begin{aligned}
\left[\left(\boldsymbol{D}_{np}F_\tau\boldsymbol{I}\right)N_i\delta\overrightarrow{q_{\tau i}}\right]^T &= \delta\overrightarrow{q_{\tau i}}^T N_i\left(\boldsymbol{D}_{np}{}^T F_\tau\boldsymbol{I}\right)\\
\left[F_\tau\left(\boldsymbol{D}_{ny}N_i\boldsymbol{I}\right)\delta\overrightarrow{q_{\tau i}}\right]^T &= \delta\overrightarrow{q_{\tau i}}^T\left(\boldsymbol{D}_{ny}{}^T N_i\boldsymbol{I}\right)F_\tau\\
\left[\left(\boldsymbol{D}_{p}F_\tau\boldsymbol{I}\right)N_i\delta\overrightarrow{q_{\tau i}}\right]^T &= \delta\overrightarrow{q_{\tau i}}^T N_i\left(\boldsymbol{D}_{p}{}^T F_\tau\boldsymbol{I}\right)
\end{aligned}
\tag{3.34}
$$

Following the procedure provided by *Varello A. (pp. 43-44) [14],* that refers to the formulation of internal work expression for a 1D Finite Elements method in *Carrera Unified Formulation*, the result obtained is:

$$\delta L_{int} = \delta\overrightarrow{q_{\tau i}}^T \boldsymbol{K}^{\tau sij}\overrightarrow{q_{sj}} \tag{3.35}$$

Where $\overrightarrow{q_{sj}}$ is the nodal displacement vector, while $\delta\overrightarrow{q_{\tau i}}^T$ is the transposed virtual displacements vector. $\boldsymbol{K}^{\tau sij}$ is the fundamental nucleus of the structural stiffness matrix of this model and is a *3x3* matrix, whose terms are obtained through equation *3.35*. It is important to underline that at this point no hypotheses have been made on material properties.

$$
\begin{aligned}
\boldsymbol{K}^{\tau sij} = &\int_l N_iN_j dy\int_\Omega \Big\{\left(\boldsymbol{D}_{np}{}^T F_\tau\boldsymbol{I}\right)\left[\widetilde{\boldsymbol{C}}_{np}\left(\boldsymbol{D}_p F_s\boldsymbol{I}\right)+\widetilde{\boldsymbol{C}}_{nn}\left(\boldsymbol{D}_{np}F_s\boldsymbol{I}\right)\right]\\
&+\left(\boldsymbol{D}_p{}^T F_\tau\boldsymbol{I}\right)\left[\widetilde{\boldsymbol{C}}_{pp}\left(\boldsymbol{D}_p F_s\boldsymbol{I}\right)+\widetilde{\boldsymbol{C}}_{pn}\left(\boldsymbol{D}_{np}F_s\boldsymbol{I}\right)\right]\Big\}\,d\Omega\\
&+\int_l N_iN_{j,y}dy\int_\Omega\left[\left(\boldsymbol{D}_{np}{}^T F_\tau\boldsymbol{I}\right)\widetilde{\boldsymbol{C}}_{nn}+\left(\boldsymbol{D}_p{}^T F_\tau\boldsymbol{I}\right)\widetilde{\boldsymbol{C}}_{pn}\right]F_s d\Omega\boldsymbol{I}_{\Omega y}\\
&+\int_l N_{i,y}N_j dy\,\boldsymbol{I}_{\Omega y}{}^{\boldsymbol{T}}\int_\Omega\left[\widetilde{\boldsymbol{C}}_{np}\left(\boldsymbol{D}_p F_s\boldsymbol{I}\right)+\widetilde{\boldsymbol{C}}_{nn}\left(\boldsymbol{D}_{np}F_s\boldsymbol{I}\right)\right]d\Omega\\
&+\int_l N_{i,y}N_{j,y}dy\,\boldsymbol{I}_{\Omega y}{}^{\boldsymbol{T}}\int_\Omega F_\tau\widetilde{\boldsymbol{C}}_{nn}F_s d\Omega\,\boldsymbol{I}_{\Omega y}
\end{aligned}
\tag{3.36}
$$

The remaining terms that must be evaluated are those related to the inertial work, since the modal analysis (or free vibrational analysis) is affected by the stiffness and inertial properties of the structure. The virtual variation of the work of inertial loadings term is expressed as:

$$\delta L_{ine} = \int_V \delta\,\boldsymbol{u}^T\rho\ddot{\boldsymbol{u}}dV = \int_l\int_\Omega \delta\,\boldsymbol{u}^T\rho\ddot{\boldsymbol{u}}d\Omega dy \tag{3.37}$$

Where the acceleration vector ($\ddot{\boldsymbol{u}}$) and the density of the material (ρ) are introduced. The integrations across the volume of the beam are carried out with the same hypothesis of the internal work. The virtual displacements and the acceleration vector are thus (remember that the following notations are equivalent and are referred to the displacements and nodal displacements vectors: $\boldsymbol{u}=\vec{u}$, $\boldsymbol{q}=\vec{q}$):

$$
\begin{aligned}
\delta\boldsymbol{u} &= F_\tau N_i\delta\boldsymbol{q}_{\boldsymbol{\tau i}}\\
\ddot{\boldsymbol{u}} &= F_\tau N_i\ddot{\boldsymbol{q}}_{\boldsymbol{\tau i}}
\end{aligned}
\tag{3.38}
$$

The substitution in equation *3.38* brings to the following formulation:

$$\begin{aligned}\delta L_{ine} &= \delta \boldsymbol{q_{\tau i}}^T \left\{ \int_l N_i \left[\int_\Omega \rho F_\tau F_s d\Omega \, \boldsymbol{I} \right] N_i dy \right\} \ddot{\boldsymbol{q}}_{\boldsymbol{sJ}} \\ \delta L_{ine} &= \delta \boldsymbol{q_{\tau i}}^T \left\{ \int_l N_i N_j dy \int_\Omega \rho F_\tau F_s d\Omega \, \boldsymbol{I} \right\} \ddot{\boldsymbol{q}}_{\boldsymbol{sJ}} \\ \delta L_{ine} &= \delta \boldsymbol{q_{\tau i}}^T \boldsymbol{M}^{\tau sij} \ddot{\boldsymbol{q}}_{\boldsymbol{sJ}}\end{aligned} \tag{3.39}$$

Where $\boldsymbol{M}^{\tau sij}$ is the fundamental nucleus of the mass matrix of the considered model. It is a *3x3* matrix that represents the inertial properties of the considered structure.

To complete this presentation, it is important to observe that subscripts *s* and *j* are referred to the real displacements and forces, while τ and *i* are the virtual ones. As stated before, the work of applied loads is evaluated only for point loads, because the applied forces are the aerodynamic ones, concentrated on *Load Points* for each panel.

$$\delta L_P = \delta \boldsymbol{u}^T \boldsymbol{P} = \delta \boldsymbol{q_{\tau i}}^T N_i F_\tau \boldsymbol{P} = \delta \boldsymbol{q_{\tau i}}^T \boldsymbol{F}_{\tau i}{}^P \tag{3.40}$$

Equation *3.40* presents the fundamental nucleus of the vector of nodal forces, equivalent to the point loads (the nucleus dimensions are *3x1*).

3.5 Static Deformation Problem

The static analysis problem is solved considering the Principle of Virtual Displacements (PVD) in the simplified formulation written in equation *3.41*:

$$\begin{gathered}\delta L_{int} = \delta L_{loads} - \delta L_{ine} \\ with: \delta L_{ine} = 0 \\ \boldsymbol{K}^{\tau sij} \overrightarrow{q_{sJ}} = \boldsymbol{F}_{\tau i}\end{gathered} \tag{3.41}$$

Where the expansion indices depend on the nodes and the expansion order chosen for the cross-section:

$$\begin{gathered}s = 1, \dots, N_u \\ \forall \tau = 1, \dots, N_u \\ \\ j = 1, \dots, [(N_N - 1)N_{EL} + 1] \\ \forall i = 1, \dots, [(N_N - 1)N_{EL} + 1]\end{gathered} \tag{3.42}$$

The equation is obtained neglecting the inertial work term from the PVD, where the general formulation is:

$$\boldsymbol{K}\vec{q} = \boldsymbol{F} \tag{3.43}$$

3.6 Free Vibration Problem

The results obtained in *chapter 3.4* can be used to rephrase of Principle of Virtual Displacements to obtain the governing equations for the free vibration problem.

$$\delta L_{int} = \delta L_{loads} - \delta L_{ine}$$

$$with: \delta L_{loads} = 0$$

$$\delta \boldsymbol{q_{\tau i}}^T \boldsymbol{M}^{\tau sij} \ddot{\boldsymbol{q_{sj}}} = \delta \boldsymbol{q_{\tau i}}^T \boldsymbol{F}_{\tau i}{}^P - \delta \boldsymbol{q_{\tau i}}^T \boldsymbol{K}^{\tau sij} \boldsymbol{q_{sj}} \tag{3.44}$$

$$\delta \boldsymbol{q_{\tau i}}^T \boldsymbol{M}^{\tau sij} \ddot{\boldsymbol{q_{sj}}} + \delta \boldsymbol{q_{\tau i}}^T \boldsymbol{K}^{\tau sij} \boldsymbol{q_{sj}} = \delta \boldsymbol{q_{\tau i}}^T \boldsymbol{F}_{\tau i}{}^P$$

Where:

$$\begin{gathered} s = 1, \dots, N_u \\ \forall \tau = 1, \dots, N_u \\ \\ j = 1, \dots, [(N_N - 1)N_{EL} + 1] \\ \forall i = 1, \dots, [(N_N - 1)N_{EL} + 1] \end{gathered} \tag{3.45}$$

Equation *3.45* states that the governing equation is referred to the whole structure, since the indices *i* and *j* vary from 1 to the last element of the beam structure, as seen in the examples of *Table 10*. The virtual displacements in *3.44* can be simplified and the obtained result is:

$$\begin{gathered} \boldsymbol{M}^{\tau sij} \ddot{\boldsymbol{q_{sj}}} + \boldsymbol{K}^{\tau sij} \boldsymbol{q}_{sj} = \boldsymbol{F}_{\tau i}{}^P \\ \\ s = 1, \dots, N_u \\ j = 1, \dots, [(N_N - 1)N_{EL} + 1] \\ \\ \forall \tau = 1, \dots, N_u \\ \forall i = 1, \dots, [(N_N - 1)N_{EL} + 1] \end{gathered} \tag{3.46}$$

This brings to the general formulation of the elasticity problem where the vector $\boldsymbol{q}$ is the nodal displacement vector for each degree of freedom of the structure and $\boldsymbol{K}$, $\boldsymbol{M}$, and $\boldsymbol{F}$ are the structural stiffness matrix, mass matrix and equivalent nodal forces vector respectively.

$$\boldsymbol{M}\ddot{\boldsymbol{q}} + \boldsymbol{K}\boldsymbol{q} = \boldsymbol{F} \tag{3.47}$$

The free vibrational analysis is obtained from *3.47* neglecting the work of loadings:

$$\boldsymbol{M}\ddot{\boldsymbol{q}} + \boldsymbol{K}\boldsymbol{q} = 0 \tag{3.48}$$

The eigenvalue problem is solved to obtain the frequencies and eigenvectors of the problem:

$$[-{\omega_h}^2 \boldsymbol{M} + \boldsymbol{K}]\boldsymbol{q_h} = 0 \tag{3.49}$$

3.7 Structural stiffness and mass matrices

The final step necessary to solve the structural modal analysis problem is to build the structural stiffness and mass matrices for the considered material and cross section. The present work will consider a simplified condition since the materials used will be isotropic or orthotropic: this condition is coherent with the use of carbon fibre, glass fibre and their main properties.

If the material is homogeneous over the cross section of the considered beam structure, the fundamental nucleus of the stiffness matrix is evaluated through *3.36* with some simplifications: the coefficients for the orthotropic material stiffness matrix are constant over the section (the expressions are evaluated following *Carrera E., Cinefra M. [12] pp. 295*-300 and *Varello A. [14] pp. 59-60*).

$$
\begin{aligned}
K_{xx}^{\tau sij} &= \tilde{C}_{22}E_j^iJ_{s,x}^{\tau,x} + \tilde{C}_{44}E_j^iJ_{s,z}^{\tau,z} + \tilde{C}_{26}E_{j,y}^iJ_s^{\tau,x} + \tilde{C}_{26}E_j^{i,y}J_{s,x}^{\tau} + \tilde{C}_{66}E_{j,y}^{i,y}J_s^{\tau}\\
K_{xy}^{\tau sij} &= \tilde{C}_{23}E_j^iJ_{s,x}^{\tau,x} + \tilde{C}_{45}E_j^iJ_{s,z}^{\tau,z} + \tilde{C}_{26}E_j^iJ_{s,x}^{\tau,x} + \tilde{C}_{36}E_{j,y}^{i,y}J_s^{\tau} + \tilde{C}_{66}E_j^{i,y}J_{s,x}^{\tau}\\
K_{xz}^{\tau sij} &= \tilde{C}_{12}E_j^iJ_{s,z}^{\tau,x} + \tilde{C}_{44}E_j^iJ_{s,x}^{\tau,z} + \tilde{C}_{45}E_{j,y}^iJ_s^{\tau,z} + \tilde{C}_{16}E_j^{i,y}J_{s,z}^{\tau}\\
K_{yx}^{\tau sij} &= \tilde{C}_{23}E_j^{i,y}J_{s,x}^{\tau} + \tilde{C}_{45}E_j^iJ_{s,z}^{\tau,z} + \tilde{C}_{26}E_j^iJ_{s,x}^{\tau,x} + \tilde{C}_{36}E_{j,y}^{i,y}J_s^{\tau} + \tilde{C}_{66}E_{j,y}^iJ_s^{\tau,x}\\
K_{yy}^{\tau sij} &= \tilde{C}_{33}E_{j,y}^{i,y}J_s^{\tau} + \tilde{C}_{55}E_j^iJ_{s,z}^{\tau,z} + \tilde{C}_{36}E_{j,y}^iJ_s^{\tau,x} + \tilde{C}_{36}E_j^{i,y}J_{s,x}^{\tau} + \tilde{C}_{66}E_j^iJ_{s,x}^{\tau,x}\\
K_{yz}^{\tau sij} &= \tilde{C}_{13}E_j^{i,y}J_{s,z}^{\tau} + \tilde{C}_{55}E_{j,y}^iJ_s^{\tau,z} + \tilde{C}_{45}E_j^iJ_{s,z}^{\tau,z} + \tilde{C}_{16}E_j^iJ_{s,z}^{\tau,x}\\
K_{zx}^{\tau sij} &= \tilde{C}_{12}E_j^iJ_{s,x}^{\tau,z} + \tilde{C}_{44}E_j^iJ_{s,z}^{\tau,x} + \tilde{C}_{45}E_j^{i,y}J_{s,z}^{\tau} + \tilde{C}_{16}E_{j,y}^iJ_s^{\tau,z}\\
K_{zy}^{\tau sij} &= \tilde{C}_{13}E_{j,y}^iJ_s^{\tau,z} + \tilde{C}_{55}E_j^{i,y}J_{s,z}^{\tau} + \tilde{C}_{45}E_j^iJ_{s,z}^{\tau,x} + \tilde{C}_{16}E_j^iJ_{s,x}^{\tau,z}\\
K_{zz}^{\tau sij} &= \tilde{C}_{11}E_j^iJ_{s,z}^{\tau,z} + \tilde{C}_{44}E_j^iJ_{s,x}^{\tau,x} + \tilde{C}_{55}E_{j,y}^{i,y}J_s^{\tau} + \tilde{C}_{45}E_{j,y}^iJ_s^{\tau,x} + \tilde{C}_{45}E_j^{i,y}J_{s,x}^{\tau}
\end{aligned}
\tag{3.50}
$$

Where the expressions of the integrals over the cross section and along the beam element *y* axis are represented with the present notation:

$$
\begin{aligned}
J_s^{\tau} &= \int_{\Omega} F_\tau F_s d\Omega & J_{s,z}^{\tau,x} &= \int_{\Omega} F_{\tau,x}F_{s,z}d\Omega & E_j^i &= \int_l N_iN_jdy\\
J_s^{\tau,z} &= \int_{\Omega} F_{\tau,z}F_s d\Omega & J_{s,x}^{\tau,z} &= \int_{\Omega} F_{\tau,z}F_{s,x}d\Omega & E_j^{i,y} &= \int_l N_{i,y}N_jdy\\
J_s^{\tau,x} &= \int_{\Omega} F_{\tau,x}F_s d\Omega & J_{s,x}^{\tau,x} &= \int_{\Omega} F_{\tau,x}F_{s,x}d\Omega & E_{j,y}^i &= \int_l N_iN_{j,y}dy\\
J_{s,z}^{\tau} &= \int_{\Omega} F_\tau F_{s,z} d\Omega & J_{s,z}^{\tau,z} &= \int_{\Omega} F_{\tau,z}F_{s,z}d\Omega & E_{j,y}^{i,y} &= \int_l N_{i,y}N_{j,y}dy\\
J_{s,x}^{\tau} &= \int_{\Omega} F_\tau F_{s,x} d\Omega
\end{aligned}
\tag{3.51}
$$

The fundamental mass matrix coefficients are obtained in an analogue way, as shown in *3.52*:

$$M_{xx}^{\tau sij} = E_j^i \int_{\Omega} \rho F_\tau F_s d\Omega$$

$$M_{yy}^{\tau sij} = E_j^i \int_{\Omega} \rho F_\tau F_s d\Omega$$

$$M_{zz}^{\tau sij} = E_j^i \int_{\Omega} \rho F_\tau F_s d\Omega$$

$$M_{xy}^{\tau sij} = M_{xz}^{\tau sij} = M_{yx}^{\tau sij} = 0$$

$$M_{yz}^{\tau sij} = M_{zx}^{\tau sij} = M_{zy}^{\tau sij} = 0 \tag{3.52}$$

Fundamental nuclei $\boldsymbol{M}^{\tau sij}$ and $\boldsymbol{K}^{\tau sij}$ are used to build the mass and structural matrices of a beam element with the properties explained in the previous sections of this chapter. In particular, the indices τ and s are expanded to the order of the cross-section polynomials that are adopted, while i and j are related to the number of nodes of the single element (the example of *Figure 31* is referred to *4-th* order McLaurin polynomials and *4-node* elements):

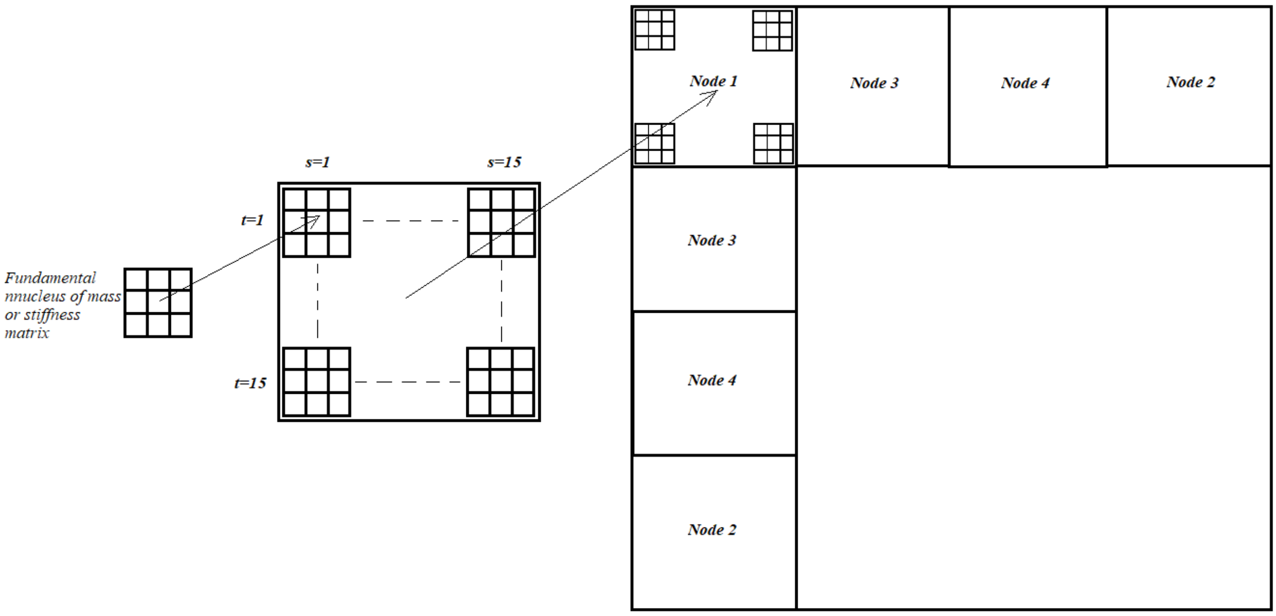

Figure 31: Stiffness and mass matrices building procedure for 4-th order cross section approximation and 4-node elements.

The global stiffness and mass matrices are built considering that the beam is coincident with the y axis of the global reference system, thus no sweep angle is involved, and no rotation of the structural properties is necessary. Moreover, each element shares the first and the last node with the previous and the following one. The result of the assembly is presented in *Figure 32*.

A similar procedure can be used for the equivalent nodal forces vector assembly procedure, where the only difference is related to the fact that the result is a vector with $3[(N_N - 1)N_{EL} + 1] \times N_u$ dimensions.

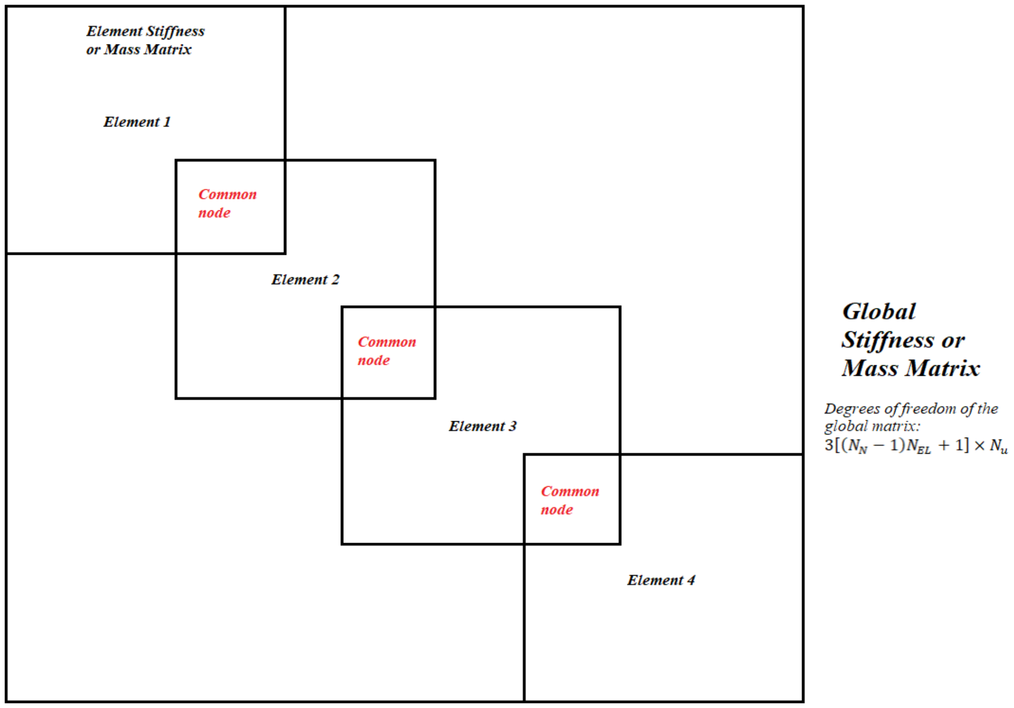

Figure 32: Stiffness and mass matrices building procedure for a 4-node beam structure (4 elements are considered).

3.8 Global coordinate system

The *y* axis of the beams considered in the previous chapters is always parallel to the global one since no sweep angle has been introduced from the structural point of view. In this section, this possibility will be introduced, coherently to the option given in the aerodynamic code (where sweep angle can be arbitrarily defined by the user in the input phase).

In the local coordinate system, the beam *y* axis is perpendicular to *x-z* plane (in which the cross-section is located), while the introduction of a global coordinate system permits the rotation of the local system with three angular degrees of freedom. In this way, the local *y* axis is no more perpendicular to the airspeed direction. The transformation presented in the following lines is general and permits all three rotations, but the considered problem will consider only the presence of sweep angle (dihedral angle and the rotation around the beam axis will not be evaluated). The previous displacements evaluated through CUF applied on FE beam model become:

$$\vec{u}_{loc}(x,y,z) = F_\tau(x,z)N_i(y)\overrightarrow{q_{\tau i}}_{,loc} \tag{3.53}$$

Where subscript *loc* refers to the fact that these displacements are in the local reference system. From this expression, each element's properties must be evaluated in the global reference system. This procedure is carried out introducing the transformation from local to global reference system (and the reverse procedure):

$$\begin{cases} i = e_{11}^G \boldsymbol{i^G} + e_{12}^G \boldsymbol{j^G} + e_{13}^G \boldsymbol{k^G} \\ j = e_{21}^G \boldsymbol{i^G} + e_{22}^G \boldsymbol{j^G} + e_{23}^G \boldsymbol{k^G} \\ k = e_{31}^G \boldsymbol{i^G} + e_{32}^G \boldsymbol{j^G} + e_{33}^G \boldsymbol{k^G} \end{cases} \tag{3.54}$$

$$\begin{cases} \boldsymbol{i^G} = \bar{e}_{11}^G i + \bar{e}_{12}^G j + \bar{e}_{13}^G k \\ \boldsymbol{j^G} = \bar{e}_{21}^G i + \bar{e}_{22}^G j + \bar{e}_{23}^G k \\ \boldsymbol{k^G} = \bar{e}_{31}^G i + \bar{e}_{32}^G j + \bar{e}_{33}^G k \end{cases} \tag{3.55}$$

Where $e_{11}^G, e_{12}^G, e_{13}^G$ are the global coordinates (equation *3.54*) of the local unit vector $\boldsymbol{i}$ (in the same way the other components are the global coordinates of the local vectors). In an analogue way $\bar{e}_{11}^G, \bar{e}_{12}^G, \bar{e}_{13}^G$ are the local coordinates of the global unit vector $\boldsymbol{i^G}$. It is important to notice that the three vectors (*i, j, k*) for each reference system correspond respectively to (*x, y, z*) directions.

Using these expressions, the vectors containing the element degrees of freedom can be used to re-formulate the Principle of Virtual Displacements in the global reference system. The vectors $\delta\boldsymbol{q}_{\tau i}$ and $\boldsymbol{q}_{sj}$ are reported in equation *3.56*:

$$\boldsymbol{q}_{sj,loc} = \boldsymbol{e}^G \boldsymbol{q}_{sj} \qquad \delta\boldsymbol{q}_{\tau i,loc} = \boldsymbol{e}^G \delta\boldsymbol{q}_{\tau i}$$
$$\boldsymbol{q}_{sj} = \bar{\boldsymbol{e}}^G \boldsymbol{q}_{sj,loc} \qquad \delta\boldsymbol{q}_{\tau i} = \bar{\boldsymbol{e}}^G \delta\boldsymbol{q}_{\tau i,loc} \tag{3.56}$$

Finally, the element stiffness matrix is re-formulated in the following way before proceeding with the assembly procedure (the global mass matrix is obtained analogously):

$$\delta L_i = \delta\boldsymbol{q}_{\tau i,loc}{}^T \boldsymbol{K}_{loc}^{\tau sij} \boldsymbol{q}_{sj,loc} = \delta\boldsymbol{q}_{\tau i}{}^T \left[\boldsymbol{e}^{G^T} \boldsymbol{K}_{loc}^{\tau sij} \boldsymbol{e}^G\right] \boldsymbol{q}_{sj}$$
$$\boldsymbol{K}^{\tau sij} = \boldsymbol{e}^{G^T} \boldsymbol{K}_{loc}^{\tau sij} \boldsymbol{e}^G \tag{3.57}$$

Where the transformation matrices are demonstrated to be orthogonal (their product is the identity matrix):

$$\boldsymbol{e}^G = \begin{bmatrix} e_{11}^G & e_{12}^G & e_{13}^G \\ e_{21}^G & e_{22}^G & e_{23}^G \\ e_{31}^G & e_{32}^G & e_{33}^G \end{bmatrix} \qquad \bar{\boldsymbol{e}}^G = \begin{bmatrix} \bar{e}_{11}^G & \bar{e}_{12}^G & \bar{e}_{13}^G \\ \bar{e}_{21}^G & \bar{e}_{22}^G & \bar{e}_{23}^G \\ \bar{e}_{31}^G & \bar{e}_{32}^G & \bar{e}_{33}^G \end{bmatrix} \tag{3.58}$$

$$[\bar{\boldsymbol{e}}^G \boldsymbol{e}^G]^T = \boldsymbol{I} \tag{3.59}$$

An example of the reference system transformation is shown in *Figure 33*, in which a positive sweep angle is introduced for the single finite element considered. All the procedure steps presented in this section follow the ones presented by *Varello A. [14]*, even thought that the variables are denominated in a different way.

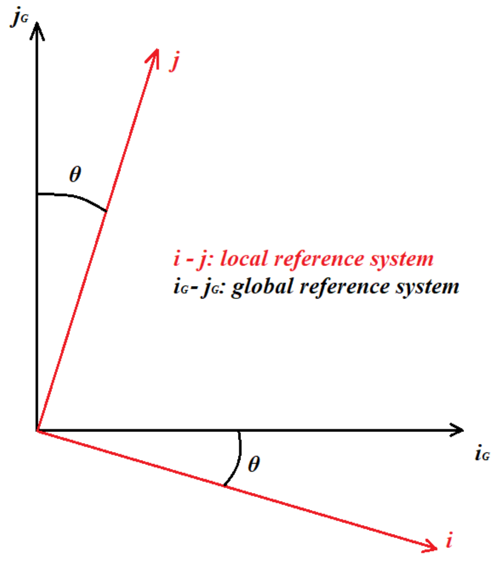

Figure 33: Representation of the local and global coordinate systems relation.

3.9 Structural Code Development and Verification

The previous sections explain the main theory elements necessary to develop a 1D beam Finite Elements Model with *Carrera Unified Formulation*. Although some hypotheses have already been introduced about material properties (orthotropic material…), this chapter will present the main code development steps and will provide a simplified description of the wing structure geometry adopted.

There are two different ways to solve the static deformation and free vibration problem that are suitable for these evaluations (this distinction is made to clarify the aim of the code developed in this work):

1. The model presented in this chapter expects an orthotropic rectangular cross section or a cluster of simple shaped sections for the beam structure. The main disadvantage is that a simplified model must be developed to approximate the real wing. In the Syncro semi-wing case study the structure has already been developed, thus this process is unavoidable.

2. The results necessary for aeroelasticity evaluations are provided by a structural analysis commercial code, where the structural stiffness and mass matrices are an output of the considered code, with a certain number of degrees of freedom.

The first approach will be presented in this work, but this does not exclude any future development following the second strategy described in the previous lines.

3.9.1 Main code development steps

Data input section permits to select the main parameters concerning beam structure characterization, such as:

1. The number of elements that discretize the beam.
2. Global beam length.
3. Rectangular cross section dimensions.
4. The order of McLaurin polynomials that discretize the cross section.
5. The number of natural frequencies to display.

Element material properties definition section, where all the properties concerning each element are assigned:

- E_1, E_2, E_3, that are the elastic moduli of the material in the material reference system.
- G_{21}, G_{31}, G_{23}, the shear moduli of the considered orthotropic material.
- Poisson ratios.

From these values, the elements properties are defined through geometrical relations (*3.1.1*) and constitutive equations (*3.1.2*), as reported in the code developed in this work.

This section has been properly modified to be suitable for Syncro wing model: a subsection where all geometrical properties of the semi-wing are specified is provided. A limitation of this code is determined by the fact that the general shape of the section is defined.

Beam modeling (CUF with Isoparametric elements) section, where the cross-section deformation is defined, and the element-wise nodes are defined for the considered structure. Each element is constituted by four equally spaced nodes (this parameter is fixed), while the cross-section polynomial order can be varied from 1 to 4 by the user.

The inputs necessary to build the stiffness matrix and the material matrix are evaluated through the integrals presented in equation *3.51* using bidimensional integration functions developed by MatLab®. Then, the mass and stiffness matrices reported in equations *3.50* and *3.52* are computed for every fundamental nucleus and assembled according to the procedures described in the previous sections.

The final step of this section is the definition of boundary conditions since the structure of the wing must be linked to the fuselage of the airplane. In this case, the semi-wing will be clamped to a theorical fuselage structure that is not affected by the deformation and forces acting of the wing. For this reason, the displacements of the first node of the first element starting from the fuselage would be zero; in particular, this condition is applied to all the degrees of freedom of the cross-section (the first cross-section is planar and coincident with the $y=0$ plane). The variation of the clamped DOFs of the first section permits to model other fixing systems.

Free vibrational problem resolution section, in which the system presented in equation *3.60* is solved using the functions implemented by MatLab®, that permit to obtain the eigenvalues and the correspondent eigenvectors.

$$[-{\omega_h}^2\boldsymbol{M}+\boldsymbol{K}]\boldsymbol{q_h}=0 \tag{3.60}$$

The frequencies obtained are sorted in ascending order and the number imposed by the user in input section is extracted. Each eigenvector ($\boldsymbol{q_h}$) contains displacement information for the considered mode and can be replaced in *3.61* to obtain the generic displacements for each point of the beam according to the order of approximation used:

$$\begin{gathered}\vec{u}(x,y,z)=F_\tau(x,z)N_i(y)\overrightarrow{q_h},\\ \tau=1,\dots,\frac{(N+1)(N+2)}{2},\qquad i=1,\dots,N_N\end{gathered} \tag{3.61}$$

The solution of the free vibrational system of equations is provided using MatLab® functions that are able to identify sparse matrices, such as the *sparse()* command. This is associated to the function *eigs()*, that solves the eigenvalue problem and finds the first *n* smallest or highest frequencies of the considered equations system.

Static deformation problem resolution section, in which the system presented in equation *3.62* is solved using the functions implemented by MatLab®, that permit to obtain the nodal displacements for the beam.

$$\boldsymbol{Kq}=\boldsymbol{F} \tag{3.62}$$

Displacement's information are replaced in 3*.63* to obtain the generic deformation for each point of the beam according to the order of approximation used:

$$\begin{gathered}\vec{u}(x,y,z)=F_\tau(x,z)N_i(y)\vec{\mathrm{q}},\\ \tau=1,\dots,\frac{(N+1)(N+2)}{2},\qquad i=1,\dots,N_N\end{gathered} \tag{3.63}$$

Post processing section, where beam structure displacements are evaluated on a set of points located over the whole semi-wing for each considered mode and the displacements obtained are saved in a file (*Displacements.mat*). These results are computed through CUF formulation and are plotted in order to visualize the deformation shapes of the beam structure. Moreover, they will be used later to define the displacement conditions for the unsteady aerodynamic problem resolution.

3.9.2 Code verification and convergence considerations

The code presented in this work has been validated through the results given by other structural codes and theorical results in some simple cases, where the beam properties are constant across different elements. This choice is only due to the simplicity of the pre-processing and to the possibility to use theorical results for verification.

The beam selected is characterized by a constant square cross-section and a length of L=*20m*. A different number of elements is selected to underline the effect of this parameter on the results obtained; moreover, the sweep angle is equal to zero (*Figure 34*).

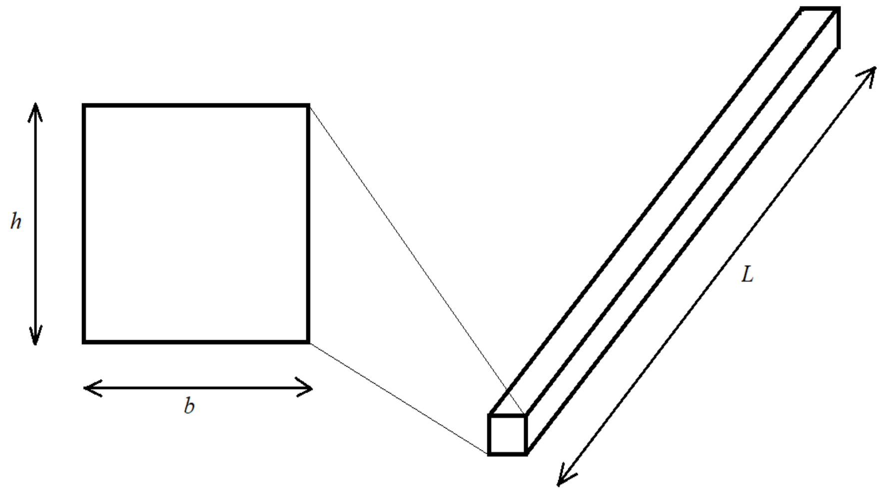

Figure 34: Representation of the beam used for verification process.

Free vibration Frequencies [Hz]									
10 Elements			*20 Elements*			*30 Elements*			*Euler-Bernoulli*
2-nd order	***3-rd order***	***4-th order***	***2-nd order***	***3-rd order***	***4-th order***	***2-nd order***	***3-rd order***	***4-th order***	***Single Element***
0.4280	0.4280	0.4280	0.4268	0.4268	0.4268	0.4264	0.4264	0.4264	0.4257
2.6812	2.6809	2.6809	2.6736	2.6733	2.6733	2.6710	2.6712	2.6710	2.6678
7.5038	7.5024	7.5024	7.4810	7.4797	7.4796	7.4732	7.4745	7.4732	7.4699
14.6983	14.6935	14.6935	14.6457	14.6412	14.6412	14.6282	14.6326	14.6282	14.6379
24.2967	24.2841	24.2841	24.1805	24.1694	24.1694	24.1469	24.1578	24.1468	24.1978

Table 13: Modal Analysis - Results for different orders of cross-section approximation and number beam of elements.

The results are compared to the classical Euler-Bernoulli beam model, where the formula for the natural frequencies of the first five bending modes is (equation *3.64*):

$$f_i = \frac{1}{2\pi}\frac{(\lambda_i L)^2}{L^2}\left(\frac{EI}{\rho A}\right)^{\frac{1}{2}} \tag{3.64}$$

$$\frac{(\lambda_i L)^2}{L^2} = (1.87510, 4.69409, 7.85476, 10.9955, 14.1372)$$

Material and geometrical properties of the considered beam are reported in *3.65*:

$$E = 75 \cdot 10^9\ Pa \qquad \nu = 0.33$$
$$G = 28 \cdot 10^9\ Pa \qquad A = bh = b^2 = 0.2^2 \tag{3.65}$$
$$\rho = 2700 \frac{kg}{m^3} \qquad I = \frac{bh^3}{12} = \frac{b^3h}{12} = \frac{b^4}{12}$$

On the other side, the results of the static deformation problem are presented in *Table 14*, where a single concentrated load along *x* or *z* direction (since the cross-section is square, the results are the same on both directions) is applied at the last node of the beam considered before (*Figure 34*). The order of approximation and the number of beams chosen do not affect the results obtained in each case for the pure bending problem.

Order of McLaurin polynomials	***Number of elements***			
	10 elements	*20 elements*	*30 elements*	*40 elements*
2-nd	264.5 mm	265.6 mm	266.0 mm	266.1 mm
3-rd	264.5 mm	265.6 mm	266.0 mm	266.1 mm
4-th	264.5 mm	265.6 mm	266.0 mm	266.1 mm
δ_{max}	*266.7 mm*			

Table 14: Static deformation - Results for different orders of cross-section approximation and number beam of elements.

Where the results for the static deformation of a uniform cross-section cantilever beam, loaded at its extremity (*P=1000N*) and fixed at the other one, are obtained through:

$$\delta_{max} = \frac{PL^3}{3EI} \tag{3.66}$$

3.9.3 Syncro wing geometry simplification

The semi-wing of Syncro aircraft has been simplified according to the properties of the material and the geometry of wing structure. The final shape has been reduced to an assembly of rectangular shaped cross-sections, on which it is easy to evaluate integrals through the functions implemented in MatLab®. The use of structural results from commercial codes is not considered in this chapters, since the aim of this work is to create a stand-alone solver, able to predict aeroelastic phenomena on a preliminary project phase semi-wing.

3.9.3.1 Composite materials properties

Materials used for Syncro wing model include carbon fibre, glass fibre, PVC foam and resin. The specifications for fibre sheets used by Fly Synthesis s.r.l. are reported in *Table 15*, as well as the ones for resin. Elastic moduli and other properties are obtained for the pure materials and then for the sheets with proper fibres orientation.

Carbon Fibre			
Density	$\boldsymbol{\rho}$	1800	kg/m^3
Sigma	$\boldsymbol{\sigma_R}$	3930	MPa
Elastic Modulus	***E***	231000	MPa
Shear Modulus	***G***	88846,15	MPa
Poisson Coefficient	$\boldsymbol{\nu}$	0,30	-

Glass Fibre			
Density	ρ	2700	kg/m³
Sigma	σ_R	3450	MPa
Elastic Modulus	E	72400	MPa
Shear Modulus	G	30000	MPa
Poisson Coefficient	ν	0,20	-
Resin			
Density	ρ	1200	kg/m³
Sigma	σ_R	70	MPa
Elastic Modulus	E	3000	MPa
Shear Modulus	G	1086,96	MPa
Poisson Coefficient	ν	0,38	-
PVC Foam			
Density	ρ	80	kg/m³
Sigma	σ_R	2,8	MPa
Elastic Modulus	E	100	MPa
Shear Modulus	G	28	MPa
Poisson Coefficient	ν	0,32	-

Table 15: Composite materials specifications.

These values are arranged to evaluate the global material properties for orthotropic orientation of the fibres and certain volume percentages of resin. The main results for 45° specimens are reported in *Table 16*:

Carbon Fibre 160 (C160)			Glass Fibre 80 (V80)		
Layer Thickness	0,16	mm	*Layer Thickness*	0,08	mm
Resin Percentage	0,55	%	*Resin Percentage*	0,55	%
Density	1470	kg/m³	*Density*	1875	kg/m³
Sigma	922,75	MPa	*Sigma*	1591	MPa
Elastic Modulus (L)	105600	MPa	*Elastic Modulus (L)*	34230	MPa
Elastic Modulus (T)	105600	MPa	*Elastic Modulus (T)*	34230	MPa
Shear Modulus	2379,87	MPa	*Shear Modulus*	2313,03	MPa
Poisson Coefficient	0,344	-	*Poisson Coefficient*	0,299	-

Table 16: Laminated composite materials - Fibre sheets global properties.

3.9.3.2 Main structural components and equivalent section properties

The wing structure is composed by different elements with geometrical properties that vary along spanwise direction (y direction in the global coordinate system, since sweep angle is zero for Syncro aircraft). The main elements that can be identified are:

- Two spars since the structure is represented by an anterior and a posterior spar with variable distance along chordwise direction (the rear one is of secondary importance). The main spar is composed by:
    - Upper and lower cap, that have a constant width and a variable height due to the different number of layers that are used (*Table 17* resumes all the properties that are considered).

- Spar web, that is realized in PVC foam and covered by a layer of *C160*. Its cross-section has a constant width along the first part of the wing (*10 mm*), while a discontinuity brings to a reduction to *5 mm* on the outer wing.

- Outer shell panels, characterized by the superposition of two layers of *C160* (inner wing) and a layer of *C160* and one of *V80* (on outer wing). These layers compose the external panels that contribute to the structural torsional stiffness and bending stiffness.

- Other elements, such as connection elements and secondary support elements are not considered in the present model, because of the difficulty of representation with the method used.

The main properties described for the semi-wing are reported in *Table 17*: all data are detected every *50 mm* on the semi-wing structure, while the following schematization will introduce a reduction of the number of elements, that are 21. Moreover, the cross-section shape is shown in *Figure 35*, where it is possible to identify the geometric properties of each section.

y coordinate [mm]	***Element***	***Web distance [mm]***	***Web Width [mm]***	***Web Thickness [mm]***	***Cap Width [mm]***	***Cap Thickness [mm]***
0	1	414,00	10,00	145,00	30,00	13,93
200	2	404,05	10,00	143,20	30,00	12,60
400	3	394,10	10,00	141,40	30,00	11,35
600	4	384,15	10,00	139,60	30,00	10,17
800	5	374,20	10,00	137,80	30,00	9,06
1000	6	364,25	10,00	136,00	30,00	8,02
1200	7	354,30	10,00	134,20	30,00	7,04
1400	8	344,35	5,00	132,40	30,00	6,13
1600	9	334,40	5,00	130,60	30,00	5,28
1800	10	324,45	5,00	128,80	30,00	4,49
2000	11	314,50	5,00	127,00	30,00	3,76
2200	12	304,55	5,00	125,20	30,00	3,09
2400	13	294,60	5,00	123,40	30,00	2,48
2600	14	284,65	5,00	121,60	30,00	1,92
2800	15	274,70	5,00	119,80	30,00	1,46
3000	16	264,75	5,00	118,00	30,00	1,06
3200	17	254,80	5,00	116,20	30,00	0,72
3400	18	244,85	5,00	114,40	30,00	0,44
3600	19	234,90	5,00	112,60	30,00	0,32
3800	20	224,95	5,00	110,80	30,00	0,32
4000	21	215,00	5,00	109,00	30,00	0,16

Table 17: Discrete semi-wing cross section properties for Syncro aircraft.

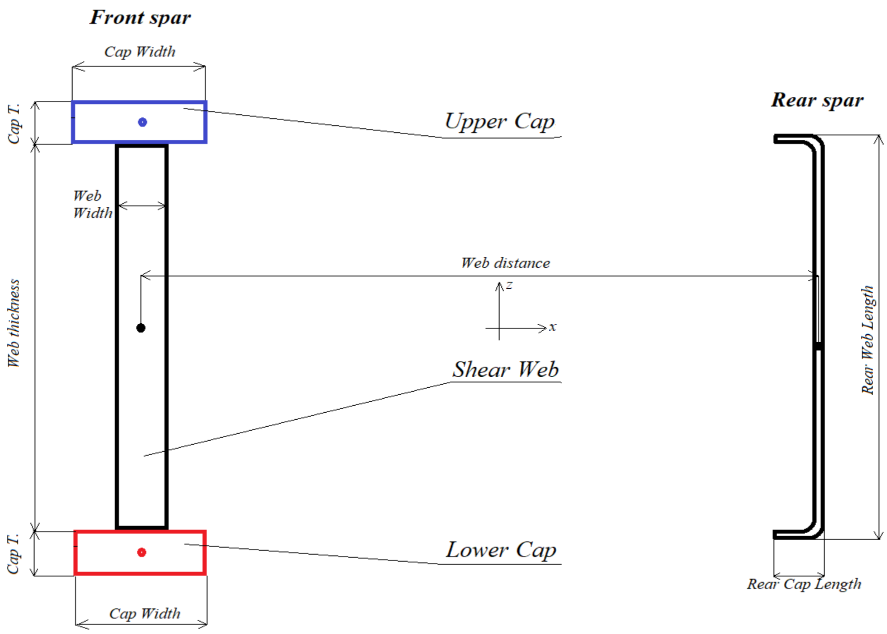

Figure 35: Discrete semi-wing cross section geometry for Syncro aircraft (right semi-wing).

3.9.3.3 Static analysis results

The procedure presented in the previous chapters will be used to evaluate the differences between each cross-section McLaurin polynomial order and the effects of an increasing number of degrees of freedom. *Figure 36* and *Figure 37,* reported in the following pages as a support to static analysis results, represent displacements for each node in the three directions of the coordinate system adopted. On the other side, modal analysis frequencies can be found in *Table 21*.

Switching from a simple cross-section case to the one presented in *Figure 35*, where the focus has been set on the main spar, some further evaluations must be carried out to confirm the validity of the code. The solution provided for the *I* shaped spar underlined convergence issues for both the static and modal analysis. This brings to an ill-conditioned systems of equations, that has been solved with classical MatLab® implemented functions. For the static deformation case:

$$\boldsymbol{K}\vec{q} = \boldsymbol{F} \tag{3.67}$$

- \, that is equivalent to the evaluation of the inverted matrix of the linear problem (*3.67*). It is used in the solution of all classical problems and brought to badly scaled problems for *3-rd* or superior orders McLaurin polynomials (that are the minimum requirements to execute a flutter analysis).

- *ldl(),* which is the function that permits the factorization of *K* matrix in its lower unit diagonal matrix (*L*) and the diagonal matrix (*D*). The equivalent system of equations that is obtained is written in equation *3.68*. This algorithm permits to avoid the divergence of the solution for lower order approximations, but it still diverges as the deformation is evaluated out of the symmetry axis of the beam.

$$\begin{gathered} \boldsymbol{K}\vec{q} = \boldsymbol{F} \\ \boldsymbol{LDL^T}\vec{q} = \boldsymbol{F} \\ \\ where: \boldsymbol{L}\vec{v} = \boldsymbol{F} \\ \boldsymbol{DL^T}\vec{q} = \vec{v} \end{gathered} \tag{3.68}$$

The same problems have been encountered in the modal analysis problem resolution, where the *eig()* function has been exploited to find eigenvalues and eigenvectors for the modal shapes of the considered beam structure.

The analysis of these failures identified two problems in the developed model:

1. The complexity of the cross-section geometry and the entity of geometric variations from the root to the tip of the semi-wing is an unavoidable problem with basic solution tools implemented in MatLab®.

2. A secondary effect can be ascribed to the different material properties of the semi-wing. In particular, the shear web of the spar is realized in PVC with a carbon fibre external cover, that causes a loss in precision as the order of cross-section polynomials grows (only 2-nd order analyses can be executed).

The conclusion is that a *I* shaped spar realized with a single material and without consistent section variations along spanwise coordinate can be represented by the present solver.

The problems underlined in this section determine the need for an alternative representation of Syncro's wing structure. The process that has been followed is based on the development of an equivalent rectangular shaped cross-section that has the same mass properties of the real semi-wing.

3.9.3.4 Pure bending section calibration

Table 18 represents the results obtained from the bending calibration of the Syncro semi-wing model: rectangular cross-section dimensions are obtained from an adaptation on the experimental results.

y coordinate [mm]	***Element***	***Section width [mm]***	***Section height [mm]***
0	1	207,00	73,92
200	2	202,03	72,47
400	3	197,05	71,05
600	4	192,08	69,66
800	5	187,10	68,31
1000	6	182,13	66,99
1200	7	177,15	65,69
1400	8	172,18	64,43
1600	9	167,20	63,20
1800	10	162,23	62,00
2000	11	157,25	60,82
2200	12	152,28	59,67
2400	13	147,30	58,55
2600	14	142,33	57,45
2800	15	137,35	56,40
3000	16	132,38	55,38
3200	17	127,40	54,38
3400	18	122,43	53,41
3600	19	117,45	52,48
3800	20	112,48	51,58
4000	21	107,50	50,70

Table 18: Discrete semi-wing cross section properties for Syncro aircraft.

This model has the advantage of reducing the solution time (since a single rectangular section substitutes the three sections of *Figure 35*); moreover, each element of the beam precisely reflects the reduction of dimensions from the root to the tip, as observed in *Table 18*.

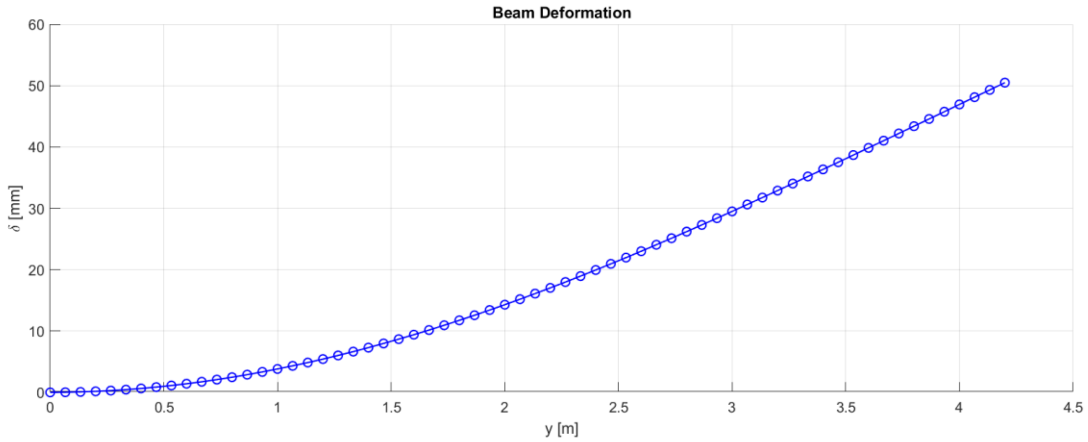

Figure 36: Static analysis z deformation for Syncro semi-wing, 4-th order McLaurin polynomials and n=1 loading at shear centre.

The results shown in *Figure 36* are a reasonable approximation of the data obtained from the several experimental analyses carried out on the test aircraft. More precisely, a specific loading condition (reported in *Appendix III*) has been used to set the calibration for the cross-section dimensions, while another deformation result has been used as a comparison for the validity of the results obtained. Since the method adopted is empirical, some further considerations about the results validity and meaning must be done:

- the cross-section loses all the properties related to the lamination of the composite materials, because an averaging process is carried out for the material properties. This means that it is symmetric, and shear-centre is at the centre of the cross section.
- The load is concentrated at the centre of the cross section, which is also the shear-centre of the rectangular section, thus no torsional effects are highlighted. This implies that this calibration is not sufficient to define the torsional stiffness of the beam structure.
- The relative positioning between the aerodynamic surface and the beam structure must be defined properly, to set the proper shear centre location respect to the aerodynamic loads.

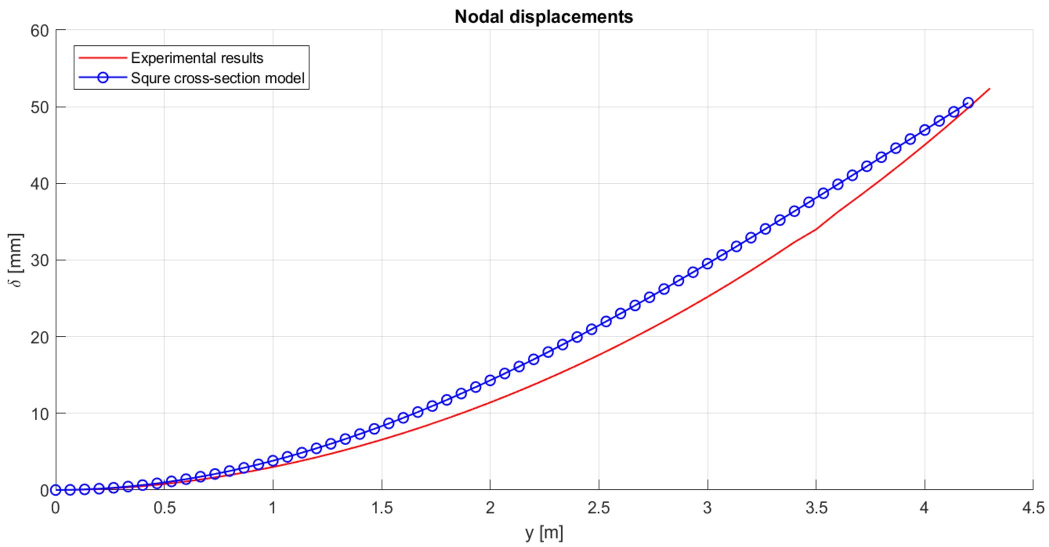

Figure 37: Static analysis results for Syncro semi-wing with 5-th order McLaurin polynomials and n=1 loading at shear centre. Comparison with experimental results.

Table 19 reports the different vertical (*z*) displacements obtained from the four McLaurin polynomial orders considered for the extremity node of each structural element that constitutes the beam. The data presented are consistent with the convergence analysis carried out in section *3.9.2*.

Nodal z displacements for right extremity node [m]				
Element	*McLaurin Polynomials order*			
	2-nd order	*3-rd order*	*4-th order*	*5-th order*
1	$1{,}684\cdot10^{-4}$	$1{,}699\cdot10^{-4}$	$1{,}700\cdot10^{-4}$	$1{,}701\cdot10^{-4}$
2	$6{,}386\cdot10^{-4}$	$6{,}418\cdot10^{-4}$	$6{,}421\cdot10^{-4}$	$6{,}424\cdot10^{-4}$
3	$1{,}408\cdot10^{-3}$	$1{,}413\cdot10^{-3}$	$1{,}413\cdot10^{-3}$	$1{,}414\cdot10^{-3}$
4	$2{,}467\cdot10^{-3}$	$2{,}475\cdot10^{-3}$	$2{,}475\cdot10^{-3}$	$2{,}477\cdot10^{-3}$
5	$3{,}807\cdot10^{-3}$	$3{,}818\cdot10^{-3}$	$3{,}818\cdot10^{-3}$	$3{,}821\cdot10^{-3}$
6	$5{,}416\cdot10^{-3}$	$5{,}429\cdot10^{-3}$	$5{,}430\cdot10^{-3}$	$5{,}434\cdot10^{-3}$
7	$7{,}281\cdot10^{-3}$	$7{,}298\cdot10^{-3}$	$7{,}299\cdot10^{-3}$	$7{,}304\cdot10^{-3}$
8	$9{,}388\cdot10^{-3}$	$9{,}409\cdot10^{-3}$	$9{,}410\cdot10^{-3}$	$9{,}416\cdot10^{-3}$
9	$1{,}172\cdot10^{-2}$	$1{,}175\cdot10^{-2}$	$1{,}175\cdot10^{-2}$	$1{,}176\cdot10^{-2}$
10	$1{,}426\cdot10^{-2}$	$1{,}430\cdot10^{-2}$	$1{,}430\cdot10^{-2}$	$1{,}431\cdot10^{-2}$
11	$1{,}700\cdot10^{-2}$	$1{,}703\cdot10^{-2}$	$1{,}704\cdot10^{-2}$	$1{,}705\cdot10^{-2}$
12	$1{,}991\cdot10^{-2}$	$1{,}994\cdot10^{-2}$	$1{,}995\cdot10^{-2}$	$1{,}996\cdot10^{-2}$
13	$2{,}296\cdot10^{-2}$	$2{,}301\cdot10^{-2}$	$2{,}301\cdot10^{-2}$	$2{,}303\cdot10^{-2}$
14	$2{,}615\cdot10^{-2}$	$2{,}620\cdot10^{-2}$	$2{,}620\cdot10^{-2}$	$2{,}622\cdot10^{-2}$
15	$2{,}945\cdot10^{-2}$	$2{,}950\cdot10^{-2}$	$2{,}950\cdot10^{-2}$	$2{,}952\cdot10^{-2}$
16	$3{,}283\cdot10^{-2}$	$3{,}289\cdot10^{-2}$	$3{,}289\cdot10^{-2}$	$3{,}291\cdot10^{-2}$
17	$3{,}628\cdot10^{-2}$	$3{,}634\cdot10^{-2}$	$3{,}635\cdot10^{-2}$	$3{,}637\cdot10^{-2}$
18	$3{,}978\cdot10^{-2}$	$3{,}984\cdot10^{-2}$	$3{,}985\cdot10^{-2}$	$3{,}988\cdot10^{-2}$
19	$4{,}331\cdot10^{-2}$	$4{,}338\cdot10^{-2}$	$4{,}338\cdot10^{-2}$	$4{,}341\cdot10^{-2}$
20	$4{,}685\cdot10^{-2}$	$4{,}692\cdot10^{-2}$	$4{,}693\cdot10^{-2}$	$4{,}696\cdot10^{-2}$
21	$5{,}040\cdot10^{-2}$	$5{,}048\cdot10^{-2}$	$5{,}048\cdot10^{-2}$	$5{,}052\cdot10^{-2}$

Table 19: Discrete semi-wing nodal z displacements for element node 2.

3.9.3.5 Pure twist section calibration

The analysis of results obtained in section *3.9.3.4* highlights that differential displacements for the extremities of the structure provide a torsional effect which is slightly the double of the one observed experimentally during load tests. A potentially valid solution to this problem is to calibrate cross-section properties to satisfy the real twist of the semi-wing, as shown in *Figure 38*. The torsional moment applied, and the consequent rotation angles obtained during the tests are reported in *Appendix III*.

The new calibrated section properties can be observed in *Table 20*, that underlines a good qualitative coherence between the simplified model and the real one, except for the tip of the semi-wing. This calibration provides a more rigid bending properties representation but can be used as an instrument for static aeroelasticity torsional divergence estimation.

y coordinate [mm]	*Element*	*Section width [mm]*	*Section height [mm]*
0	1	492,86	64,87
200	2	481,01	63,59
400	3	469,17	62,35
600	4	457,32	61,13
800	5	445,48	59,94
1000	6	433,63	58,78
1200	7	421,79	57,65
1400	8	409,94	56,54
1600	9	398,10	55,46
1800	10	386,25	54,40
2000	11	374,40	53,37
2200	12	362,56	52,36
2400	13	350,71	51,38
2600	14	338,87	50,42
2800	15	327,02	49,49
3000	16	315,18	48,60
3200	17	303,33	47,72
3400	18	291,49	46,87
3600	19	279,64	46,05
3800	20	267,80	45,26
4000	21	255,95	44,49

Table 20: Discrete semi-wing cross section properties for Syncro aircraft, torsional properties calibration.

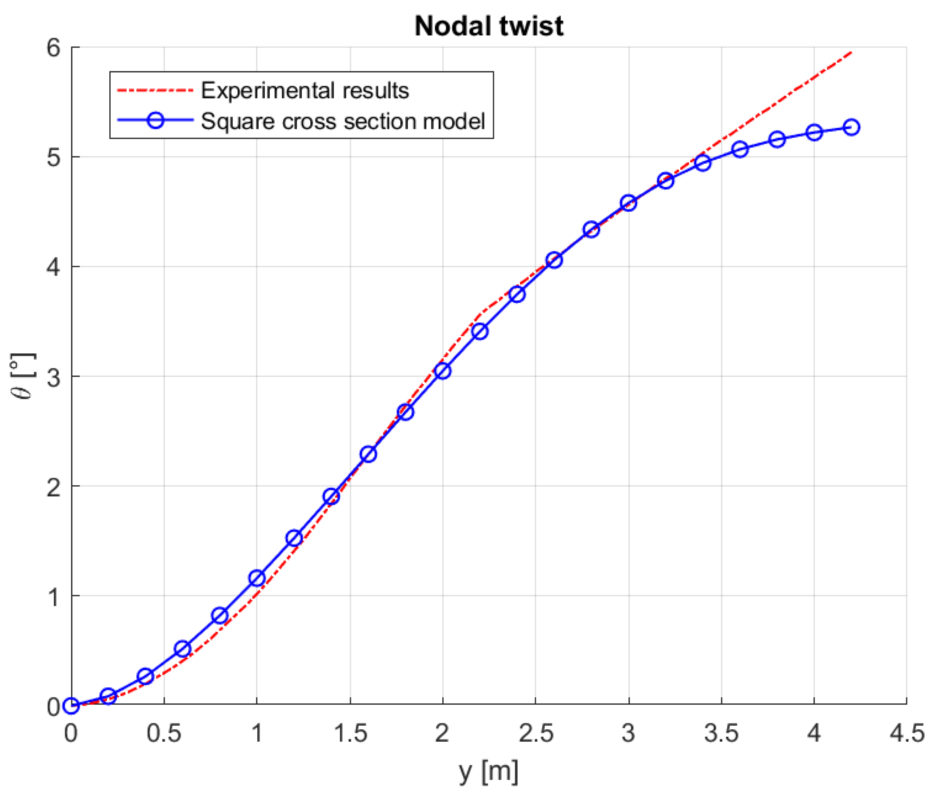

Figure 38: Static analysis results for Syncro semi-wing with 2-nd order McLaurin polynomials and twist test loading. Comparison with experimental results.

3.9.3.6 Modal analysis results

Once the model has been calibrated on the static deformation, the modal analysis can be executed to find the vibrational modes of the structure. *Table 21* reports the frequencies obtained for the three approximation orders that have been considered.

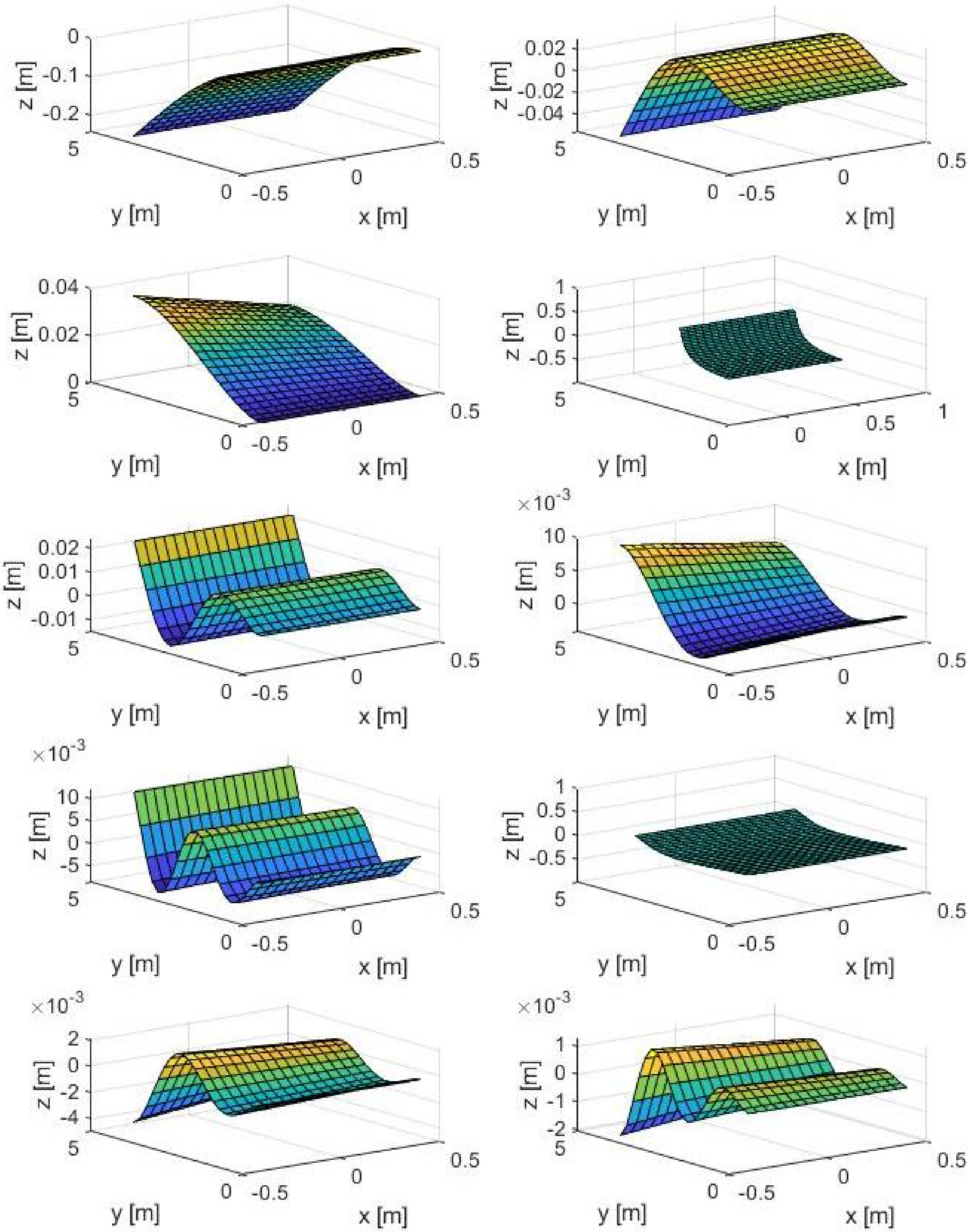

Figure 39: Modal analysis results for Syncro semi-wing with 4-nd order McLaurin polynomials.

Figure 39 represents the deformation of the beam obtained through the present code for the first 10 free vibrational modes. The following modes can be found starting from left to right and from top to bottom:

1. First pure z bending mode.
2. Second pure z bending mode.
3. First bending-torsional mode.
4. First x bending mode.
5. Third pure z bending mode.
6. Second bending-torsional mode.
7. Fourth pure z bending mode.
8. Second x bending mode.
9. Third bending-torsional mode.
10. Fourth bending-torsional mode.

Free vibrational frequencies [Hz]			
Mode	*2-nd order*	*3-rd order*	*4-th order*
1	37,80	37,76	37,75
2	174,81	174,31	174,25
3	215,40	209,06	205,10
4	250,30	249,50	249,46
5	443,03	440,57	440,41
6	517,99	492,55	482,92
7	830,81	823,32	822,99
8	858,06	830,48	828,77
9	915,59	851,92	835,26
10	1327,10	1287,90	1262,08

Table 21: Modal analysis results for square cross-section.

A final test has been carried out on the *I* shaped spar, to test an alternative solution methodology: the function *eig()*, that permits to evaluate the eigenvalues and eigenvectors of the free vibrational problem, can specify an additional parameter *'qz'*, recalling the Schur's decomposition. The computational time increases due to the time necessary for the decomposition process, but this solves the problems generated by the different materials that compose the beam and the ones related to the spanwise geometry variation (provided that the variations are not too rough).

3.9.4 Modal analysis results on composite materials beams

The present code can be applied on different types of structures, such as composite materials beams, that usually have orthotropic constitutive relations. The direction of lamination determines the variation of beam's structural properties both on static and modal analysis. In this sub-chapter, a series of results obtained for a constant cross section beam will be presented, with particular attention to the variability of vibrational frequencies due to the lamination angle that is considered. *Figure 40* represents the reference system adopted for fibres orientation, in particular:

a. 0°, fibres are parallel to the y axis.
b. ±45°, fibres have a positive/negative angle respect to y axis.
c. 90°, fibres are perpendicular to y axis.

Material properties (orthotropic material)			
Elastic Modulus Longitudinal direction	E_L = 132,5 GPa	*Elastic Modulus Transversal direction*	E_T = 10,8 GPa
Poisson's Ratio	*v* = 0,24	*Shear Modulus*	G = 5,7 GPa
Geometrical properties (constant along span)			
Section chord	c = 0,15 m	*Wingspan*	L = 1,50 m
Section height	h = 0,0045 m	*Sweep angle*	Λ = 0°
Structural Mesh			
Beam elements	20	*Element nodes*	4
Cross section McLaurin polynomials order		4-th	

Table 22: Orthotropic beam geometrical and material properties.

The generic orientation can be both positive or negative in modal analysis since the beam is symmetric and the consequent vibration frequencies that are obtained are the same. This is not valid for static aeroelasticity and flutter, where the airspeed direction determines the asymmetry of the problem.

The properties of the beam structure and the ones of the orthotropic material are presented in *Table 22*, while the first six frequencies for each lamination case are displayed in *Table 23*. In the same table, the relative percentual errors obtained from the comparison with the results of *MUL2 [18]* reference are presented. The reference system adopted implies that in the 0° condition the longitudinal Young's modulus (E_L) is aligned with *y* axis.

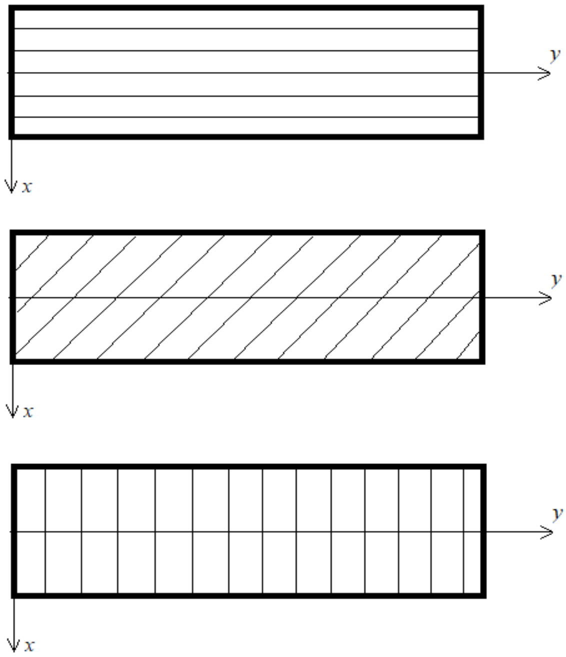

Figure 40: Lamination angles for an orthotropic beam (from top to bottom: 0°, 45°, 90°).

Lamination angle	**Modal frequency [Hz]**					
	1-st	**2-nd**	**3-rt**	**4-th**	**5-th**	**6-th**
0°	2,9921	18,7436	19,3078	52,4547	60,4431	93,8598
15°	1,9991	12,3332	28,7585	34,6863	63,4774	68,8128
% error	*3,6404%*	*3,5257%*	*4,9746%*	*3,6850%*	*3,1355%*	*3,9562%*
30°	1,2766	7,9813	22,5233	33,6265	40,5480	44,9974
% error	*1,7860%*	*1,8315%*	*2,0049%*	*4,9996%*	*1,2674%*	*2,3090%*
45°	0,9775	6,1162	17,1656	28,6812	31,4583	33,8814
% error	*1,5111%*	*1,5170%*	*1,5739%*	*3,3684%*	*1,1481%*	*1,6771%*
60°	0,8566	5,3640	15,0209	22,9341	28,0353	29,4759
% error	*2,0333%*	*2,0003%*	*2,0130%*	*2,5347%*	*1,7370%*	*2,1169%*
75°	0,8187	5,1300	14,3632	19,3454	27,0738	28,1484
% error	*2,4391%*	*2,4381%*	*2,4370%*	*0,6285%*	*2,3884%*	*2,4417%*
90°	0,8142	5,1020	14,2852	18,1470	26,9586	27,9924
% error	*2,7493%*	*2,7434%*	*2,7447%*	*0,0924%*	*2,7175%*	*2,7484%*

Table 23: Orthotropic beam modal frequencies (4-th order McLaurin polynomials cross-section discretization).

Chapter 4

Splining Process

The final step necessary to complete a static or dynamic aeroelastic analysis is the splining process. The method described in the following pages is the Infinite Plate Spline (IPS). To proceed with the splining process, which is at the base of structural-aerodynamic coupling, two grids of points must be known:

1. Pseudo Structural Points, a grid of points that are defined on the undeformed beam *x-y* plane. Although the beam has a 1D geometry from the formal point of view, these points are defined considering their expansion through the chordwise direction.

2. Aerodynamic *Load* and *Control Points* grid, that has already been defined in *Chapter 2* and contains the reference points for each aerodynamic panel of the wing.

The final aim of IPS is to map the structural displacements of Pseudo Structural Points obtained from the modal analysis on the aerodynamic *Load* and *Control points* grid. This permits to evaluate aerodynamic loads on the deformed semi-wing by the means of slopes and displacements at *Load* and *Control points* that establish boundary conditions for Vortex Lattice Method and Doublet Lattice Method application.

4.1 Infinite Plate Spline method

Infinite plate spline method is an interpolation method that refers to an infinite uniform surface and was developed by *Harder and Desmarais* to evaluate displacements and slopes on 2D aerodynamic surfaces. It permits to evaluate the displacement function for a surface according to a discrete number of points (that are the Pseudo Structural Points) for which this displacement is known. The governing differential equation which is at the base of the problem formulation is reported in equation *4.1*:

$$D\nabla^4 w = q \qquad (4.1)$$

Where q is the distributed load on the plate, D is the uniform plate bending stiffness and w is the plate deflection. The problem is solved in polar coordinates, thus the differential operator and x, y coordinates are defined in equation *4.2*:

$$\begin{gathered} x = rcos(\theta) \\ y = rsin(\theta) \\ \nabla^4 = \frac{1}{r}\frac{d}{dr}\left\{r\frac{d}{dr}\left[\frac{1}{r}\frac{d}{dr}\left(r\frac{d}{dr}\right)\right]\right\} \end{gathered} \qquad (4.2)$$

For the sake of brevity, the solution process for the fourth order differential equation (*4.1*) will not be reported in this work but can be easily found in the work of *Varello A. [14] (p. 155-157)* that has been used as the reference for IPS model construction. The result is reported in *4.3*:

$$w(r) = A + Br^2 + Fr^2 \ln(r^2)$$

$$A = C_0, B = C_1, F = \frac{P}{16\pi D} \qquad (4.3)$$

Where C_0, C_1 are two coefficients that will be obtained from the application of boundary conditions (and interpolation at different points) and *D* is the bending stiffness. The hypotheses made in these evaluations are:

- No distributed loads are applied on the infinite plate.
- A single concentrated load is applied.
- The load is applied at the origin of the coordinate system.

The most general case, which is the one used in this work, is characterized by multiple loads applied on the infinite plate that are located on a generic number of points all over the plane. For this reason, r_i is defined as the distance between the point where the vertical displacement of the plate is evaluated ($w(x,y)$) and the load application point, as shown in *Figure 41*. The general expression for *w* displacements is obtained through the superposition of the effects of the single loads, as reported in *4.4*:

$$w(x,y) = \sum_{i=1}^{N} [A_i + B_i r_i^2 + F_i r_i^2 \ln(r_i^2)] \qquad (4.4)$$

Where *N* is the number of concentrated loads (P_i) applied on the plate. *r* and r_i are thus:

$$r^2 = x^2 + y^2$$

$$r_i^2 = (x - x_i)^2 + (y - y_i)^2 \qquad (4.5)$$

The previous formula will finally be rewritten as a function of x_i, y_i, *r* and θ following the procedure proposed by *Varello A. [14] (p.158-163)*, that will not be reported in this work for simplicity. The result is a system of equations that must be solved in order to determine the coefficients that describe the plate deformation starting from the known displacements at *N Load Points*.

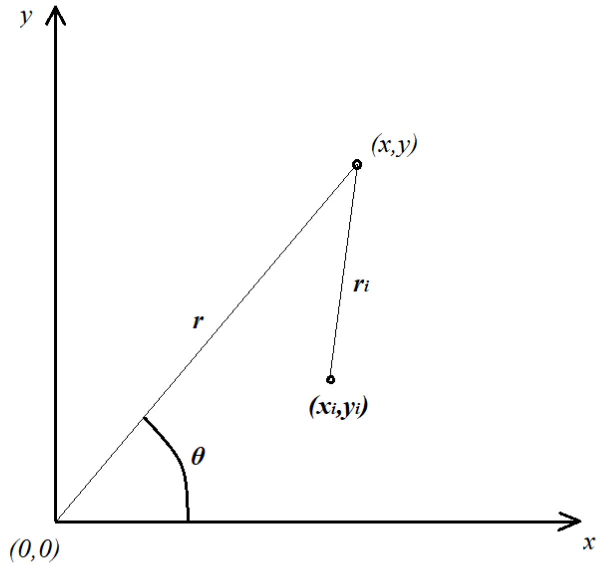

Figure 41: Coordinate system and load application points representation.

The final formulation that describes the transverse displacements of the plate charged by *N* concentrated loads located on the same number of *Load Points* is:

$$w(x,y) = a_0 + a_1 x + a_2 y + \sum_{i=1}^{N} [F_i r_i^2 \ln(r_i^2)]$$

$$where: K_i(x,y) = r_i^2 \ln(r_i^2) \qquad (4.6)$$

Where the unknowns of the spline formulation (*N+3*) are the following coefficients: a_0, a_1, a_2, F_i, that will be determined assigning *N* displacements at *N Load Points* and the boundary conditions at infinity (*4.7*).

$$\sum_{i=1}^{N} F_i = 0\,, \sum_{i=1}^{N} F_i x_i = 0\,, \sum_{i=1}^{N} F_i y_i = 0 \tag{4.7}$$

In the end, Pseudo Structural Points are the ones where the displacements are known, thus the formulation in equation *4.8* is adopted to define the displacement on each point:

$$\begin{gathered} w_j(x_j, y_j) = a_0 + a_1 x_j + a_2 y_j + \sum_{i=1}^{N} [F_i K_{ij}(x, y)] \\ {r_{ij}}^2 = (x_i - x_j)^2 + (y_i - y_j)^2 \\ K_{ij} = {r_{ij}}^2 \ln({r_{ij}}^2) \end{gathered} \tag{4.8}$$

Where $K_{ij} = K_{ji}$ and $K_{ij} = 0$ when *i=j*. Subscript *j* refers to each Pseudo Structural Point in which the vertical displacement is evaluated, while subscript *i* establishes the relation with all the *Load Points* considered. Equations in *4.8* can be rewritten in matrixial form introducing the following vectors and matrices:

$$\begin{gathered} \{w\} = \{w_1, w_2, \dots, w_N\}^T \qquad [R] = \begin{bmatrix} 1 & x_1 & y_1 \\ 1 & x_2 & y_2 \\ \dots & \dots & \dots \\ 1 & x_N & y_N \end{bmatrix} \\ \{a\} = \{a_0, a_1, a_2\}^T \\ \{F\} = \{F_1, F_2, \dots, F_N\}^T \qquad [K] = \begin{bmatrix} K_{11} & K_{12} & \dots & K_{1N} \\ K_{21} & K_{22} & \dots & K_{2N} \\ \dots & \dots & \dots & \dots \\ K_{N1} & K_{N2} & \dots & K_{NN} \end{bmatrix} \end{gathered} \tag{4.9}$$

The system that, given all Pseudo Structural Points, permits to evaluate the coefficients of the infinite plate is:

$$\begin{gathered} \begin{cases} [0] = [0]\{a\} + [R]^T\{F\} \\ [w] = [R]\{a\} + [K]\{F\} \end{cases} \\ \begin{Bmatrix} \{0\} \\ \{w\} \end{Bmatrix} = \begin{bmatrix} [0] & [R]^T \\ [R] & [K] \end{bmatrix} \begin{Bmatrix} \{a\} \\ \{F\} \end{Bmatrix} = [G] \begin{Bmatrix} \{a\} \\ \{F\} \end{Bmatrix} \end{gathered} \tag{4.10}$$

All the data necessary to evaluate displacements on aerodynamic *Control* and *Load Points* are now available: the next sections of this chapter will explain how these computations are actuated.

4.2 Load and control points notation

Before proceeding with the evaluation of deformations and displacements for the aerodynamic surfaces, a brief resume about the notable points must be carried out:

- *Control Points* (X_{cont}, Y_{cont}) are the coordinates of control points on the wing plane surface. The third coordinate will be obtained from the splining process (Z_{cont}).
- *Load Points* (X_{load}, Y_{load}), that analogously are the positions of load points in the same reference system. Vertical displacement Z_{load} will be obtained as a result from splining.

A discrepancy emerges from the coupling of *VLM* with *DLM* and the structural model if aerodynamic panels are not located on a 2D surface due to an asymmetric camber line. In the following chapters, the semi-wing will be considered planar to avoid the discrepancy between the two aerodynamic codes, even thought that an error is introduced in the aerodynamic properties' representation.

4.2.1 Displacements at Load and Control points

For the sake of simplicity, the present section will explain how slopes at aerodynamic *Control Points* can be obtained for the case where sweep angle is zero (this permits to avoid the use of superscripts related to local and global reference systems and to explain more clearly the processes involved).

The coefficients a_0, a_1, a_2, F_j are known from chapter *4.1*, thus for the *k-th Control Point* the following equation describes its displacement along *z* coordinate:

$$Z_{cont_k}(X_{cont_k}, Y_{cont_k}) = a_0 + a_1 X_{cont_k} + a_2 Y_{cont_k} + \sum_{j=1}^{N_{PS}} F_j K_{kj} \tag{4.11}$$

$$\begin{gathered} K_{kj} = {R_{kj}}^2 \ln({R_{kj}}^2) \\ {R_{kj}}^2 = (X_{cont_k} - x_j)^2 + (Y_{cont_k} - y_j)^2 \end{gathered} \tag{4.12}$$

Where N_{PS} is the number of structural points used for the spline interpolation and N_{AP} is the number of aerodynamic panels: $k = 1,2,\dots,N_{AP}$. In matrixial notation this is equivalent to the solution of the system:

$$\begin{Bmatrix} Z_{cont_1} \\ Z_{cont_2} \\ Z_{cont_3} \\ \cdots \\ Z_{cont_{N_{AP}}} \end{Bmatrix} = \begin{bmatrix} 1 & X_{cont_1} & Y_{cont_1} & K_{11} & \cdots & K_{1N_{PS}} \\ 1 & X_{cont_2} & Y_{cont_2} & K_{21} & \cdots & K_{2N_{PS}} \\ 1 & X_{cont_3} & Y_{cont_3} & K_{31} & \cdots & K_{3N_{PS}} \\ \cdots & \cdots & \cdots & \cdots & \cdots & \cdots \\ 1 & X_{cont_{N_{AP}}} & Y_{cont_{N_{AP}}} & K_{N_{AP}1} & \cdots & K_{N_{AP}N_{PS}} \end{bmatrix} \begin{Bmatrix} a_0 \\ a_1 \\ a_2 \\ F_1 \\ \cdots \\ F_{N_{PS}} \end{Bmatrix} \tag{4.13}$$

$$in\ compact\ form: \{Z_{cont}\} = \boldsymbol{D_{cont}} \begin{Bmatrix} \{a\} \\ \{F\} \end{Bmatrix}$$

$$\begin{Bmatrix} Z_{load_1} \\ Z_{load_2} \\ Z_{load_3} \\ \cdots \\ Z_{load_{N_{AP}}} \end{Bmatrix} = \begin{bmatrix} 1 & X_{load_1} & Y_{load_1} & K_{11} & \cdots & K_{1N_{PS}} \\ 1 & X_{load_2} & Y_{load_2} & K_{21} & \cdots & K_{2N_{PS}} \\ 1 & X_{load_3} & Y_{load_3} & K_{31} & \cdots & K_{3N_{PS}} \\ \cdots & \cdots & \cdots & \cdots & \cdots & \cdots \\ 1 & X_{load_{N_{AP}}} & Y_{load_{N_{AP}}} & K_{N_{AP}1} & \cdots & K_{N_{AP}N_{PS}} \end{bmatrix} \begin{Bmatrix} a_0 \\ a_1 \\ a_2 \\ F_1 \\ \cdots \\ F_{N_{PS}} \end{Bmatrix} \tag{4.14}$$

$$in\ compact\ form: \{Z_{load}\} = \boldsymbol{D_{load}} \begin{Bmatrix} \{a\} \\ \{F\} \end{Bmatrix}$$

4.2.2 Slopes at Control points

Since the focus is set on slopes of the panels at *Control Points*, the following relations are obtained:

$$\frac{\partial Z_{cont_k}}{\partial x}(X_{cont_k}, Y_{cont_k}) = a_1 + \sum_{j=1}^{N_{PS}} F_j \frac{\partial K_{kj}}{\partial x} = a_1 + \sum_{j=1}^{N_{PS}} F_j DK_{kj} \tag{4.15}$$

Where:

$$DK_{kj} = \frac{\partial K_{kj}}{\partial x} = 2\left(X_{cont_k} - x_j\right)\left[1 + \ln\left(R_{kj}{}^2\right)\right] \tag{4.16}$$

As shown in *4.13*, even slopes can be computed in matrixial form (*4.17*). Now all the data concerning the boundary conditions for aerodynamic panels have been evaluated; since the pseudo structural points used for splining process will be the data resulting from modal analysis, slopes and displacements obtained from *4.13*, *4.14* and *4.17* will be the input data for Doublet Lattice Method evaluations.

$$\begin{Bmatrix} \dfrac{\partial Z_{load_1}}{\partial x} \\ \dfrac{\partial Z_{load_2}}{\partial x} \\ \dfrac{\partial Z_{load_3}}{\partial x} \\ \cdots \\ \dfrac{\partial Z_{load_{N_{AP}}}}{\partial x} \end{Bmatrix} = \begin{bmatrix} 0 & 1 & 0 & DK_{11} & \cdots & DK_{1N_{PS}} \\ 0 & 1 & 0 & DK_{21} & \cdots & DK_{2N_{PS}} \\ 0 & 1 & 0 & DK_{31} & \cdots & DK_{3N_{PS}} \\ \cdots & \cdots & \cdots & \cdots & \cdots & \cdots \\ 0 & 1 & 0 & DK_{N_{AP}1} & \cdots & DK_{N_{AP}N_{PS}} \end{bmatrix} \begin{Bmatrix} a_0 \\ a_1 \\ a_2 \\ F_1 \\ \cdots \\ F_{N_{PS}} \end{Bmatrix} \tag{4.17}$$

$$in\ compact\ form\text{:}\ \left\{\frac{\partial Z_{load}}{\partial x}\right\} = \boldsymbol{DK_{load}} \begin{Bmatrix} \{a\} \\ \{F\} \end{Bmatrix}$$

4.3 Unsteady boundary condition for DLM

The procedures described in this chapter permit to recall equation *2.5*, used in Doublet Lattice Method for the evaluation of pressure coefficients. It is now possible to express the normal wash (normalized using the speed of the aircraft) in its most general shape, which includes the steady and unsteady contributes obtained in *chapter 4.1.* The results are shown in equation *4.18*.

$$\begin{gathered} \{C_P\} = [D]^{-1}\{w\} \\ \{w\} = i\frac{\omega}{V_\infty}\{Z_{cont}\} + \left\{\frac{\partial Z_{cont}}{\partial x}\right\} \end{gathered} \tag{4.18}$$

Where ω is the input frequency and i is the imaginary unit. If the input frequency reduces to zero, the boundary condition becomes the one presented in *4.19*, where the imaginary term is no more present:

$$\{w\} = \left\{\frac{\partial Z_{cont}}{\partial x}\right\} \tag{4.19}$$

This chapter completes the description of all the elements necessary to execute static aeroelasticity and flutter analysis for a conventional trapezoidal semi-wing. The next step will be presented in the following chapters, where the solution method will be described.

4.4 IPS Code Development and Results

This section is developed separately from the static and modal analysis code to obtain a structured solving process. In the following chapters, a main program that recalls and links the different analyses will be written.

The splining process based on IPS is relatively simple to develop and the main issues that can be identified are related to the accuracy of the grid. An appropriate grid size must be defined, and the consequent computational time must be benchmarked.

4.4.1 Main code development steps

It is noteworthy that the present chapter has the aim to explain the main concepts of the routines used and the main sections of the code. Following the same schedule used for the other MatLab® programs presented in this work, these main code sections can be identified:

Data input section, where data obtained through the structural code are loaded (from *Displacements.mat* output file) and are used to evaluate displacements on Pseudo Structural Points (PSP). The result will be a set of three matrices that contain the coordinates of the considered points:

- *spline_x*, coordinates of PSP in chordwise direction (*Figure 42*).
- *spline_y*, coordinates of PSP in spanwise direction (*Figure 42*).
- *spline_w*, that contains *z* displacements for PSP, evaluated through the results of structural analysis (both static and free vibrational one).

In order to study flutter phenomenon, the previous splining process is carried out for every modal frequency considered in the structural model (for example the first 10 frequencies). *Figure 42* reports a general example of Pseudo Structural grid on a rectangular semi-wing, that permits a better focus on the problem: PSP coordinates are selected to guarantee a good approximation of aerodynamic displacements.

The elements that can be observed in this figure (*42*) are:

- Undeformed wing PSP, that are represented in black.
- Deformed wing PSP, that are represented in red.
- Wing contour, identified by three black segments.
- Root section of the wing is located at $y=0$ according reference system adopted.
- Tip section is located at $y=2.14m$.
- Chordwise coordinates range from $x=-0.3m$ to $x=0.3m$.

The deformed configuration is referred to the first free vibrational frequency of the modal analysis carried out on the semi-wing and the resulting points reported on *Figure 42* are concerned by *z* displacements.

Spline coefficients evaluation section, in which Pseudo Structural Points are used to evaluate the coefficients described in *chapter 4.2*. The results are obtained through the resolution of the following system of equations:

$$\begin{Bmatrix} \{0\} \\ \{w\} \end{Bmatrix} = [G] \begin{Bmatrix} \{a\} \\ \{F\} \end{Bmatrix}$$

$$thus: \begin{Bmatrix} \{a\} \\ \{F\} \end{Bmatrix} = [G]^{-1} \begin{Bmatrix} \{0\} \\ \{w\} \end{Bmatrix} \tag{4.20}$$

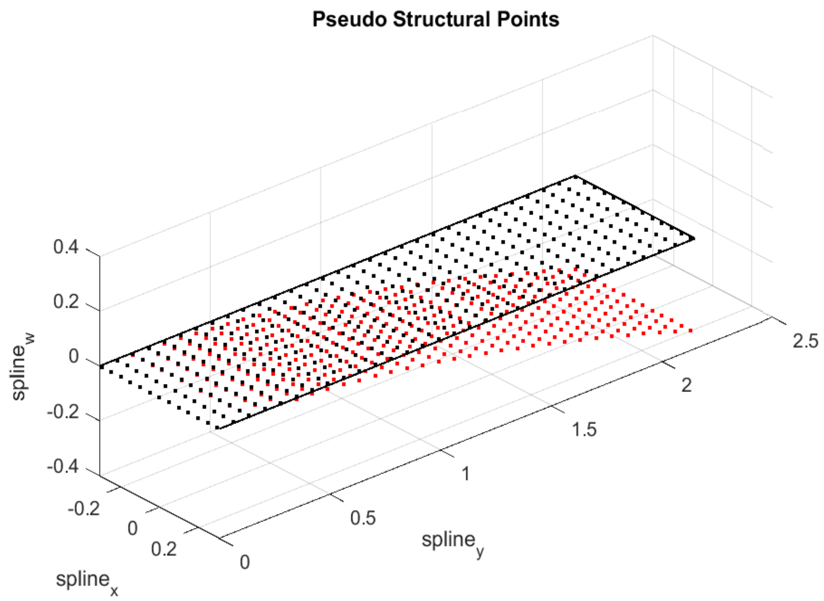

Figure 42: Pseudo Structural Points for a generic simple semi-wing.

Aerodynamic points displacements and slopes evaluation section, where aerodynamic *Load* and *Control Points* for each panel defined in VLM code are imported from *Aerodynamic_ControlPoints.mat* file. They are used to obtain displacements and slopes at the points of interest through equations *4.13*, *4.14* and *4.17*. The results of this section are three vectors defined as:

- Displacements at *Load Points* (*w_aer_l*).
- Displacements at *Control Points* (*w_aer_c*).
- Slopes at *Control Points* (*w_aerprime_c*).

All the equations used are presented in the previous chapter and no particular routines are involved in these calculations, except for the cycles necessary to build the matrices of displacements and slopes from the previous vectors. In this way, the same indices used for the panels in aerodynamic codes can be used.

DLM input data section, in which the final results are saved in *AeroDisplacementsforDLM.mat* file. It will be the input file used for DLM evaluations: all the data necessary to carry out the aeroelastic analysis are now available.

4.4.2 Code verification and convergence considerations

The present code permits to change the number of Pseudo Structural Points used for the splining process. As PSP number increases, two opposite effects can be observed:

- A more accurate approximation for aerodynamic *Control Points* displacements is obtained.
- The solution time increases as the rank of the matrices becomes greater. In particular, the solution time is proportional to the square of the number of PSP selected.

For this reason, a balance between the two effects must be chosen, that also satisfies the requirements established for Pseudo Structural Points positioning:

1. The points cannot be aligned along a line.
2. Two or more PSP cannot be located on the same *spline_x*, *spline_y* coordinates.

These conditions would define a singularity condition for *[G]* matrix, thus failing to define the spline plane, as stated by *Varello A. [14] p.168*.

4.4.3 Syncro wing geometry simplification

Once the aerodynamic surface and the structure of the wing have been defined, the splining process can be executed, provided that the relative position between spars and the leading edge is correctly established. This operation is done by simply adding a constant term to the x coordinate of all *Load Points* and *Control Points*: displacements in z coordinate are correctly evaluated through this technique.

Obviously, this does not affect the coordinates of aerodynamic points in VLM and DLM codes, since only slopes and displacements are exported from the splining code. *Figure 43* represents the configuration that has been studied, where the following elements can be identified:

- Aerodynamic surface contour, represented in black.
- Front spar, in red.
- Rear spar, in blue.
- Quarter chord line, which is the dotted black line.

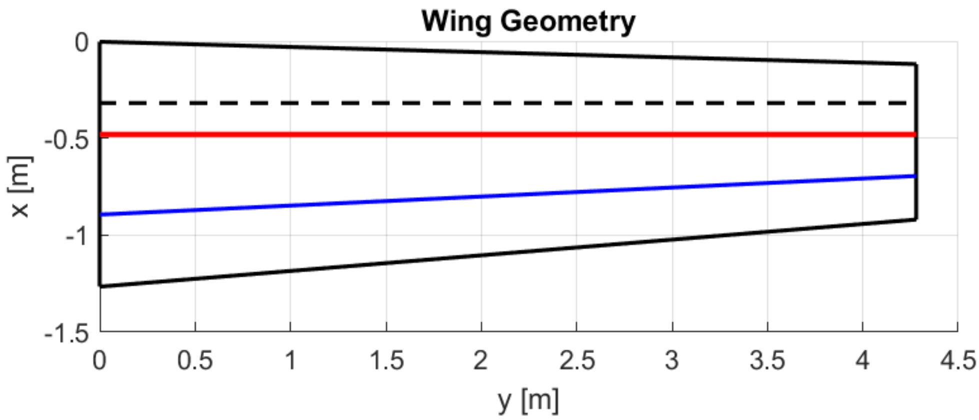

Figure 43: Syncro wing geometry configuration. Relation between structural elements position and aerodynamic surface collocation.

If the structure is simplified as a rectangular cross-section beam, the position of the equivalent semi-wing shear centre must be the same of the real semi-wing one, as well as the torsional stiffness of each element. The second condition is satisfied since in chapter *3.9.3.5* the calibration of the beam section has been executed, while the analysis related to the shear centre position will follow these criteria:

- In static aeroelasticity analysis, the position of shear centre will be varied in order to identify the consequent variation of the torsional divergence velocity. This provides a complete analysis of the limits for the aircraft's flight envelope.

- In flutter analysis, the relative position between shear centre and aerodynamic centre will be fixed to the real condition.

Chapter 5

Aeroelastic model

The considerations made in the introduction of this work in a qualitative way will be explained in detail in the two main sections of the present chapter, with particular attention to the analysis methods used. This is particularly important for flutter evaluations, where different solution strategies can be adopted: the focus will be set on k-method and p-k method (section *5.2*).

5.1 Static aeroelastic model

The static aeroelastic analysis aim is to evaluate the static deformation of a semi-wing loaded with steady aerodynamic forces computed through Vortex Lattice Method. These evaluations are carried out for a range of airspeeds that permits to evaluate how the static response of the wing structure changes, as will be observed later in this section. The reference used to describe the interaction between aerodynamics and structural deformation is the work of *Varello A. [14] p. 183-190*.

5.1.1 Steady aerodynamic loads vector

The first element necessary for the static aeroelastic analysis is represented by the vector that contains all the dimensionless pressure loads on each panel of the semi-wing, as written in equation *5.1*:

$$\Delta \boldsymbol{p} = \frac{\Delta \boldsymbol{p'}}{\frac{1}{2}\rho_\infty V_\infty^2} \tag{5.1}$$

Where: $\Delta \boldsymbol{p}$ is the dimensionless pressure load vector, while $\Delta \boldsymbol{p'}$ is the dimensional pressure load.

From this expression, it is possible to define for each aerodynamic panel (i) the three force components acting in 3D space, thanks to the quantities defined in *chapter 2.3*:

- Δx_i is the average chordwise dimension of the generic panel i. It is equal to the chord of the panel measured at its middle spanwise coordinate, since their shape is trapezoidal or rectangular.
- Δy_i is the spanwise dimension of the considered panel.
- n_{xi}, n_{yi}, n_{zi} are the components of the *i-th* panel normal vector in global coordinates.
- $\Delta \boldsymbol{p_i}$ is the dimensionless pressure load on the panel.

The three force components in three-dimensional space are thus written in equation *5.2*:

$$\begin{aligned} L_{i_x} &= \frac{1}{2}\rho_\infty V_\infty^2 (\Delta x_i \Delta y_i n_{xi} \Delta \boldsymbol{p_i}) \\ L_{i_y} &= \frac{1}{2}\rho_\infty V_\infty^2 (\Delta x_i \Delta y_i n_{zi} \Delta \boldsymbol{p_i}) \\ L_{i_z} &= \frac{1}{2}\rho_\infty V_\infty^2 (\Delta x_i \Delta y_i n_{zi} \Delta \boldsymbol{p_i}) \end{aligned} \tag{5.2}$$

The next step is the assembly of the vector representing aerodynamic forces acting on the considered surfaces: this is done by introducing a diagonal matrix that multiplies the dimensionless pressure loads vector ($\boldsymbol{\Delta p}$) and permits to obtain the forces vector, named $\boldsymbol{L}$:

$$\boldsymbol{L} = \frac{1}{2}\rho_\infty V_\infty^2 \boldsymbol{I_D} \boldsymbol{\Delta p} \tag{5.3}$$

Where the matrix $\boldsymbol{I_D}$ is defined as reported in equation *5.4*, (N_{AP} is the total number of aerodynamic panels):

$$\boldsymbol{I_D} = \begin{bmatrix} \Delta x_1 \Delta y_1 & 0 & \dots & 0 \\ 0 & \Delta x_2 \Delta y_2 & \dots & 0 \\ \dots & \dots & \dots & 0 \\ 0 & 0 & 0 & \Delta x_{N_{AP}} \Delta y_{N_{AP}} \end{bmatrix} \tag{5.4}$$

Now that all the geometric and constant quantities have been defined, VLM results are retrieved to evaluate the dimensionless pressure loads through equation *5.5*:

$$\begin{gathered} \boldsymbol{w} = \boldsymbol{A} \cdot \boldsymbol{\Delta p} \\ \boldsymbol{\Delta p} = [\boldsymbol{A}]^{-1} \cdot \boldsymbol{w} \end{gathered} \tag{5.5}$$

Where $\boldsymbol{A}$ is the aerodynamic influence coefficients matrix for the considered discretization and $\boldsymbol{w}$ is the vector composed by dimensionless normal velocity components to the *i-th* panel, as written in *5.6*.

$$\{w\} = \boldsymbol{w} = \frac{\boldsymbol{w'}}{V_\infty} \tag{5.6}$$

Moreover, a relation between the aerodynamic boundary condition (dimensionless normal wash) and the structure deformation can be established through the results of the splining process. The slope at the aerodynamic *Control Point* is equal to the dimensionless normal wash, as stated in *chapter 4.3*:

$$\{w\} = \left\{\frac{\partial Z_{cont}}{\partial x}\right\} \tag{5.7}$$

This also permits to relate the displacements in z direction to the structural degrees of freedom, since slopes at aerodynamic *Control Points* are connected to the structural DOFs through the IPS splining process. In the following lines, some equations and procedures described in *chapter 4* will be recalled, in order to make clearer the definition of the aerodynamic stiffness matrix, which is the core of the static aeroelasticity problem. Starting from equation *5.5* and introducing the result presented in *5.7*, equation *5.8* can be written:

$$\boldsymbol{\Delta p} = [\boldsymbol{A}]^{-1} \left\{\frac{\partial Z_{cont}}{\partial x}\right\} \tag{5.8}$$

Where the vector of slopes at *Control Points* can be obtained from equation *5.9* as a function of the structural nodal degrees of freedom (the link between aerodynamic loading and structural displacements is here introduced for the first time):

$$\left\{\frac{\partial Z_{cont}}{\partial x}\right\} = \boldsymbol{DK_{cont}} \cdot \boldsymbol{a_{a\to s}} \cdot \boldsymbol{q_z} \tag{5.9}$$

The matrix $\boldsymbol{DK_{cont}}$ is defined in an analogue way to the one presented in equation *4.17* for *Load Points* slopes, while the term $\boldsymbol{a_{a\to s}}$ represents the connection between aerodynamic *Load Points* and structural degrees of freedom and is composed by the following matrices:

$$\boldsymbol{a_{a\to s}} = \boldsymbol{S} \cdot \boldsymbol{Y} \tag{5.10}$$

Where the matrix concerning the rotation of the reference system is not considered, since for the sake of simplicity the problem description is made in the zero-sweep angle case. The definitions of $\boldsymbol{S}$ and $\boldsymbol{Y}$ are presented in equation *5.11* (the definition of $\boldsymbol{S}$ recalls equation *4.10*) and *5.12*:

$$\begin{gathered}\boldsymbol{S}^* = [G]^{-1} = \begin{bmatrix} [0] & [R]^T \\ [R] & [K] \end{bmatrix}^{-1} \\ \boldsymbol{S} = \boldsymbol{S}^*_{\boldsymbol{ij}} \\ with: i = 1, \dots, N_N + 3 \ (rows) \\ j = 4, \dots, N_N + 3 \ (columns)\end{gathered} \tag{5.11}$$

$\boldsymbol{Y}$ relates the coordinates of Pseudo Structural Points (that in this situation are the *Load Points* of each aerodynamic panel) to the structural degrees of freedom in *z* global coordinate system direction: the aerodynamic influence matrix and the consequent pressures multiplied by $\boldsymbol{Y}$ are equivalent to the application of a generic set of loads on PSP. Each row of the matrix has the following expression:

$$\begin{gathered}\boldsymbol{Y_j} = F_\tau(X_{load}, Z_{load}) \cdot N_i(Y_{load}) \\ with: \tau = 1, \dots, N_u \ (polynomial\ order) \\ i = 1, \dots, 4 \ (nodes) \\ j = 1, \dots, N_{AP} \ (rows)\end{gathered} \tag{5.12}$$

The number of columns of the matrix is equal to the number of degrees of freedom of the problem (where the clamped wing condition has not been applied yet), thus $\boldsymbol{Y}$ is different from zero only for the degrees of freedom ($\boldsymbol{q_z}$) influenced by the PSP load.

The expression of aerodynamic forces can be now written in its explicit formulation:

$$\boldsymbol{L} = \frac{1}{2}\rho_\infty V_\infty^2 \boldsymbol{I_D} \cdot [\boldsymbol{A}]^{-1} \cdot \boldsymbol{DK_{cont}} \cdot \boldsymbol{S} \cdot \boldsymbol{Y} \cdot \boldsymbol{q_z} \tag{5.13}$$

5.1.2 Aerodynamic stiffness matrix

Chapter 5.1.1 results include the value of loading forces on every aerodynamic panel that constitutes the lifting surface of the semi-wing. In particular, loads on aerodynamic *Load Points* are known and thus they can be transferred to the structural nodes. This permits to evaluate the out of plane structural beam deformation through the Principle of Virtual Displacements, with an analogue method to the one presented in *chapter 3* for the solution of the static structural deformation problem. Equation *5.14* represents the virtual work of aerodynamic load forces and the one due to structural loads:

$$\delta L_{aero\ loads} = \{\delta Z_{load}\}^T \cdot \boldsymbol{L} = [\boldsymbol{D_{load}} \cdot \boldsymbol{a_{a\to s}} \cdot \delta \boldsymbol{q_z}]^T \cdot \boldsymbol{L} \tag{5.14}$$

$$\delta L_{aero\ loads} = \delta \boldsymbol{q_z}^{\boldsymbol{T}} \cdot [\boldsymbol{a_{a \to s}}]^T \cdot [\boldsymbol{D_{load}}]^T \cdot \boldsymbol{L}$$

$$\delta L_{struct\ loads} = \delta \boldsymbol{q_z}^{\boldsymbol{T}} \cdot \boldsymbol{L_{struct}} \tag{5.14}$$

Equation *5.15* shows how structural loads energetically equivalent to the aerodynamic ones are obtained through the Principle of Virtual Displacements application:

$$\delta L_{aero\ loads} = \delta L_{struct\ loads}$$

$$\delta \boldsymbol{q_z}^{\boldsymbol{T}} \cdot [\boldsymbol{a_{a \to s}}]^T \cdot [\boldsymbol{D_{load}}]^T \cdot \boldsymbol{L} = \delta \boldsymbol{q_z}^{\boldsymbol{T}} \cdot \boldsymbol{L_{struct}} \tag{5.15}$$

$$\boldsymbol{L_{struct}} = [\boldsymbol{a_{a \to s}}]^T \cdot [\boldsymbol{D_{load}}]^T \cdot \boldsymbol{L}$$

In the end, the substitution of load forces vector in the structural loads one leads to the following expression:

$$\boldsymbol{L_{struct}} = [\boldsymbol{a_{a \to s}}]^T \cdot [\boldsymbol{D_{load}}]^T \cdot \boldsymbol{L}$$

$$\boldsymbol{L_{struct}} = [\boldsymbol{a_{a \to s}}]^T \cdot [\boldsymbol{D_{load}}]^T \cdot \frac{1}{2} \rho_\infty V_\infty^2 \boldsymbol{I_D} \cdot [\boldsymbol{A}]^{-1} \cdot \boldsymbol{DK_{cont}} \cdot \boldsymbol{a_{a \to s}} \cdot \boldsymbol{q_z} \tag{5.16}$$

$$\boldsymbol{L_{struct}} = \frac{1}{2} \rho_\infty V_\infty^2 [\boldsymbol{a_{a \to s}}]^T \cdot [\boldsymbol{D_{load}}]^T \cdot \boldsymbol{I_D} \cdot [\boldsymbol{A}]^{-1} \cdot [\boldsymbol{DK_{cont}}] \cdot [\boldsymbol{a_{a \to s}}] \cdot \boldsymbol{q_z}$$

Equation *5.16* can be rewritten in a simplified formulation that introduces the aerodynamic stiffness matrix, which has the same dimensions of the structural stiffness matrix (a square matrix with a rank equal to the number of degrees of freedom of the structural problem):

$$\boldsymbol{L_{struct}} = \frac{1}{2} \rho_\infty V_\infty^2 [\boldsymbol{a_{a \to s}}]^T \cdot [\boldsymbol{D_{load}}]^T \cdot \boldsymbol{I_D} \cdot [\boldsymbol{A}]^{-1} \cdot [\boldsymbol{DK_{cont}}] \cdot [\boldsymbol{a_{a \to s}}] \cdot \boldsymbol{q_z}$$

$$\boldsymbol{L_{struct}} = -\boldsymbol{K_{aero_z}} \cdot \boldsymbol{q_z} \tag{5.17}$$

5.1.3 Aeroelastic stiffness matrix and problem solution

The results shown in equation *5.17* and the static deformation system of equations obtained in equation *3.43* can be finally compared as written in *5.18, 5.19* and *5.20*: the matrix that is obtained is the aeroelastic stiffness matrix, that considers the effects of aerodynamic loadings on the structural stiffness of the beam in this 1D case study. In particular, as the aerodynamic forces change due to air density or airspeed variations, the consequent aerodynamic stiffness matrix changes and determines different deformation conditions.

It is extremely important to underline that all the previous equations consider only *z* degrees of freedom, thus the aerodynamic stiffness matrix must be properly manipulated to be summed to the structural one. This operation is a simplification, since the aeroelastic coupling is analysed only in the lift loading direction. The other terms of the expanded aerodynamic matrix are thus equal to zero.

$$\begin{cases} \boldsymbol{L_{struct}} = \boldsymbol{K_{struct}} \cdot q \\ \boldsymbol{L_{struct}} = -\boldsymbol{K_{aero}} \cdot q \end{cases} \tag{5.18}$$

$$\boldsymbol{K_{struct}} \cdot \boldsymbol{q} = -\boldsymbol{K_{aero}} \cdot \boldsymbol{q} \tag{5.19}$$

$$\begin{gathered} [\boldsymbol{K_{struct}} + \boldsymbol{K_{aero}}] \cdot \boldsymbol{q} = 0 \\ [\boldsymbol{K_{aeroelastic}}] \cdot \boldsymbol{q} = 0 \end{gathered} \tag{5.20}$$

Equation *5.20* solution is a singular vector since no perturbation or load is applied to the 1D structural geometry. If the right-hand side of *5.20* is different from zero, the deformation of the structure can be mapped along *y* coordinate of the beam reference system and the behaviour of the deformation can be studied as a function of:

- The relative position between the beam shear centre and aerodynamic loads.
- Air density, and thus the altitude of the aircraft according to ISA atmosphere data (*Appendix I*).
- Aircraft True Airspeed (TAS).

The right-hand side load vector is different from zero as the shape of the semi-wing is deformed, thus the structure does not lie on the *z=0* plane (it is important to remember the hypothesis of no dihedral angle for the beam). This perturbation is supplied by the boundary condition given for the VLM problem resolution, which was presented in the previous lines as:

$$\{w\} = \left\{\frac{\partial Z_{cont}}{\partial x}\right\} = \boldsymbol{DK_{cont}} \cdot \boldsymbol{S} \cdot \Delta\boldsymbol{x} \tag{5.21}$$

The vector $\Delta\boldsymbol{x}$ represents the analogue effect of introducing an angle of attack, that causes the aerodynamic forces to be non-zero. The following steps necessary to evaluate the right-hand side vector are equal to the ones presented in section *5.1.1* and *5.1.2*, thus after applying the Principle of Virtual Displacements:

$$\boldsymbol{L_{RHS_z}} = \frac{1}{2}\rho_\infty V_\infty^2 [\boldsymbol{a_{a\to s}}]^T \cdot [\boldsymbol{D_{load}}]^T \cdot \boldsymbol{I_D} \cdot [\boldsymbol{A}]^{-1} \cdot [\boldsymbol{DK_{cont}}] \cdot \boldsymbol{S} \cdot \Delta\boldsymbol{x} \tag{5.22}$$

From *5.22* it is possible to write the final formulation of the static aeroelasticity problem:

$$\begin{gathered} [\boldsymbol{K_{struct}} + \boldsymbol{K_{aero}}] \cdot \boldsymbol{q} = \boldsymbol{L_{RHS}} \\ [\boldsymbol{K_{aeroelastic}}] \cdot \boldsymbol{q} = \boldsymbol{L_{RHS}} \end{gathered} \tag{5.23}$$

The previous procedure may introduce long solution time and inaccuracies. On the other hand, the classical aeroelastic analysis approach is based on the eigenvalue problem solution obtained from equation *5.20*, which is rewritten in the following shape:

$$\begin{gathered} [\boldsymbol{K_{struct}} + \boldsymbol{K_{aero}}] \cdot \boldsymbol{q} = 0 \\ [\boldsymbol{K_{struct}} - \lambda \boldsymbol{K^*_{aero}}] \cdot \boldsymbol{q} = 0 \\ [[\boldsymbol{K^*_{aero}}]^{-1}\boldsymbol{K_{struct}} - \lambda \boldsymbol{I}] \cdot \boldsymbol{q} = 0 \end{gathered} \tag{5.24}$$

Where $\lambda = \frac{1}{2}\rho V_\infty^2$ is the dynamic pressure parameter. The relation between $\boldsymbol{K_{aero}^*}$ and $\boldsymbol{K_{aero}}$ is:

$$\boldsymbol{K_{aero}} = \lambda \boldsymbol{K_{aero}^*} = \frac{1}{2}\rho V_\infty^2 \boldsymbol{K_{aero}^*} \tag{5.25}$$

This formulation is not adopted due to the singularities that may be obtained from the inversion of $\boldsymbol{K_{aero}^*}$ matrix, but the alternative solution is to provide the inversion of structural stiffness matrix, multiply it by aerodynamic stiffness matrix and compute the eigenvalues of their product. The maximum eigenvalue that is obtained from this procedure is the inverse of λ, which has been introduced in equation *5.24*; divergence velocity can be easily obtained from this term. The obtained results will be reported in *chapter 6*.

5.2 Dynamic aeroelastic model: flutter

In the following lines, the focus will be set on the most used flutter investigation strategies.

5.2.1 General problem description

While static aeroelasticity concerns only static deformations and loads, flutter is a more complex problem and can be represented by the governing equations of motion in time domain:

$$\boldsymbol{M}\ddot{u}(t) + \boldsymbol{C}\dot{u}(t) + \boldsymbol{K}u(t) = \boldsymbol{F}(t) \tag{5.26}$$

Where the terms concerned are the following:

- *M* is the mass matrix, related to inertial effects mentioned in the previous lines.
- *C* is the structural damping matrix, related to the dissipation of energy due to structural deformation.
- *K* is the stiffness matrix, representing the effect of elastic forces.
- *F* is the applied force vector, including both aerodynamic forces and generic external ones.
- *u(t)* is the time dependent vector representing the degrees of freedom of the problem.

In all the next evaluations, the structural damping matrix *[C]* will be considered equal to zero and the applied force vector will be represented only by aerodynamic forces. Nevertheless, for a first description of the equation solution, the formulation with *F(t)=0* will be used:

$$\boldsymbol{M}\ddot{u}(t) + \boldsymbol{C}\dot{u}(t) + \boldsymbol{K}u(t) = 0 \tag{5.27}$$

If the problem has only a single degree of freedom the matrices *M, C, K* become single constant terms and *u(t)* is the displacement of the considered degree of freedom (associated to its velocity $\dot{u}(t)$ and acceleration $\ddot{u}(t)$). The solution of this equation is obtained considering that the displacement is represented in a harmonic form:

$$\begin{gathered} u(t) = \bar{u}e^{\lambda t} \\ \dot{u}(t) = \lambda\bar{u}e^{\lambda t} \\ \ddot{u}(t) = \lambda^2\bar{u}e^{\lambda t} \end{gathered} \tag{5.28}$$

This leads to the characteristic polynomial, which is obtained in the next lines:

$$\boldsymbol{M}\lambda^2\bar{u}e^{\lambda t} + \boldsymbol{C}\lambda\bar{u}e^{\lambda t} + \boldsymbol{K}\bar{u}e^{\lambda t} = 0$$
$$\boldsymbol{M}\lambda^2 + \boldsymbol{C}\lambda + \boldsymbol{K} = 0 \tag{5.29}$$

The solution of the previous second-degree polynomial equation permits to evaluate the eigenvalues of the problem, that can be real or conjugate complexes, depending on *M, C, K* values. If they are both real and negative the solution is aperiodic and stable, otherwise it would be unstable. In the case of conjugate complexes, the solution is a periodic motion with a pulsation determined by the relations:

$$\lambda_{1,2} = \frac{-\boldsymbol{C} \pm \sqrt{\boldsymbol{C}^2 - 4\boldsymbol{MK}}}{2\boldsymbol{M}} = \lambda_R \pm \mathrm{i}\lambda_I \tag{5.30}$$

$$\omega_n = \sqrt{\frac{\boldsymbol{K}}{\boldsymbol{M}}} \qquad \omega = \sqrt{\frac{\boldsymbol{K}}{\boldsymbol{M}} - \left(\frac{\boldsymbol{C}}{2\boldsymbol{M}}\right)^2} \tag{5.31}$$

$$f_n = \frac{\omega_n}{2\pi} \qquad f = \frac{\omega}{2\pi} \tag{5.32}$$

Where the imaginary part determines the oscillation period; (ω_n, f_n) refers to the harmonic oscillation while (ω, f) refers to the damped ones.

It is now possible to explain more clearly the insurgence of flutter phenomenon, which corresponds to the solution of the previous equation in the situation of undamped oscillations, that is the limit between an asymptotically stable solution and an unstable one. The second one is not acceptable for the operative conditions of an aircraft since it leads to disruptive structural deformations and a probable loss of the vehicle. In *Figure 44* all the types of oscillating solutions are represented to describe clearly the conditions explained.

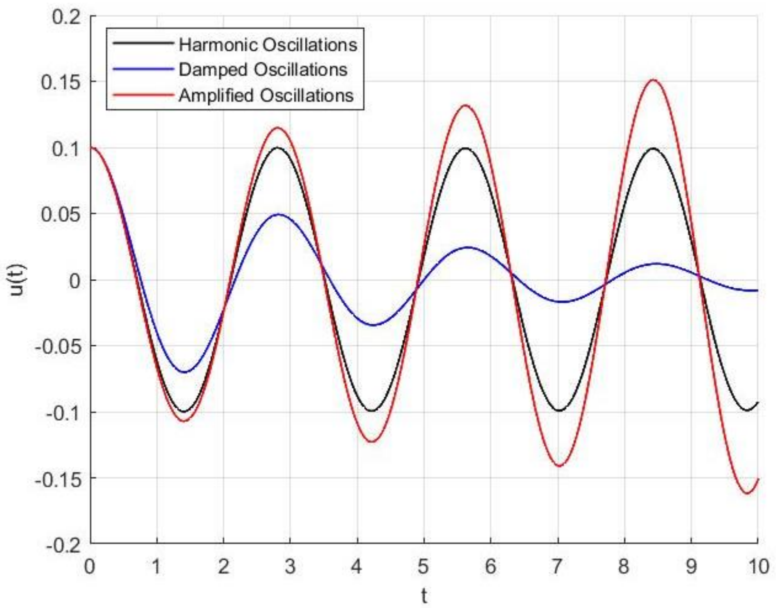

Figure 44: Damped, harmonic, and amplified oscillations for a single degree of freedom system.

5.2.2 p-k method

The solution for the equations of motion presented in chapter *5.2.1* can be obtained in the most general case in different ways and with a variable degree of approximation. The case of a multiple variable system can be represented in time domain or in frequencies domain (through a proper transformation explained later). In frequency domain, the non-dimensional differential operator p can be introduced to reformulate flutter equation and its real and imaginary part study permits to identify the occurrence of this phenomenon. As is explained by *Hassig H. [15] p. 885-887*, p is defined as:

$$p = \frac{b}{V_\infty}\left(\frac{d}{dt}\right) \tag{5.33}$$

Where b is the reference length (usually equal to half of the chord length) and V_∞ is the true airspeed.

Flutter equation, or equation of motion, can be expressed as (with the hypothesis introduced in section *5.2.1*):

$$\begin{gathered} \boldsymbol{M}\ddot{\boldsymbol{u}}(t) + \boldsymbol{K}\boldsymbol{u}(t) = \boldsymbol{F}(t) \\ where{:}\, u(t) = \boldsymbol{\Phi} q(t) \end{gathered} \tag{5.34}$$

It is important to underline that the vector q contains the degrees of freedom for the considered modes (Φ), since the flutter problem involves the free vibrational solution of structural problem. The term *F(t)* is represented by the aerodynamic forces acting on the wing surface, that in matrixial formulation are:

$$\boldsymbol{F} = \frac{1}{2}\rho {V_\infty}^2 \boldsymbol{Q} \tag{5.35}$$

The equation's system obtained from *5.34* is rewritten in *8.36* as described by *Petrolo M. [13] p. 50-56*:

$$\left[\frac{{V_\infty}^2}{b^2}\widetilde{\boldsymbol{M}}p^2 + \widetilde{\boldsymbol{K}} - \frac{1}{2}\rho {V_\infty}^2 \widetilde{\boldsymbol{Q}}(ik)\right]\{q(p)\} = 0 \tag{5.36}$$

Where the three matrices presented are:

- $\widetilde{\boldsymbol{M}_{ij}} = \boldsymbol{\Phi}^{\boldsymbol{T}}\boldsymbol{M}\boldsymbol{\Phi}$, M is the mass matrix of the beam structure (described in chapter *3.7*).
- $\widetilde{\boldsymbol{K}_{ii}} = \omega_i^2 \widetilde{\boldsymbol{M}_{ij}}$, K is the stiffness matrix obtained from the structural model (described in chapter *3.7*).
- *** $\widetilde{\boldsymbol{Q}_{ij}} = \sum_{N=1}^{N_{AP}} \Delta p_j^N(ik) \tilde{Z}_i^N\, S_{AP}^N$, which is the aerodynamic term obtained from DLM.

Since aerodynamic forces are computed through the DLM code developed in this work, it is important to underline that the hypothesis of harmonic forces has been considered. For this reason, *p-k method* introduces an error in the system of equations solution: the pure harmonic nature of aerodynamic forces is not consistent with the damped sinusoidal motion assumed for p, but it can be reputed valid in proximity of harmonic oscillations. The use of more accurate methods, both for aerodynamic non-stationary forces definition and for the solution of the equations of motion system (such as the g-method), are not considered in this work.

*** $\widetilde{\boldsymbol{Q}_{ij}}(ik) = \sum_{N=1}^{N_{AP}} \Delta \boldsymbol{p}_j^N(ik) \tilde{Z}_i^N S_{AP}^N$	
$\Delta \boldsymbol{p}_j^N(ik)$	It is the pressure jump due to the *j-th* modal shape set of motions. This value is computed for the *N-th* aerodynamic panel and evaluated for the considered reduced frequency (k).
$\tilde{Z}_i^N$	Is the *i-th* transversal set of motions evaluated on the *N-th* aerodynamic panel starting from the results of free vibrational analysis (this is done by means of the splining process).
S_{AP}^N	Is the area of the *N-th* aerodynamic panel.

Table 24: Aerodynamic matrix terms definition through DLM and IPS splining results.

The solution of *5.36* is obtained imposing the determinant equal to zero, thus the expression of p is a polynomial with real coefficients that leads to conjugate complex roots:

$$p = \gamma k \pm ik \tag{5.37}$$

Where i is the imaginary unit, k is the reduced frequency and γ is the decay rate. These terms are defined as:

$$\gamma = \frac{1}{2\pi} \ln\left(\frac{a_{n+1}}{a_n}\right)$$
$$a_n, a_{n+1}: amplitudes\ of\ successive\ oscillations$$
$$(5.38)$$
$$k = \frac{\omega b}{V_\infty}$$
$$\omega: oscillation\ frequency$$

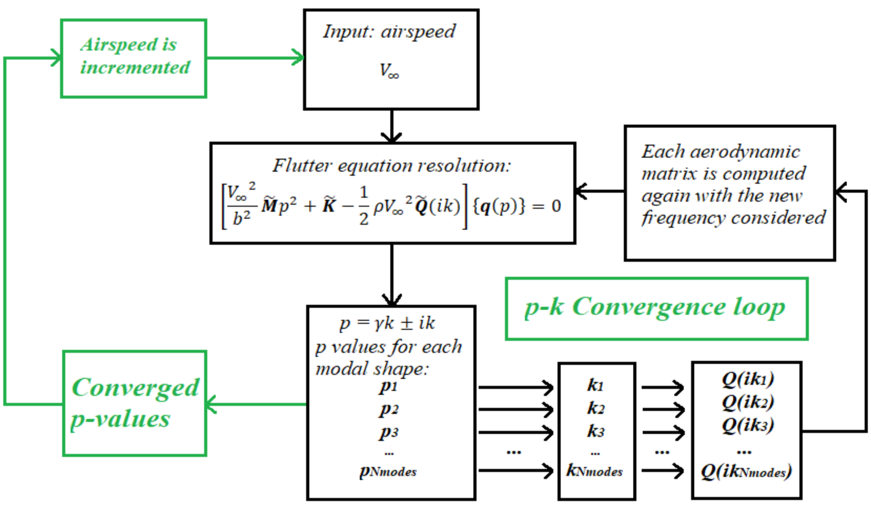

Figure 45: p-k method algorithm for a flutter problem with Nmodes modal shapes.

For every true airspeed considered, the vector of p values (*10x1* if the number of modal natural frequencies considered is equal to *10*) must be computed iteratively. Indeed, the k value obtained from p will not be equal to the one used for the aerodynamic evaluations. For this reason, the procedure presented in *Figure 45* will be adopted until the tolerance conditions are satisfied.

5.2.3 k method

The method presented in *5.2.2* can lead to convergence problems related to the identification of each mode reduced frequency. For this reason, an alternative solution that can be adopted is the one provided by the k-method, which is based on the same motion equations, but in an alternative shape:

$$\left[\widetilde{\boldsymbol{K}} - \left\{\widetilde{\boldsymbol{M}} + \frac{\frac{1}{2}\rho b^2}{k^2}\widetilde{\boldsymbol{Q}}(k)\right\}\left(\frac{\omega^2}{1+ig}\right)\right]\{q\} = 0 \tag{5.39}$$

Where the three matrices presented are the same of equation *5.36*, while:

- ω is the dimensional frequency ($2\pi f$).
- g is the structural damping required for harmonic motion.

The equation is solved sequentially on a series of k values for which the aerodynamic matrix is interpolated through Doublet Lattice Method: this avoids the iteration process involved in p-k method. This method requires short computational times, but it can occasionally generate some inaccuracies due to the "looping" of frequencies and damping, as described by *Dale M. Pitt [16] p. 1*. k-Method solution is valid only when $g=0$ and the structural motion is neutrally stable, as well as the aerodynamic motion.

The results obtained from this type of analysis are usually displayed on two plots that show the adimensional damping and the oscillation frequency for each considered speed. The first crossing from a negative damping condition to a positive one determines flutter speed, while the flutter frequency can be identified at the same velocity for the considered fluttering mode. The solution of the system of equations *5.39* brings to a complex eigenvalues vector which has the same length of the considered number of modes. Each vector is evaluated for a certain k value and permits to compute damping and frequency for each vibrational mode:

$$\begin{gathered} Frequency\colon \omega = \frac{1}{\sqrt{Re(\lambda)}} \\ Damping\colon g = \frac{Im(\lambda)}{Re(\lambda)} \\ Velocity\colon V = \frac{\omega b}{k} \end{gathered} \tag{5.40}$$

These three parameters permit to completely identify the fluttering mode and its main characteristics. As will be underlined in *chapter 6*, this method permits to study flutter insurgence on flat plates modelled through 1D structural models and VLM-DLM, but some limitations are introduced by the structural model limitations: the accuracy of the present structural model and of aerodynamic models influence the results obtained.

Chapter 6

Static Aeroelasticity and Flutter Results

This chapter will be the central part of the present work, since it reports the development of analysis methods used for static and dynamic aeroelasticity and the main results that are obtained. For the sake of brevity, only some of the possible studies will be shown, while this instrument can be adapted to many different cases.

6.1 Static Aeroelasticity code development

A practical approach has been adopted for this type of analysis, since the aim is to provide an instrument that computes autonomously divergence speed. For this reason, the command prompt permits to set the air density and the relative position between aerodynamic surface and beam structure shear centre. Inside this routine, the following code sections can be identified.

Static aeroelasticity data input section, where the data from VLM code are loaded from the proper file. It is important to underline that the code previously presented has been modified for this aim: the new code evaluates the aerodynamic influence coefficients matrices only for the considered semi-wing, coherently with the structural representation of the beam that has been adopted. Also, air density is defined in this section and sets the altitude at which the aircraft is flying.

Structural code resolution with shear centre and aerodynamic centre relative positioning section, where the final part of the static structural code is retrieved and the relative positioning between aerodynamic centre and shear centre is set. In this part, aerodynamic loads are applied at *Load Points* to furnish a basis for IPS splining process, since the output of this section is the vector of static displacements for the structural degrees of freedom.

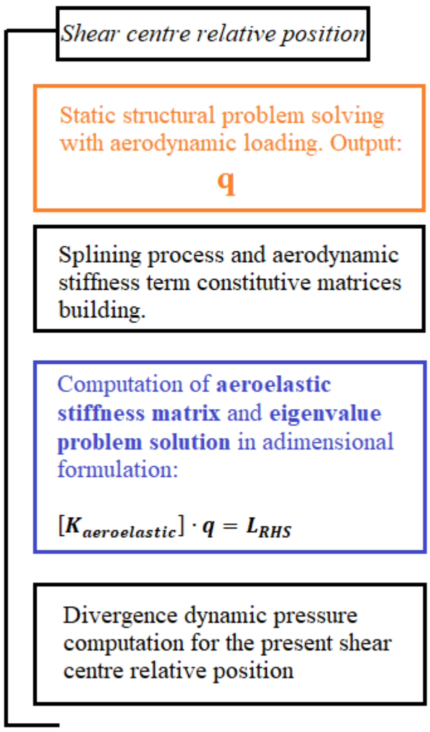

Figure 46: Main static aeroelasticity code sections.

Aerodynamic points correlation to structural model and splining section, where the aerodynamic points are properly translated to respect the relative positioning between shear centre and aerodynamic centre. Moreover, the code lines developed in the IPS splining chapter are used to evaluate the matrices relating the surfaces deflection at *Load Points* and *Control Points*. According to *chapter 5.1*, the following outputs are obtained from this section:

$$[\boldsymbol{DK_{cont}}] \tag{6.1}$$

$$[\boldsymbol{D_{load}}] \tag{6.2}$$

Aerodynamic stiffness term constitutive matrices section, in which the matrices of equation *6.3* are built up. The routines of this section are based on equations *5.11* and *5.12*; all the code lines involved are structured to respect the discretization imposed from VLM and structural code.

$$[\boldsymbol{a}_{a\rightarrow s}] = \boldsymbol{S}\cdot\boldsymbol{Y} \tag{6.3}$$

Divergence speed computation section, where the adimensional aerodynamic stiffness matrix is built using the previously defined components. Once this matrix has been obtained and has been multiplied by the inverse of the structural stiffness one, the eigenvalues are computed. The inverse of the maximum one, as explained in the previous chapter, leads to the divergence dynamic pressure.

Post processing: divergence evaluation section. In this part of the code, the divergence velocity for each shear centre relative position is identified by the first eigenvalue of the obtained matrix.

6.2 Flutter code development

The core section of k-method code is reported in this work, since it shows in a simple way how the equations of motion are obtained from structural and aerodynamic data and how the related unsteady aerodynamics matrices are computed for each reduced frequency. Three main sections can be identified.

Input data section, where the number of structural modes is selected. Frequencies and reference chord are consequently evaluated. In particular, the modal analysis results are loaded from the previously defined *Displacements_Modal.mat* data file (output of the modal analysis code).

Matrices generation and eigenvalue problem solution section, in which the following matrices are built:

- $\widetilde{\boldsymbol{M}_{\iota\jmath}} = \boldsymbol{\Phi}^{\boldsymbol{T}}\boldsymbol{M}\boldsymbol{\Phi}$

- $\widetilde{\boldsymbol{K}_{\iota\iota}} = \omega_i^2\widetilde{\boldsymbol{M}_{\iota\jmath}}$

- $\widetilde{\boldsymbol{Q}_{\iota\jmath}} = \sum_{N=1}^{N_{AP}} \Delta\boldsymbol{p}_j^N(ik)\tilde{Z}_i^N\, S_{AP}^N.$

It is important to underline that $\widetilde{\boldsymbol{Q}_{\iota\jmath}}$ depends on the input reduced frequency, thus it must be evaluated for every k value that has been considered. The solution time is determined by the number of input frequencies that are considered and by the number of aerodynamic panels for the semi-wing, since for every k value the DLM function is executed to determine $\widetilde{\boldsymbol{Q}_{\iota\jmath}}$.

DLM function section, that is a modified Doublet Lattice Method code, realized properly to evaluate quickly the unsteady aerodynamics contribute for each mode that has been considered. The main equations involved in the adimensionalized pressure jump evaluation for each panel and for each mode are reported in *6.4*:

$$\begin{gathered}\{C_P\} = [D]^{-1}\{w\}_{mode} \\ \{w\}_{mode} = i\frac{\omega}{V_\infty}\{Z_{cont}\}_{mode} + \left\{\frac{\partial Z_{cont}}{\partial x}\right\}_{mode}\end{gathered} \tag{6.4}$$

Where $\frac{\omega}{V_\infty} = k\frac{c_{mean}}{2}$, $\{Z_{cont}\}_{mode}$ are the displacements at *Control Points* for the considered mode and $\left\{\frac{\partial Z_{cont}}{\partial x}\right\}_{mode}$ are the slopes of aerodynamic panels at that points.

6.3 Static Aeroelasticity results

The code used for static aeroelasticity analysis has been tested on some structure examples to evaluate the capabilities of this instrument in the practical field. For all cases, aerodynamic properties that have been considered are the ones associated to the VLM model validated through the *Athena Vortex Lattice [11]* code.

6.3.1 Constant cross-section test beam

The first model is an isotropic semi-wing with a rectangular cross-section and constant properties along spanwise coordinates. Its main characteristics are reported in *Table 25*:

Material properties (isotropic material)			
Elastic Modulus	E = 75 GPa	*Poisson's Ratio*	$\nu = 0{,}33$
Shear Modulus	G = 28 GPa	*Density*	$\rho = 2700\ kg/m^3$
Geometrical properties (constant along span)			
Section chord	c = 0,5 m	*Wingspan*	L = 4,28 m
Section height	h = 0,01 m	*Sweep angle*	$\Lambda = 0°$
Structural Mesh			
Beam elements	20	*Element nodes*	4
Cross section McLaurin polynomials order	3-rd	*DOFs (clamped boundary condition)*	1800
Aerodynamic Mesh (equally spaced grid)			
Chordwise panel's number		10	
Spanwise panel's number		20	
Panel's total number		200	

Table 25: Test beam structure properties.

A series of simple static load conditions have been considered for the beam structure of *Table 25*, where loads obtained from the aerodynamic code are applied to the structure to test its behaviour.

The result of the divergence analysis is reported in *Figure 47*, following the specifications of *Table 26* (that establish the relative positioning between aerodynamic *Load Points*, *Control Points,* and structural points). *Load* and *Control Points* are translated by the distance needed to establish the correct shear centre relative position, to guarantee that the slopes at *Control Points* for each aerodynamic panel are assigned correctly.

Torsional Divergence: test case analysis	
Aerodynamic Chord	$c = 0{,}500\ m$
Span	$L = 4{,}28\ m$
Shear centre position	$x_0 = c/2 = 0{,}250\ m$
Aerodynamic Centre Location	$x_{ac} = c/4 = 0{,}125\ m$ **
Air density	$\rho = 1{,}225\ kg/m^3$
Torsional stiffness	$J = ch^3/3$

Table 26: Test semi-wing aerodynamic properties.

***Aerodynamic centre position is evaluated at the root section of the semi-wing, and it is represented by an axis parallel to y one, since sweep angle is null.*

At the same time, a simple model based on the strip theory is used as a verification instrument for the present code. The input properties are reported in *Table 26* and the results obtained through this model are:

$$q_D = \frac{GJ}{cC_{L\alpha}(x_0 - x_{ac})}\left(\frac{\pi}{2L}\right)^2 = 1{,}862 \cdot 10^3\ Pa$$

$$V_D = \sqrt{\frac{2q_D}{\rho}} = \sqrt{\frac{2 \cdot 1{,}862 \cdot 10^3}{1{,}225}} = 55{,}14\,\frac{m}{s} \tag{6.5}$$

That can be compared with the ones obtained from the code developed in this work, as written in *Table 27*:

Model	***Divergence speed***
Strip theory	55,14 m/s
Present code	57,58 m/s

Table 27: Static aeroelasticity results comparison.

The results from strip theory are an approximation since aerodynamic loads are considered as a unique force applied at 25% of chord from the leading edge; moreover, the divergence condition is determined only by the torsional deflection, while the interaction with bending and vertical displacements is not properly considered. It is important to underline that the angular lift coefficient is set to the value obtained from Vortex Lattice Method (VLM) evaluations.

The results obtained from the present code show a divergence speed that is greater than the one obtained from the other theory. This can be due to the aerodynamic lift distribution determined by the aerodynamic influence coefficients matrix. At the same time, the consistence of the present theory results has been proved through the variation of several discretization parameters.

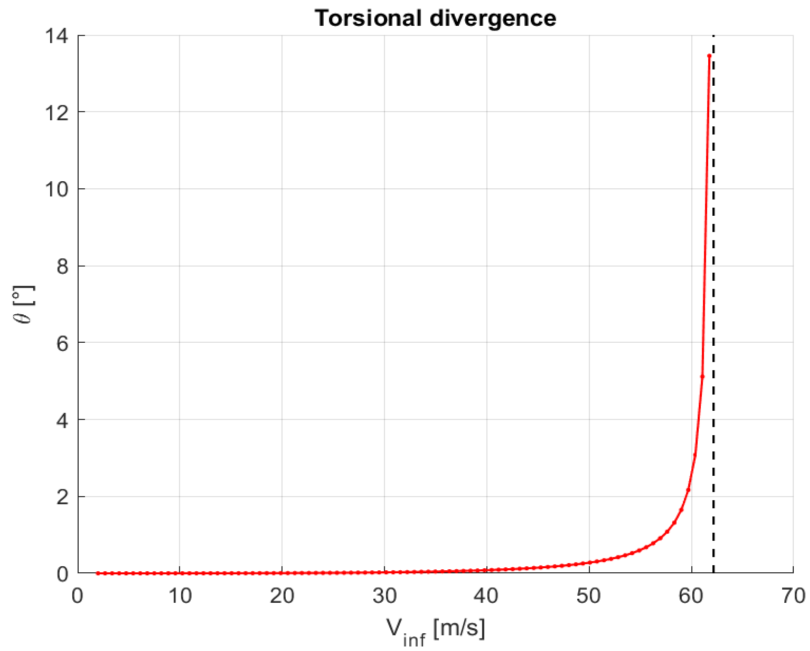

Figure 47: Tip angular deflection behaviour for a generic test semi-wing, 3-rd order McLaurin polynomials.

In the following table, the focus will be set on the effect of different orders of approximation used for the cross-section behaviour. This will permit to establish the coherence and convergence of the model. As is shown in *Table 28*, the growth of the cross-section approximation order leads to a lower divergence speed, even thought that the variation is limited. The use of *3-rd* and *4-th* order polynomials leads to the same result, except for variations lower than 1/100 of the measure unit (m/s). This behaviour can be justified by the fact that the second order approximation does not well represent torsional effects. Once the test model results have been analysed, the study moves to the Syncro aircraft wing model.

Cross-section approximation order	***Divergence velocity***
2-nd order McLaurin Polynomials	58,90 m/s
3-rd order McLaurin Polynomials	57,58 m/s
4-rd order McLaurin Polynomials	57,58 m/s

Table 28: Test semi-wing divergence velocity.

6.3.2 Syncro torsional divergence evaluation

After the considerations made on the simple constant cross-section beam, the analysis focuses on Syncro aircraft's semi-wing model that has been developed as described in chapter *3.9.3.3*. In this case, the divergence velocity is evaluated for an aerodynamic grid composed by:

- 20 chordwise panels.
- 40 spanwise panels (only the right semi-wing is considered).

These parameters have been chosen after a trial-and error process, that evidenced the following condition: as the number of panels is increased, the result converges to the values obtained for the selected grid (as shown in *Table 29*). A finer grid could be chosen, such as a *30x40* panels one, but this would imply excessive computational times and lead to the same result of the *10x40* and the *20x40* meshes.

Chordwise aerodynamic panels	***Spanwise aerodynamic panels***	***Divergence velocity***
10	20	191,21 m/s
	30	161,59 m/s
	40	158,05 m/s
20	20	192,68 m/s
	30	162,35 m/s
	40	158,75 m/s
30	40	158,98 m/s

Table 29: Syncro semi-wing divergence velocity evaluation, aerodynamic grid definition and convergence considerations for Δ=1.54 (real wing shear centre approximate position).

The relative position between shear centre and aerodynamic centre is defined through equation *6.6*:

$$\Delta = \frac{x_{shear\ centre}}{x_{aero\ centre}} \tag{6.6}$$

Where x coordinate defines the chordwise direction on the semi-wing reference system:

- If $\Delta > 1$ the shear centre is backwards respect to the aerodynamic centre.
- If $\Delta < 1$ the shear centre is located forward respect to the aerodynamic centre.

Shear centre relative position (Δ)	*Divergence velocity*
1	***Infinite***
1.1	317,15 m/s
1.2	246,57 m/s
1.3	207,10 m/s
1.4	181,62 m/s
1.5	163,59 m/s
1.5426	***158,98 m/s***
1.6	149,99 m/s
1.7	139,25 m/s
1.8	130,49 m/s
1.9	123,14 m/s
2	116,84 m/s
2.5	94,22 m/s
3	77,72 m/s
3.5	62.18 m/s

Table 30: Syncro semi-wing divergence velocity evaluation, 1.225 kg/m³ air density.

The experimental results show that the real shear centre of the aircraft is located approximatively at $\Delta=1.5426$ from the leading edge, thus the resulting divergence velocity can be represented by the value in equation *6.7*.

$$V_D = 158{,}98\frac{m}{s} \tag{6.7}$$

The effect of shear centre relative position is evidenced in *Table 30*, where the divergence speed decreases as the value of Δ grows, for $\Delta > 1$. At the same time, if $\Delta < 1$ the rotation induced by aerodynamic forces on the semi-wing induces an opposite rotation, that implies an imaginary solution (there is no divergence velocity). The general behaviour that can be identified is described by the following three situations:

1. $\Delta > 1$ the rotation induced by aerodynamic loads is positive (y axis, right hand rule).
2. $\Delta < 1$ the rotation induced by aerodynamic loads is negative (y axis, right hand rule).
3. $\Delta = 1$ the rotation induced is equal to zero,

For a fixed shear centre position, the effect of air density variation is analysed in *Table 31*, where divergence speed is evaluated for different altitudes, from *0m* to *4000m*. It can be obtained in two ways, that permit to furtherly prove the consistence of the here developed code:

- The most suitable way is to evaluate it from the divergence dynamic pressure obtained at *0m* of altitude and substitute the density for the considered flight level (*1000m*), as presented in *6.8*.

- The second way is to execute the static divergence code for the desired density (that is a computationally expensive way to evaluate the divergence condition); this permits to establish the validity of the code.

$$q_D = \lambda = \frac{1}{2}\rho_{0m}V_{D_{0m}}^2 = \frac{1}{2}\rho_{1000m}V_{D_{1000m}}^2 \tag{6.8}$$

Air Density	*Altitude*	*Divergence Velocity*
1.2250 kg/m^3	0 m	158,98 m/s
1.1000 kg/m^3	1107 m	166,07 m/s
1.0000 kg/m^3	2064 m	174,17 m/s
0.9000 kg/m^3	3097 m	183,59 m/s
0.8190 kg/m^3	4000 m	192,46 m/s

Table 31: Syncro semi-wing divergence velocity evaluation, altitude variation effect.

The results obtained show that the divergence condition is located outside of the envelope diagram of *Syncro* Light Sport Aircraft. In particular, the limit operational velocities of the aircraft are presented in *6.9*, where the never exceed velocity and the design one are presented:

$$V_D = 84{,}00 \text{ m/s}$$
$$V_{NE} = 75{,}56 \text{ m/s} \tag{6.9}$$

In the end, the dynamic divergence pressures are obtained for all loading factors that are concerned by the flight envelope. The divergence condition at maximum load factor (n) is located outside the envelope for the sea level condition (which is the most severe), as presented in *6.10*:

$$V_D = 79{,}50\frac{m}{s} > V_{NE} = 75{,}56\frac{m}{s} \tag{6.10}$$

6.3.3 Effect of lamination on divergence speed

The previous sections (*6.3.1* and *6.3.2*) do not consider the effect of advanced composite material properties on structural deformation and their effect on aeroelastic phenomena.

These considerations will focus on the influence of lamination direction on static divergence velocity, through the analysis of a rectangular cross section beam. The structure analyzed is realized with a generic orthotropic material (as specified in *Table 32*) and fibers orientation is defined as specified in the reference system presented in *Figure 48*.

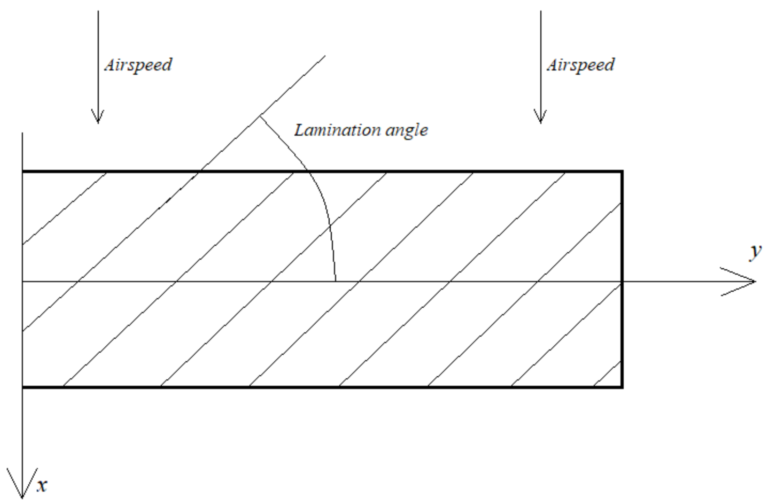

Figure 48: Orthotropic material lamination angle reference system for a generic beam structure.

In the case presented in *Figure 48* the lamination angle is positive (wash out lamination); the angles considered in the present analysis will be varied from -90° to +90°: in this way, the complete range of possible lamination angles will be investigated. The static structural deformation code is run at different lamination conditions, while all the other parameters of the semi wing are intentionally left constant. The static momentum load applied on the beam shows different torsion angles as the lamination is varied:

- Positive lamination angles imply a greater deflection for the trailing edge of the beam than for the leading edge if compared with the 0° lamination case
- Negative lamination angles determine an opposite condition at leading and trailing edge.

From these considerations, it is already clear that lamination will influence divergence speed (as well as on flutter velocity): this phenomenon is called aeroelastic tailoring. Its definition was proposed by *Shirk M. [21]*:

"the embodiment of directional stiffness into an aircraft structural design to control aeroelastic deformation, static or dynamic, in such a fashion as to affect the aerodynamic and structural performance of that aircraft in a beneficial way,"

Material properties (orthotropic material)			
Elastic Modulus Longitudinal direction	E_L = 30,5 GPa	*Elastic Modulus Transversal direction*	E_T = 10 GPa
Poisson's Ratio	v = 0,33	*Shear Modulus*	G = 5 GPa
Geometrical properties (constant along span)			
Section chord	c = 0,5 m	*Wingspan*	L = 5,00 m
Section height	h = 0,02 m	*Sweep angle*	$\Lambda = 0°$
Structural Mesh			
Beam elements	20	*Element nodes*	4
Cross section McLaurin polynomials order	3-rd	*DOFs (clamped boundary condition)*	1800
Aerodynamic Mesh (equally spaced grid)			
Chordwise panel's number		10	
Spanwise panel's number		40	
Panel's total number		400	
Torsional Divergence: test case analysis			
Shear centre position		$x_0 = c/2 = 0,250$ m	
Aerodynamic Centre Location		$x_{ac} = c/4 = 0,125$ m **	
Air density		$\rho = 1,225\ kg/m^3$	

Table 32: Orthotropic material beam structure properties.

As presented by *Librescu L., Thin-Walled Composite Beams [23] p. 508-512*, aeroelastic phenomena are typically influenced by the lamination angle of a generic orthotropic material wing structure. In particular, the deformation generated by aerodynamic loads on the considered structure can be enhanced by the lamination direction, that leads to different tip deformations in the classical structural analysis (where the influence of aerodynamic stiffness matrix term has not been introduced).

This condition is presented in *Figure 49*, where tip deflection angles for the complete range of possible laminations are reported for the following aerodynamic conditions (red line):

- $V_\infty = 50\,\frac{m}{s}$
- $\rho_\infty = 1{,}225\,\frac{kg}{m^3}$
- $\alpha = 2°$

The same analysis can be carried out for different airspeeds and incidence angles, generating an analogue trend but with lower or higher rotation angles. An example of this behaviour is proposed in *Figure 49*, where tip deflection angles for $V_\infty = 50\,\frac{m}{s}$ are compared with the ones for $V_\infty = 40\,\frac{m}{s}$ (blue line) and $V_\infty = 30\,\frac{m}{s}$ (black line). Positive and negative rotations are defined as:

1. Positive rotation when tip leading and trailing edge generate an angle concordant with *y* direction (considering the right hand rule).
2. Negative rotation in the opposite condition (discordant with *y* direction, right hand rule).

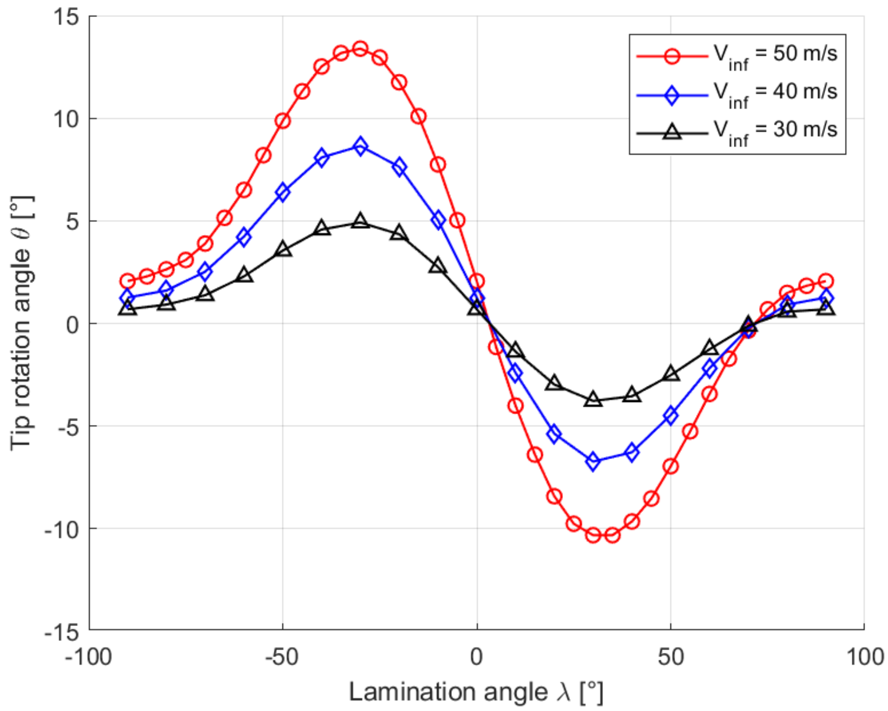

Figure 49: Tip section rotation angles for different lamination angles and airspeeds.

After this brief introduction on aeroelastic tailoring phenomena, the results of static divergence analysis executed on the example test beam are presented in *Figure 50*, where the *x* axis represents the lamination angle that has been considered, while on *y* axis the matching static divergence speed is reported. The results obtained show that a minimum value for static divergence speed is achieved for lamination angles around -30°, where V_D*=21,79 m/s*. This is in accordance with the maximum positive wing tip rotation observed in the static structural deformation result presented in *Figure 49*.

The general behaviour implies a reduction of divergence velocity for *wash in* conditions, while *wash out* leads to a rapid growth of divergence velocity. Lamination angles between 5° and 85° return an imaginary value from the static aeroelasticity code execution; this means that the divergence condition is not reached. In *Figure 50*, this range of angles is included between the two vertical dotted blue lines. In the end, divergence velocity obtained for 0° lamination can be considered as the reference value, that permits to make some quantitative evaluations (*Table 33*) on the percentual variation.

Lamination angle	***Divergence velocity***	***Percentual variation** (0° is the reference value)*
90°	54,96 m/s	-2,74%
85° - 5°	Non defined	Non defined
0°	**56,51**	0,00%
-5°	35,93	-36,41%
-10°	28,90	-48,85%
-15°	25,32	-55,19%
-20°	23,31	-58,75%
-25°	22,22	-60,68%
-30°	21,79	-61,44%
-35°	21,89	-61,26%
-40°	22,50	-60,18%
-45°	23,62	-58,20%
-50°	25,32	-55,19%
-55°	27,70	-50,98%
-60°	30,87	-45,37%
-65°	34,89	-38,26%
-70°	39,65	-29,84%
-75°	44,69	-20,92%
-80°	49,18	-12,97%
-85°	52,47	-7,15%
-90°	54,96	-2,74%

Table 33: Aeroelastic tayloring effect on divergence velocities, percentual variation.

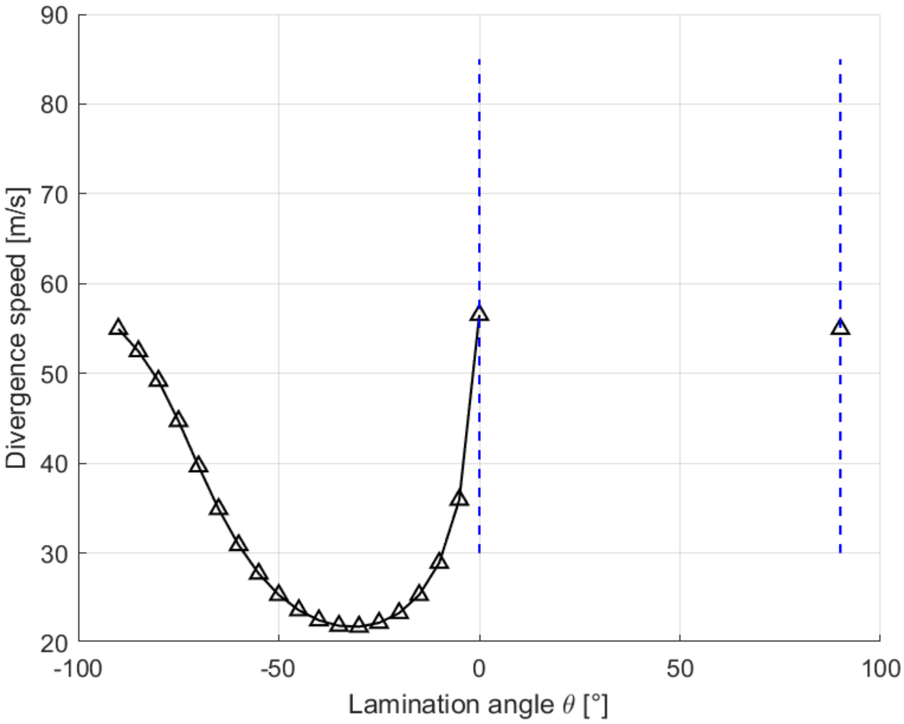

Figure 50: Aeroelastic tayloring effect on divergence velocities.

6.3.4 Sweep effect on static divergence velocity

In the present section, the effect of sweep angle of the semi-wing on static aeroelasticity will be investigated. It is defined as the angle between the y axis on the reference system presented in *Figure 51* and the quarter chord line, which is the line linking each 25% wing section point.

The variation from a negative angle to a positive one will be analysed, but some practical considerations must be performed regarding a typical real wing case.

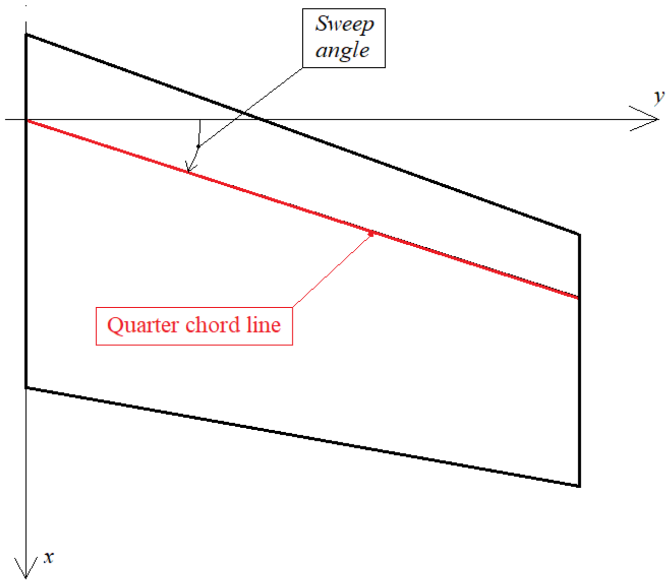

Figure 51: Sweep angle reference system on a generic tapered right semi-wing.

These observations are related to the following properties:

- Subsonic aircrafts flying at low velocities (incompressible range of speeds) usually present null or low sweep angles, since the primary effect of this parameter is to delay the surging of compressibility phenomena when high Mach numbers (M=*0.7-0.8*) are approached.

- High sweep angles both in the positive and negative range will be investigated, even thought that more limited angles will be considered in the project of a Light Sport Aircraft.

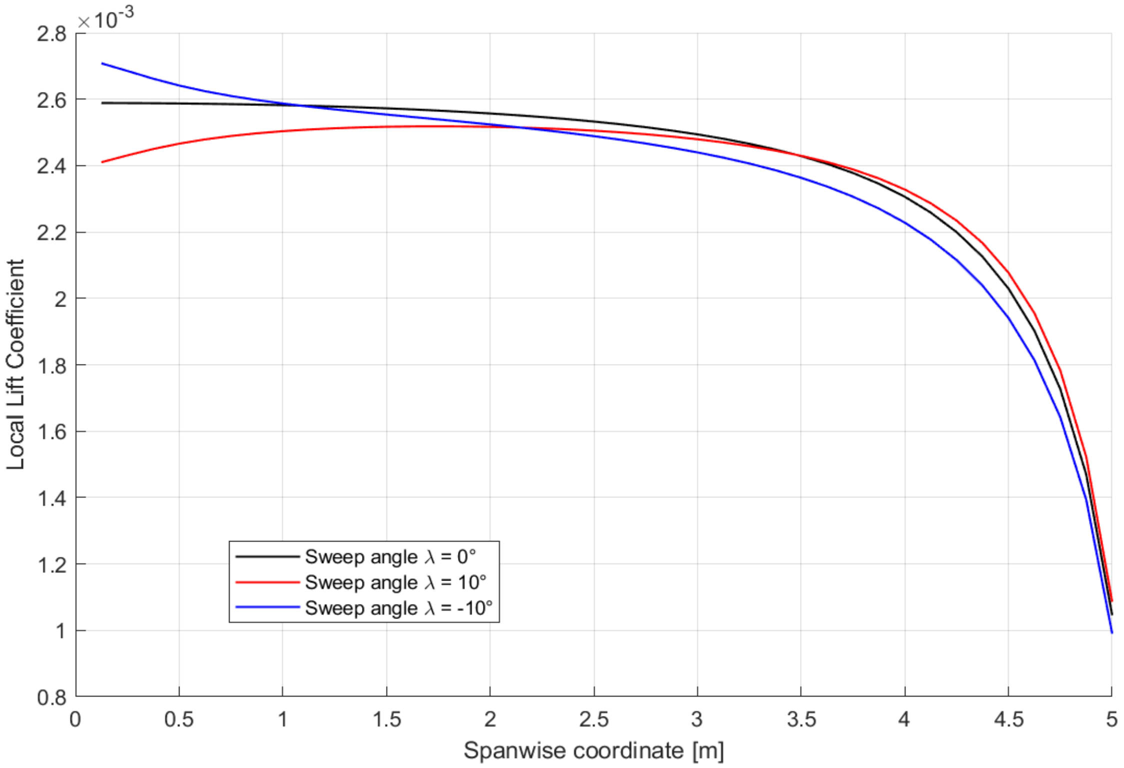

Figure 52: Sweep angle influence on spanwise lift coefficient distribution (present code results).

The test case that has been considered in this work is a rectangular cross-section beam structure realised with an isotropic material. In this way, only the effect of sweep will be evidenced: from the aerodynamic point of view, *Figure 52* represents the lift coefficient distribution for three different sweep angles (a positive angle, a negative one and the zero-sweep reference case).

Material properties (orthotropic material)			
Elastic Modulus		E_L = 75 GPa	
Shear Modulus		G = 28 GPa	
Poisson's Ratio		*ν* = 0,25	
Geometrical properties (constant along span)			
Section chord		c = 0,50 m	
Section height		h = 0,02 m	
Wingspan		L = 5,00 m	
Structural grid			
Beam elements	20	*Element nodes*	4
Cross section McLaurin polynomials		4-th order	
Aerodynamic grid			
Chordwise panels		10	
Spanwise panels		40 on semi-wing (80 total)	

Table 34: Test case beam properties and considered discretization.

Table 34 resumes the main aerodynamic and structural properties considered for the present case study, while *Table 35* reports the verification test cases compared to *AVL [11]* results. Lift coefficients are referred to a 1° incidence angle and underline a general good coherence between the two codes considered.

Sweep angle	***Lift coefficient (C_L)***		
	Present code results	*AVL [11] results*	*Relative error*
-10°	0,0942	0,0936	0,64%
0°	0,0955	0,0948	0,73%
10°	0,0943	0,0936	0,74%

Table 35: Lift coefficient results verification for three different sweep angles on the considered semi-wing (incidence: 1°).

At this point, the static structural code and the aerodynamic one (VLM) have been executed with several sweep angle conditions, that brought to the following observations:

1. Positive sweep angle generates a rapid increase of divergence velocity, in particular, static aeroelasticity code returns an imaginary value for angles above 10° (this means that the considered system does not present torsional divergence problems).

2. Negative sweep angles determine a quick reduction of divergence speed.

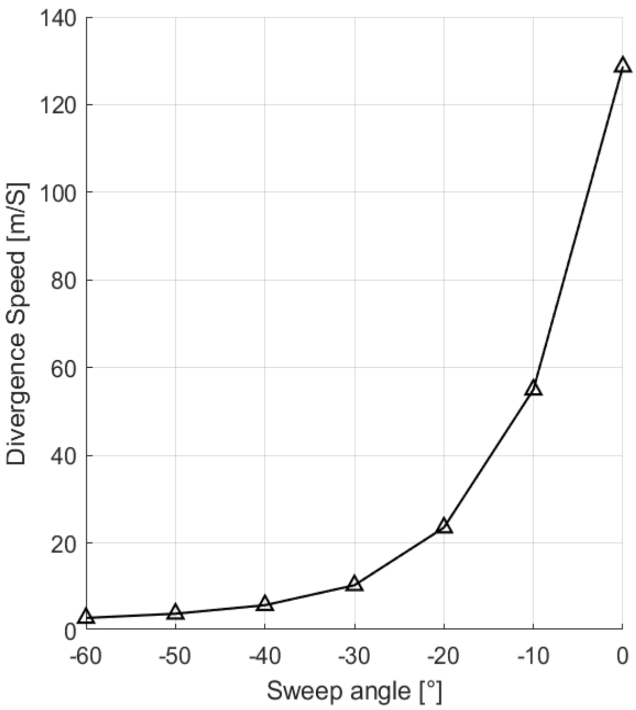

Figure 53: Sweep angle influence on static divergence velocity (present code results).

6.4 Flutter results

The various attempts made during the code development phase brought to a compromise: the solution proposed is based on k-method, that guarantees short solution times and the coherence with results obtained from the other instruments used in the following section. A verification of the results has been provided.

6.4.1 Constant cross-section test beam

The verification case that has been considered is a constant rectangular cross-section beam, that has the properties described in *Table 36* and *Table 37*. Flutter velocity has been compared to the ones obtained from the following theories:

- A two degrees of freedom p-k method based on Theodorsen's unsteady aerodynamics model; this code has been developed by *Petrolo M. and Zappino E. [17]* during Aeroelasticity lessons at Politecnico di Torino.
- *MUL2 Aeroelasticità 2020-2021 [18]* solver, which is a solver based on multiple degrees of freedom structural model, Double Lattice Method, and g-method.

Material properties (isotropic material)			
Elastic Modulus	E = 75 GPa	*Poisson's Ratio*	$\nu = 0{,}33$
Shear Modulus	G = 28 GPa	*Density*	$\rho = 2700$ kg/m^3
Geometrical properties (constant along span)			
Section chord	c = 0,2 m	*Wingspan*	L = 1,5 m
Section height	h = 0,01 m	*Sweep angle*	$\Lambda = 0°$

Table 36: Test beam geometrical and material properties for flutter analysis.

Structural Mesh			
Beam elements	20	*Element nodes*	4
Cross section McLaurin polynomials order	4-th	*DOFs (clamped boundary condition)*	1800
Aerodynamic Mesh (equally spaced grid)			
Chordwise panel's number	Case 1: 7 Case 2: 10	*Spanwise panel's number*	20
Panel's total number	Case 1: 140 Case 2: 200	*Reduced frequency limit*	$k < 0{,}08\pi \cdot (10) = 2{,}51$

Table 37: Test beam structural and aerodynamic grid properties for flutter analysis.

Damping and oscillation frequencies have been analysed from the k-method solution data. The crossing from a negative damping condition to a positive one has been searched in the range of considered velocities.

The results obtained from the various models show a general coherence between the analyses executed; in particular, the solution provided by the here developed k-method and the g-method from *MUL2 [18]* underline consistent results as the number of aerodynamic panels grows. The values imposed for reduced frequency are limited in the range of equation *6.11*:

$$k < 2.0 \tag{6.11}$$

Where the maximum reduced frequency is limited by the grid parameters chosen for the semi-wing. The results obtained for frequency values are reported in *Figure 54*, while the damping behaviour is not shown since the graphical result is of difficult interpretation for the considered range of speeds. Nevertheless, the velocity values for which the crossing from negative damping to positive damping is reported in *Table 38*, where the flutter condition is identified. The unstable mode is the fourth one, which is the first torsional mode for the considered beam structure.

<table>
<tr><th>Solver</th><th colspan="6">Flutter speed</th></tr>
<tr><td>2 DOFs p-k method</td><td colspan="6">224 m/s</td></tr>
<tr><td rowspan="2">g-method</td><td colspan="3">6x20 aerodynamic grid</td><td colspan="3">10x20 aerodynamic grid</td></tr>
<tr><td colspan="3">227 m/s</td><td colspan="3">226 m/s</td></tr>
<tr><td rowspan="2">k-method</td><td colspan="2">7x20 aerodynamic grid</td><td colspan="2">10x20 aerodynamic grid</td><td colspan="2">12x20 aerodynamic grid</td></tr>
<tr><td colspan="2">233 m/s</td><td colspan="2">230 m/s</td><td colspan="2">228 m/s</td></tr>
</table>

Table 38: Test beam flutter results comparison.

For the sake of simplicity, the results shown in *Figure 54* include only the frequency values obtained for velocities that are lower than 500 m/s: the considered range is still larger than the one of interest, but this permits to display the complete behaviour of the considered phenomena. The values obtained for transonic and supersonic speeds are meaningless from the physical point of view, since the hypotheses of VLM (based on Laplace's equation) are not valid for that range of velocities.

Moreover, *Figure 54* clearly shows the limitation that has been imposed to reduced frequency (*k*), that is identified by the virtual segment that connects the minimum velocity condition for each considered frequency. Finally, another consideration for the analysis that has been executed is related to the frequency values of the first unstable mode (*4-th*), that is merging with the third one.

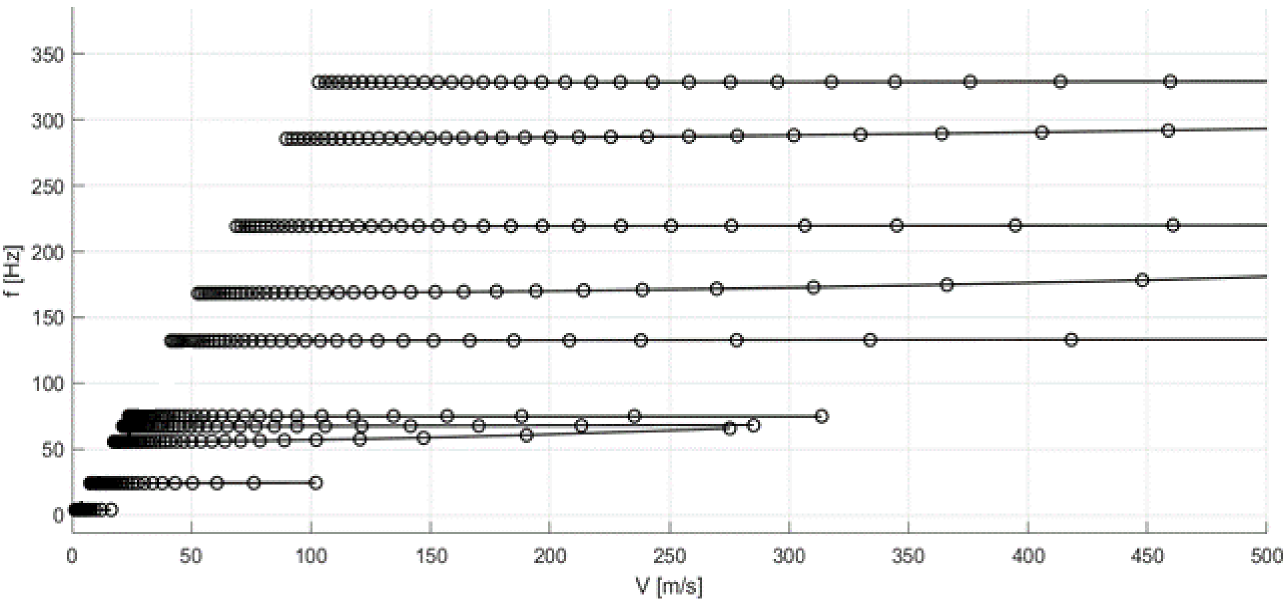

Figure 54: First 10 modes frequencies for the considered test beam.

6.4.2 Simple case experimental references and g-method analysis

Flutter analysis includes a large number of variables and error sources due to the many approximations that have been introduced in the steady and unsteady aerodynamic theories as well as in the structural model development. The present section has the aim to verify the obtained results with the ones presented by *Kemal Yaman, Subsonic Flutter of Cantilever Rectangular PC Plate Structure [22]*, where a comparison between experimental evidence and g-method results is carried out. A rectangular polycarbonate plate has been considered, with the properties resumed in *Table 39* and *Table 40*: the aerodynamic grid and structural discretization adopted in the codes developed in this work are listed in the same tables.

Present code aerodynamic grid	
Chordwise panels	*8*
Spanwise panels	*36*
Present code structural grid	
Elements	*20*
Cross section polynomial order	*4-th*
Element's nodes	*4*

Table 39: Reference rectangular beam aerodynamic and structural grids.

The experimental test has been carried out at ART (*Kemal Yaman [22]*), that is Ankara Wind Tunnel (maximum wind speed is 90 m/s), while the computational results were obtained from ZAERO© and MSC NASTRAN©. The polycarbonate beam is bound with a clamped boundary condition at the base of the wind tunnel; the same conditions are replicated in the software model.

Geometrical properties	
Beam length	$L = 1{,}0\ m$
Chord length	$c = 0{,}125\ m$
Cross section height	$h = 0{,}005\ m$
Polycarbonate material properties	
Density	$\rho = 1200\ kg/m^3$
Elastic Modulus	$E = 3{,}5\ GPa$
Shear Modulus	$G = 1{,}30\ GPa$
Poisson's Ratio	$\nu = 0{,}35$
Mass	$m = 0{,}75\ kg$

Table 40: Reference rectangular beam geometrical and material properties.

Finally, the results obtained from the present code, the g-method ones and the experimental test are presented in *Table 41*. Some considerations have been made on the evidence of this analysis:

- The present code results have a good coherence with the experimental ones considering the oscillation frequency of the polycarbonate beam (*Table 42* shows the first six modal frequencies obtained for the free-vibration case from the code described in *chapter 3.9.1*).
- The flutter velocity obtained from the present k-method is the smallest if compared with the *Subsonic Flutter of Cantilever Rectangular PC Plate Structure [22]* results, but it is also conservative.
- The detected fluttering mode is the same for all the considered cases.

Reference:	*Present code*	*Subsonic Flutter of Cantilever Rectangular PC Plate Structure [22]*		
Theory:	***k-method***	***Experimental Result***	***ZAERO© g-method***	***ZAERO© k-method***
Speed	21,45 m/s	24,89 m/s	22,5 m/s	23,8 m/s
Frequency	9,1 Hz	8,9 Hz	10,4 Hz	9,7 Hz
Mode	2-nd	2-nd	2-nd	2-nd

Table 41: Flutter results comparison for the rectangular beam test case considered.

Mode	*1-st*	*2-nd*	*3-rd*	*4-th*	*5-th*	*6-th*
Frequency	8,79 Hz	55,04 Hz	134,85 Hz	154,30 Hz	214,87 Hz	303,13 Hz

Table 42: First six free vibrational modes for the considered rectangular beam.

6.4.3 HALE aircraft equivalent wing model

Flutter analysis examples literature is rich of studies regarding small flat plates that have limited aspect ratios, that may generate problems in the present structural modal analysis instruments and later in the interaction with the aerodynamic code.

For this reason, an ideal example to test the present k-method is provided by HALE (High-Altitude, Long-Endurance) aircraft, that will be simplified in the present section due to the different flutter analysis input data approach that has been used. The information of this aircraft's wing are reported in *Table 43*, where its main properties are resumed; all data have been obtained from *Kirsch, B., Montagnier O., Bénard, E., Faure, T. [24]*, and *Mayuresh J. Patil [25]*:

Semi-span	L = 16,0 m
Chord	c = 1,00 m
Mass per unit length	μ = 0,75 kg/m
Centre of gravity (CG)	50%
Elastic axis (EA)	50%
Distance between CG and EA	0,00 m
Bending stiffness (y)	$EI_y = 2,00 \cdot 10^4$ Nm^2
Bending stiffness (x)	$EI_x = 4,00 \cdot 10^6$ Nm^2
Torsional stiffness	$GJ = 1,00 \cdot 10^4$ Nm^2

Table 43: Geometrical and structural properties of HALE aircraft.

An equivalent rectangular cross section for the present code semi-wing has been developed considering all data presented in *Table 43*: the thickness of the flat plate (h) has been computed from the mass per unit length parameter and the *x-y* planform geometry of the wing. The resulting value is $h = 0,05\ m$, that permits to also evaluate E_x, E_y, and G values, while the aerodynamic surface of this high aspect ratio wing is modelled through VLM and DLM codes from L and c values.

This is clearly a simplification since the real wing properties are different from the geometrical point of view and the free vibrational results will represent an approximation of the real case.

The properties of aerodynamic and structural grid are presented in *Table 44*:

Present code aerodynamic grid	
Chordwise panels	*10*
Spanwise panels	*60*
Present code structural grid	
Elements	*20*
Cross section polynomial order	*4-th*
Element's nodes	*4*

Table 44: HALE aircraft discretization properties.

Figure 55 reports the speed-damping plot obtained for the HALE aircraft model. As can be observed, only the fluttering mode is shown and the dynamic instability velocity is 31.92 m/s, while the frequency is 6.43 Hz (first mode). From the comparison with *Kirsch, B., Montagnier O., Bénard, E., Faure, T. [24]*, and *Mayuresh J. Patil [25]* results, flutter velocity is properly evaluated by the present code (the reference values from the previously quoted sources are included in the range *32.2-32.6 m/s*). On the other side, frequency presents a high error ratio, probably due to the simplifications introduced in the present wing geometry model.

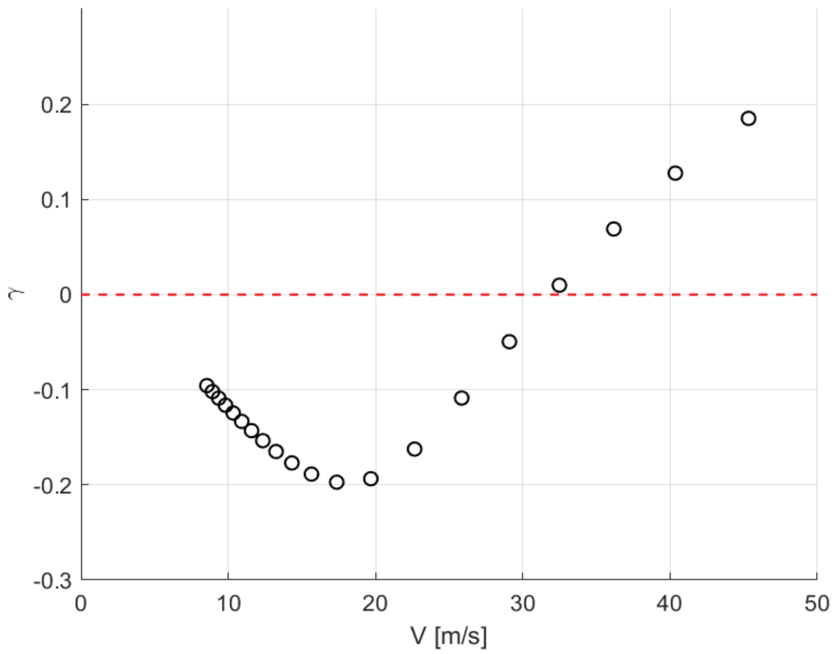

Figure 55: Unstable mode damping-velocity plot for HALE aircraft.

6.4.4 Syncro model flutter evaluation

Finally, this section considers k-method results on Syncro semi-wing model. The structure and aerodynamic properties have already been described in the previous chapters, in particular:

1. The structural model is made of 22 beam elements with variable spanwise properties; The structural analysis code verification has already been provided and the structural properties are the same that have been used for the static divergence investigations in *chapter 6.3.2*.

2. The aerodynamic model used for this analysis is a compromise between short computational times for the DLM code section execution and the respect of the other conditions that are imposed. In particular, the following number of panels has been chosen for the semi-wing model:

   2.1. Chordwise elements: 25
   2.2. Spanwise elements: 30

   This permits to set the reduced frequency limit to $k = 6.3$. Also, aspect ratio limitations are satisfied.

3. The splining process is then executed through the appropriate MatLab® code, that permits to evaluate displacements and slopes at each *Load* and *Control Point* for the considered modes. This is the last step that anticipates the k-method flutter code run.

The conditions presented in the previous section become even more complicate for the results concerning the model of Syncro aircraft's semi-wing, since the range of velocities obtained for the reduced frequencies that have been considered is extended to supersonic and hypersonic speeds.

As in the verification case, only the first 10 free-vibration modes have been considered and the results obtained are displayed in *Table 45*, where the fluttering mode and the correspondent velocity are reported.

Another central point is related to the number of panels that are necessary to properly describe the properties of the semi-wing: as the grid is refined, the solution time increases exponentially, determining the need to properly balance the number of panels. The grid that has been created satisfies the conditions imposed on the aspect ratio with a relatively short execution time.

Number of free-vibration modes	10
Fluttering mode	*2-nd*
Flutter velocity	132,6 m/s
Flutter Frequency	177,5 Hz

Table 45: Syncro aircraft flutter results.

This result is an approximation due to the many hypothesis that have been introduced, such as:

- The creation of the structural model of Syncro aircraft's semi-wing with the equivalent section model.
- The use of harmonic aerodynamic properties.
- The use of k-method to solve the dynamic aeroelasticity problem.

All these simplifications concur to generate possible inaccuracies on the real semi-wing representation, that has a much more complex structure than the ones used for verification cases or simple flutter analyses.

For this reason, the velocity that has been obtained is considered as an indicative result and will be compared with the ones provided by commercial structural codes in the future developments (as explained in the conclusive chapter).

Chapter 7

Conclusions

The final considerations about the present work are divided into three main sections, that reflect the procedure followed in the development phase. The main key points, as well as the advantages and drawbacks that have been identified, are underlined for:

- Aerodynamic analysis.
- Structural analysis.
- Aeroelastic analysis.

The codes for steady and unsteady aerodynamic analysis provide data that are coherent with the corresponding verification examples. The main hypotheses that were introduced are: inviscid flow and harmonically oscillating aerodynamic properties (for the unsteady case analysed through Doublet Lattice Method). This implies that the scripts proposed for VLM and DLM are a valid base for the analysis of trapezoidal wings aerodynamic properties in the linear range of angles of attack. The representation of stall phenomena is not provided by this theory.

Vortex Lattice Method can also account for limited profile camber effects by considering vortex ring elements: each panel is identified by the orthogonal vector with three components in three-dimensional space and the results obtained are coherent with the analogue analysis executed with *Athena Vortex Lattice [11]*. The same improvement can be done on Doublet Lattice Method by introducing the $D_{2,ij}$ term, which accounts also for z displacements of *Load* and *Control Points*. This term has already been presented in *chapter 2*, but it has not been implemented in the present analysis since it determines additional computational time.

The structural analysis instrument that has been developed in this work presents some advantages, but even some disadvantages that are determined by the approximations introduced in the model.

The main advantages are:

1. The rapidity in prototyping simple beam structures with constant cross-section or linear and limited taper ratio. The materials used can be both isotropic and orthotropic with a generic fibre orientation angle. The number of elements used to discretize the beam is arbitrary.

2. The structural code can be adapted to represent a general cross-section composed by an arbitrary number of rectangular/square elements. This permits to realize all the mainly used beam shapes for spars, such as I, T, and C ones.

3. The materials assigned to each section can be varied. This property is particularly useful, for example when a spar has a web realised in honeycomb or PVC, while caps are made of composite materials.

At the same time, some disadvantages have been identified from the various tests carried out:

1. Complex structures and realistic components, such as junctions and connection elements, are difficult to be modelled with this simple model.

2. Structures with huge geometrical properties variation from root to tip section tend to generate ill-conditioning in matrixial problems solution, that can be solved in modal analysis case with the use of Schur's decomposition of matrices (integrated in *eig()* function, as specified in *chapter 3.9.3.6*). A more effective approach could be to use Lagrange polynomials instead of McLaurin ones to discretize cross-section deformations for each element. This solution has already been adopted in other similar works and will certainly be a desirable future development for these codes.

The structural model used to represent Syncro's aircraft semi-wing is the result of several analysis and evaluations executed during the development process. The semi-wing has been modelled as a rectangular cross-section equivalent beam, whose deformation properties have been calibrated on the experimental bending and torsion results. In this model, the equivalent beam has the same mass properties defined for each real element, while geometry, material stiffness and density are derived consequently.

While it is an efficient and practical method to represent complex structures concerning many elements, the disadvantages of this solution are:

- A calibration phase is always necessary to set the correct cross-section properties, thus it is difficult to automatize the development of the model.

- The effect of aeroelastic tayloring cannot be investigated since the obtained beam is an equivalent structure where fibres orientation is not represented.

Finally, an alternative solution is to use the results of a commercial structural solver to analyse the semi-wing properties. The results obtained (mass and stiffness matrices) could be used as the input data for aeroelastic analyses.

Static divergence analysis results have been tested on a sample beam, that assesses the validity of the model. The results obtained are coherent with strip theory, but permit to study a variety of different semi-wings where the following properties can be varied arbitrarily:

1. Material (isotropic, orthotropic).

2. Aerodynamic surface geometry (taper ratio, discretization grid properties…).

3. Beam structure properties (taper ratio, different cross-sections…).

This permits to apply the obtained code to every static aeroelasticity problem when the structural results do not present singularities or ill-conditioning.

Flutter analysis results, on the other hand, are more complex to be interpreted than static divergence ones since many factors can influence this type of study. As described in *chapter 5*, dynamic aeroelasticity can be investigated through k-method, p-k method, and g-method (with an increasing precision from the first to the last method indicated). Flutter speeds presented in this work are obtained through k-method, because of the difficulties that have been encountered during the development phase: p-k method implies an iterative process to evaluate the value of p (which contains the information related to damping and oscillation frequency for the considered system of equations), which increases excessively computational time. This is due to the fact that every step of the iterative process implies the execution of the unsteady aerodynamics code in order to evaluate the contribute for that reduced frequency.

On the other hand, k-method avoids this iterative process and shortens the code execution time, while the precision of the obtained results is reduced and, in some situations, could generate inaccuracies due to the "looping" of frequencies and damping, as described by *Dale M. Pitt [16] p. 1*.

In the present codes, k-method represents a good compromise between accuracy and solution time, but p-k method remains a fundamental step for future developments from this work.

The main points of this last chapter underline that there are several perspectives to improve the present work from different points of view. Nevertheless, the result of this study is a complete assembly of MatLab® codes that permits to analyse, in a simplified way, the wing of a generic ultralight aircraft from the aerodynamic and structural point of view. Thus, this work could be a base support instrument for the analysis of future Synthesis s.r.l. products.

Chapter 8

Appendix

Appendix I – ISA Atmosphere

International Standard Atmosphere is the typical model for the variation of density, pressure, temperature and viscosity through a wide range of altitudes. For troposphere, which is the first layer of the atmosphere (about 0-10000m), temperature variation is defined through *A1.1*:

$$T = T_0 - 0.0065h \tag{A1.1}$$

$$\rho = \rho_0 \left(\frac{T_0 - 0.0065h}{T_0}\right)^{4.2561} = \rho_0 \left(1 - \frac{0.0065h}{T_0}\right)^{4.2561} \tag{A1.2}$$

Where h is the altitude considered from sea level in meters.

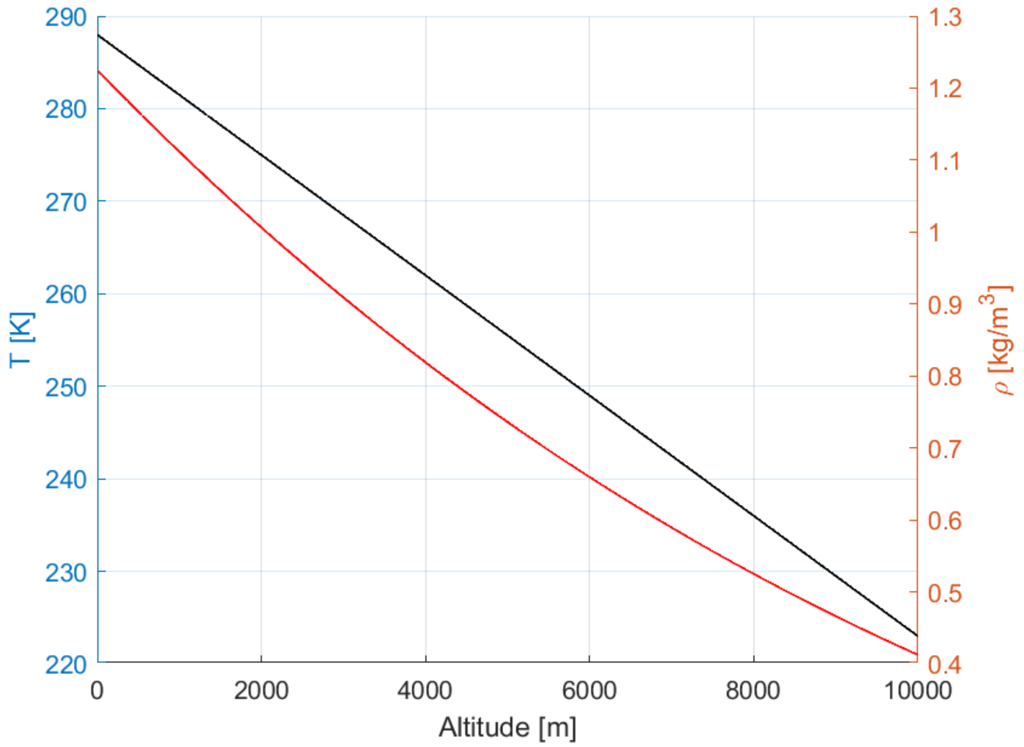

Figure 56: ISA Atmosphere temperature and density variation.

Appendix II – Material stiffness coefficients matrix

The transformation matrix described in equation *3.16* permits to obtain material stiffness coefficients matrix in the structural reference system, given the angle between the orthotropic material lamination direction and the reference system, and the values of the coefficients in the material reference *(1,2,3)*. The multiplications that must be carried out are the following, where the ~ apex is referred to the structural reference system values:

$$
\begin{gathered}
\tilde{C}_{33} = C_{33}\cos^4(\theta) + 2(C_{23} + 2C_{66})\sin^2(\theta)\cos^2(\theta) + C_{22}\sin^4(\theta) \\
\tilde{C}_{23} = C_{23}(\cos^4(\theta) + \sin^4(\theta)) + (C_{33} + C_{22} - 4C_{66})\sin^2(\theta)\cos^2(\theta) \\
\tilde{C}_{13} = C_{13}\cos^2(\theta) + C_{12}\sin^2(\theta) \\
\tilde{C}_{36} = (-C_{33} + C_{23} + 2C_{66})\,sin(\theta)\cos^3(\theta) + (C_{22} - C_{23} - 2C_{66})\sin^3(\theta)\cos(\theta) \\
\tilde{C}_{22} = C_{22}\cos^4(\theta) + 2(C_{23} + 2C_{66})\sin^2(\theta)\cos^2(\theta) + C_{33}\sin^4(\theta) \\
\tilde{C}_{12} = C_{12}\cos^2(\theta) + C_{13}\sin^2(\theta) \\
\tilde{C}_{26} = (-C_{33} + C_{23} + 2C_{66})\,cos(\theta)\sin^3(\theta) + (C_{22} - C_{23} - 2C_{66})\cos^3(\theta)\sin(\theta) \\
\tilde{C}_{11} = C_{11} \\
\tilde{C}_{16} = (C_{12} - C_{13})\,sin(\theta)\,cos(\theta) \\
\tilde{C}_{44} = C_{44}\cos^2(\theta) + C_{55}\sin^2(\theta) \\
\tilde{C}_{45} = (C_{44} - C_{55})\,sin(\theta)\,cos(\theta) \\
\tilde{C}_{55} = C_{55}\cos^2(\theta) + C_{44}\sin^2(\theta) \\
\tilde{C}_{66} = (C_{33} + C_{22} - 2C_{23} - 2C_{66})\sin^2(\theta)\cos^2(\theta) + C_{66}(\cos^4(\theta) + \sin^4(\theta))
\end{gathered}
\tag{A2.1}
$$

Appendix III – Static test loading conditions

The experimental loading tests carried out on Syncro aircraft semi-wing have been executed by charging the wing with a series of sandbags distributed along *y* coordinate. Their weight has been distributed on the elements of the beam model with a proper interpolation. The condition of 600kg wing loading is considered, thus each semi-wing is loaded with 300kg: this corresponds to a unitary contingence factor ($n=1$) MTOW of 600kg.

Loading process is intended to only create a bending in z direction, thus the center of mass of each sandbag is located on the torsional center of the wing section (this prevents the creation of torsional effects). At the same time, a twist test has been carried out: the incremental torsional moments measured for each element are reported in the following table.

y coordinate [mm]	***Element***	*Pure bending loading*		*Pure torsional loading*
		Loading [kg]	***Loading [N]***	***Momentum [Nm]***
0	1	17,225	168,978	329,590
200	2	16,921	165,999	317,270
400	3	16,618	163,020	305,380
600	4	16,314	160,042	293,920
800	5	16,011	157,063	282,870
1000	6	15,707	154,085	272,240
1200	7	15,403	151,106	262,000
1400	8	15,100	148,127	252,170
1600	9	14,796	145,149	242,710
1800	10	14,492	142,170	233,640
2000	11	14,189	139,191	224,940
2200	12	13,885	136,213	216,600
2400	13	13,582	133,234	208,620
2600	14	17,510	171,770	199,200
2800	15	12,974	127,277	173,540
3000	16	12,671	124,298	143,080
3200	17	12,367	121,320	114,050
3400	18	12,063	118,341	86,410
3600	19	11,760	115,362	60,110
3800	20	11,456	112,384	35,140
4000	21	8,952	87,822	11,450

Table 46: Semi-wing loadings for experimental tests.

Appendix IV - Code Interfaces

All the analysis carried out in this work have been presented in the previous chapters, as well as the results obtained from each of them. Before proceeding with the conclusions, a short review of the MatLab® codes and their user interfaces is presented, since they can be easily adapted to other aircrafts analyses.

IV.1 VLM interface

Even thought that aeroelastic analyses are based on uncambered profiles, a version of VLM code based on vortex rings and horseshoes is provided, thus cambered profiles can be introduced. The validity of the results obtained from this code has been proven through the *Athena Vortex Lattice (AVL) [11]*. As the program run button is selected, the interface that appears is the one presented in *Figure 57*. The parameters of a generic trapezoidal wing can be set to evaluate lifting properties of the surface that is considered:

- The first three parameters permit to use three different profiles along spanwise coordinate. The user must type the name of the file containing profile coordinates in two dimensions (a *.txt* file), while the code will automatically evaluate camber and panels discretization on the base of the following parameters.

- The following three boxes permit to set the conditions on which lift and induced drag are computed (the forces in Newton will be the output of the code); at the same time, the program will compute lift and drag coefficients for all the angles in the linear range, while stall is not modelled since this theory is based on inviscid aerodynamics.

- The other parameters permit to set geometrical properties of the wing and homogeneous grid discretization.

- The last two boxes are the ones that set the spanwise coordinate on which profile changes from the first to the second and from the second to the last one. The choice of a maximum of three different profiles along spanwise coordinate is based on the Syncro aircraft case, but it can be easily adapted to more complex situations.

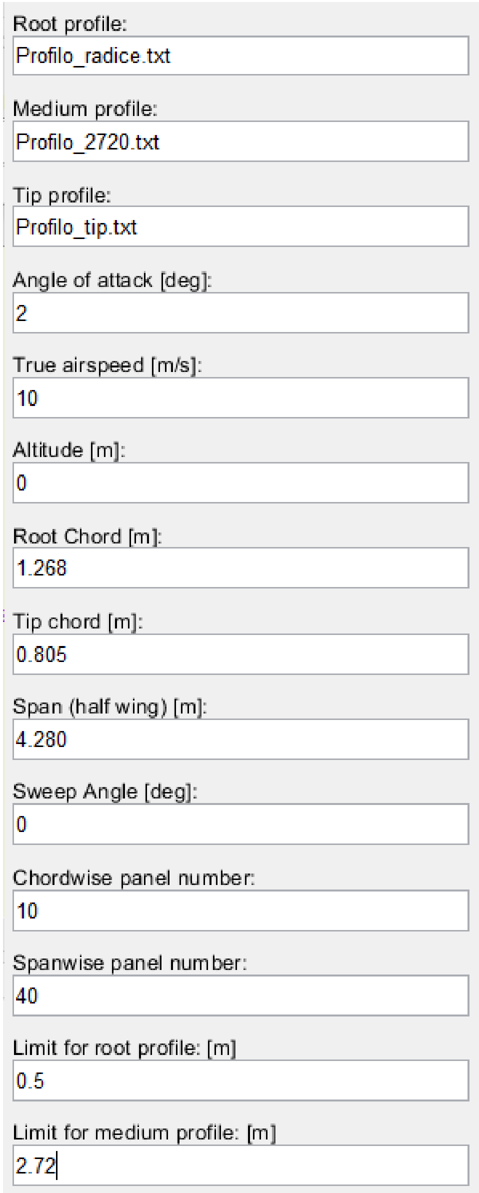

Figure 57: Vortex Lattice Method code user interface.

IV.2 DLM interface

A version of Doublet Lattice Method code with a user interface has been provided to evaluate the effect of oscillating aileron on lift of a generic trapezoidal wing. The input interface permits to set the same parameters described previously, and a series of parameters that are specific for this analysis:

- Aileron chord in meters.
- Aileron span, considering that its location extends from wing tip towards the root for the value that has been provided in the box.
- Aileron deflection in degrees.
- Reduced aileron oscillation frequency (k); if its value is equal to zero, the result obtained is the static lift coefficient for the considered aileron deflection.

The user must be aware that DLM code requires two conditions for the grid definition in the unsteady case, that have been defined in *chapter 2*. The first one relates the maximum reduced frequency to the panel chord, while the second relates the maximum aspect ratio of each panel:

$$\Delta x < \frac{0.08 V_\infty}{f} = \frac{0.08 V_\infty}{\omega} 2\pi = \frac{0.08}{k} 2\pi b \qquad (10.1)$$

$$AR < 5 \qquad (10.2)$$

The output provided will be the pressure coefficient for each panel of the semi-wing, that permits to evaluate the real and imaginary parts of the lift coefficient for the considered wing.

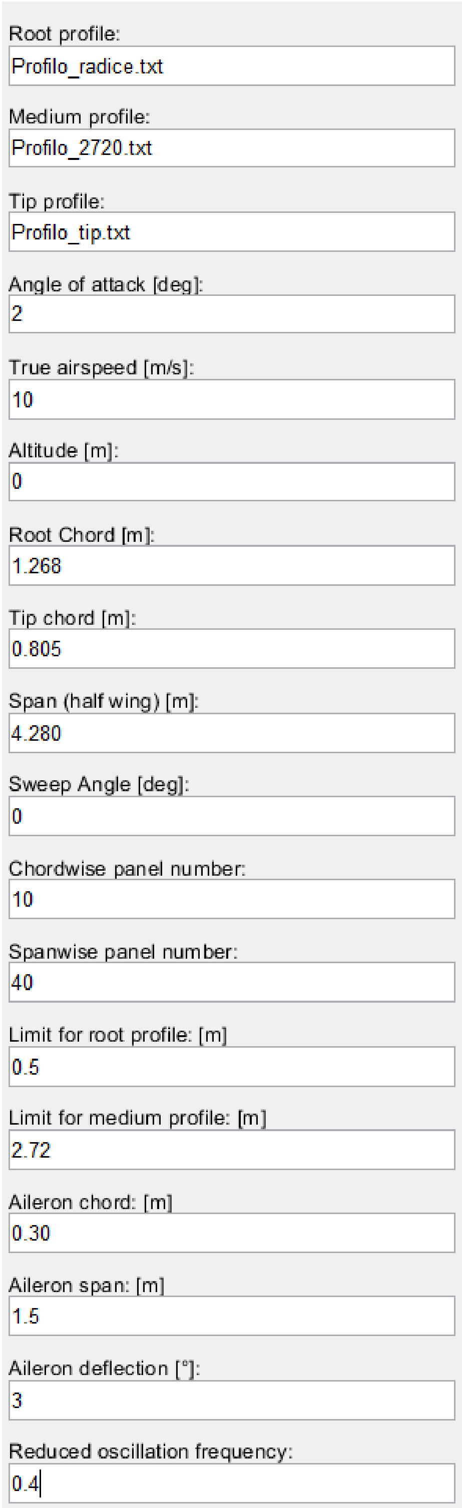

Figure 58: Doublet Lattice Method code user interface.

IV.3 Structural static deformation interface

As for the aerodynamic codes, an user interface has been provided for structural codes, that permits to rapidly prototype simple constant cross section wings, where the main geometrical properties and the material ones can be easily varied by the user. For more complex cases, such as the one of Syncro aircraft semi-wing, the most suitable solution is to assign the variable cross-section properties directly from the code lines. Nevertheless, *Figure 59* resumes the main properties that can be set by a generic user:

- The number of structural elements in which the beam is divided.
- The global beam length and its cross-section dimensions (x and z), that define its geometry.
- The number of free-vibrational frequencies considered if the modal analysis is carried out.
- McLaurin polynomial orders used to represent the beam properties (it can be varied in the range that goes from 2-nd to 4-th order).
- Sweep angle assigned to the structure.
- The material properties of the beam. The present code permits to discretise:

    1. Isotropic materials, where elastic moduli and shear moduli are equal in the three independent directions of the considered reference system.
    2. Orthotropic materials, where elastic modulus is different in the longitudinal and the transversal direction and depends on the lamination properties of the considered beam.

- The final three boxes permit to set the density of the material, Poisson's ratio, and fibres orientation for orthotropic materials. If the beam is made of isotropic materials, the fibres orientation must be set equal to zero degrees.

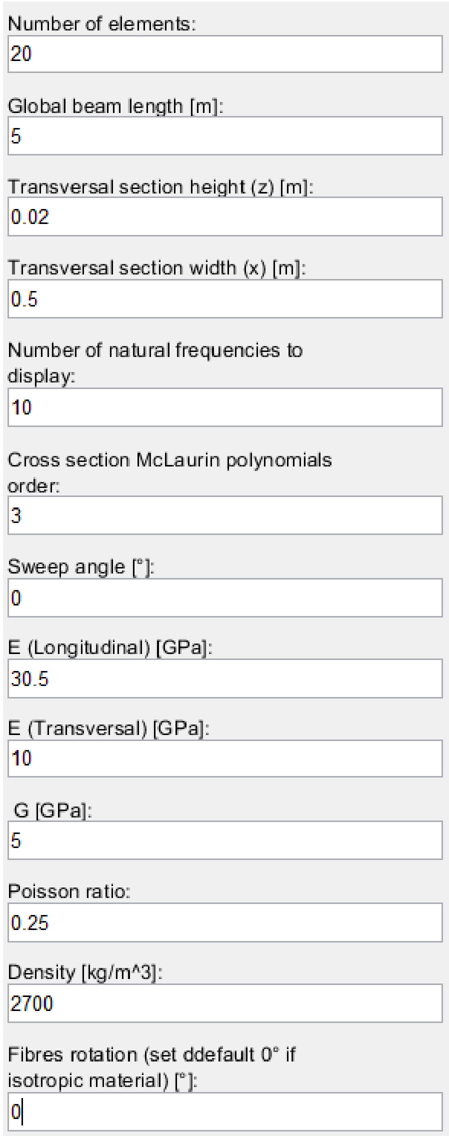

Figure 59: Structural code user interface.

IV.4 Other codes

A simple code interface has been provided even for the aeroelasticity codes, but it is often necessary to set some parameters and input conditions on the base of the specific situations that are considered. For this reason, a complete automatization of the evaluations is not suitable.

Bibliography

[1] Hodges, H., Pierce, A., 2011. Introduction to Structural Dynamics and Aeroelasticity, Cambridge University Press.

[2] A. R. Collar, The first fifty years of aeroelasticity, in Aerospace, 2, vol. 5, 1978, pp. 12–20.

[3] Kehoe, M., 1995. A Historical Overview of Flight Flutter Testing. NASA Technical Memorandum 4720.

[4] Wald, M. L., NY Times, 16-09-1997. https://www.nytimes.com/1997/09/16/us/old-problem-is-pinpointed-in-the-crash-of-fighter.html

[5] Reed, W., Garrick, I., November 1981. Historical Development of Aircraft Flutter, Journal of Aircraft, Vol. 18, N. 11, pp. 897-912.

[6] Corrado, C., 2009. Moti di fluido ideale irrotazionale: metodologie di soluzione.

[7] Arina, R., Fondamenti di Aerodinamica, Parte I – Nozioni introduttive e teoria del fluido inviscido. Levrotto e Bella.

[8] Katz, J., Plotkin, A., 1991. Low Speed Aerodynamics - From Wing Theory to Panel Methods. McGraw-Hill.

[9] Rodden, P., Taylor, P., McIntosh, S., 1996. Further refinement of the nonplanar aspects of the subsonic Doublet-Lattice lifting surface method. International Council of Aeronautical Sciences (ICAS), pp. 1786-1799.

[10] Blair, M., March 1992. A compilation of the mathematics leading to the Doublet Lattice Method. Wright-Patterson Air Force Base, Ohio.

[11] Drela, M. Athena Vortex Lattice (AVL). https://web.mit.edu/drela/Public/web/avl/

[12] Carrera, E., Cinefra, M., 2017. Fondamenti di Meccanica Strutturale, CLUT.

[13] Petrolo, M., 2011. Advanced aeroelastic models for the analysis of lifting surfaces made of composite materials.

[14] Varello, A., 2013. Advanced higher-order one-dimensional models for fluid-structure interaction analysis.

[15] Hassig, Hermann J., 1971. An Approximate True Damping Solution of the Flutter Equation by Determinant Iteration, Journal of Aircraft, Vol. 8, N. 11, pp. 885-889.

[16] Dale, M. Pitt, April 1999. A New Non-Iterative P-K Match Point Flutter Solution, AIAA 40th Structures, Structural Dynamics, and Materials Conference and Exhibit.

[17] Petrolo, M., Zappino, E., Aeroelasticity Lessons. Politecnico di Torino

[18] MUL2 Aeroelasticità 2020-2021. Static and Dynamic aeroelasticity solver. Politecnico di Torino. MUL2 Research Group.

[19] Forschling, H., Triebstein, H., Wagener J., April 1971. Pressure measurements on a harmonically oscillating swept wing with two control surfaces in incompressible flow. Symposium on Unsteady aerodynamics for aeroelastic analyses of interfering surfaces. AGARD.

[20] Rowe, W.S., Sebastian, J.D., Petrarca, J.R., March 1979, Reduction of Computer usage costs in predicting unsteady aerodynamic loadings caused by control surface motions – Analysis and results. Boeing Commercial Airplane Company Seattle, Washington.

[21] Shirk, M., Hertz, T., Weisshaar, T., 1986. Aeroelastic Tailoring – Theory, Practice, Promise, Journal of Aircraft, Vol. 23, No. 1, pp. 6-18.

[22] Kemal Yaman, 2016. Subsonic Flutter of Cantilever Rectangular PC Plate Structure. International Journal of Aerospace Engineering, Volume 2016. Hindawi Publishing Corporation.

[23] Librescu, L., Song, O., 2006. Thin-Walled Composite Beams. Springer, pp. 508-512.

[24] Kirsch, B., Montagnier O., Bénard, E., Faure, T. Computation of very flexible high-aspect-ratio composite wing flutter speed using optimised opensource solver. 53rd 3AF International Conference on Applied Aerodynamics Multiphysics approach in Aerodynamics, Mar 2018, Salon de Provence, France.

[25] Mayuresh J. Patil, May 1999. Nonlinear Aeroelastic Analysis, Flight Dynamics, and Control of a Complete Aircraft. Georgia Institute of Technology, pp. 38-41.